



TECHNISCHE
UNIVERSITÄT
WIEN
Vienna | Austria



VIENNA UNIVERSITY OF TECHNOLOGY

DIPLOMA THESIS

Structural and mechanical evaluation of collagen fibrils from equine tendon: The effect of age, tendon zone and type

Carried out for the purpose of obtaining the degree of Dipl.-Ing submitted at TU
Wien, Faculty of Mechanical and Industrial Engineering, by

Lukas Kain, BSc

Mat.Nr.: 0826268

Under the supervision of

Univ. Prof. Dipl. -Ing. Dr. sc. nat. Thurner P.J
Andriotis O. PhD

Institute of Lightweight Design and Structural Biomechanics

Declaration of Authorship

I, Kain L., BSc, declare that this thesis titled,

Structural and mechanical evaluation of collagen fibrils from equine tendon:
The effect of age, tendon zone and type and the work presented in it are my
own. I confirm that:

- This work was done wholly or mainly while in candidature for a research degree at this University.
- Where any part of this thesis has previously been submitted for a degree or any other qualification at this University or any other institution, this has been clearly stated.
- Where I have consulted the published work of others, this is always clearly attributed.
- Where I have quoted from the work of others, the source is always given. With the exception of such quotations, this thesis is entirely my own work.
- I have acknowledged all main sources of help.
- Where the thesis is based on work done by myself jointly with others, I have made clear exactly what was done by others and what I have contributed myself.

Signed:

Date:

Abstract

Faculty of Mechanical Engineering
Institute of Lightweight Design and Structural Biomechanics

Dipl.Ing

Structural and mechanical evaluation of collagen fibrils from equine tendon: The effect of age, tendon zone and type

by Kain L., BSc

Depending on their function, tendons are classified either as flexor or as extensor tendons. The superficial digital flexor tendon (SDFT) of the horse is an example of a flexor tendon. The SDFT is characterized by large extensibility, which enhances energy storage, important for locomotion due to decrease in energetic cost. In contrast, the common digital extensor tendon (CDET) of the horse, an extensor tendon (or position tendon), is less extensible than the SDFT. Mechanically, the SDFT has a lower elastic modulus and failure stress but higher failure strain along its long axis, compared to the CDET. In addition, structural as well as biochemical differences exist between the SDFT and the CDET. Although, the structure and mechanics at the tissue level of the SDFT and the CDET have been studied, little is known on the structural and mechanical properties of smaller hierarchical components of these tendons. These fascicular matrix and the interfascicular matrix and the components therein, most prominently the individual collagen fibrils. It is unknown how the mechanical properties of individual collagen fibrils are influenced by age and tendon type (i.e. SDFT and CDET). This thesis, provides an insight how mechanical parameters like the elastic modulus change with age in these two tendon types. Therefore longitudinal as well as transverse cuts of both tendon types (SDFT, CDET) from 3 and 18 year old horses were tested via microindentation on the AFM. Nanoindentation applied on individual collagen fibrils, the smallest structural component of a tendon, was subsequently carried out to find potential differences in their mechanical as well as swelling characteristics, according to age and type of the tendon.

Acknowledgements

First of all, I would like to thank my parents, who gave me the chance and always supported me in pursue the target of reaching this level of education and motivated me several times to finish it. Many Thanks to Prof. Philip Thurner, who gave me the chance to write the Thesis in his experimental biomechanics research group. Sincerest thanks goes to Dr. Orestis Andriotis who was always supporting me with his knowledge about atomic force microscopy and experience in performing experiments on biological tissue. Sincerest thanks are also given to the rest of the experimental biomechanics research group especially Dipl.-Ing. Martin Frank who spend much time on supporting me with the macroscopic compression tests but also to Mag.rer.nat. Vedran Nedelkovski who supported me with his knowledge in SEM imaging. Furthermore sincerest thanks goes to Mag. Marica Markovic who supported me with her knowledge about Agarose gels and helped me with the preparation of these hydrogels. Furthermore I want to thank Dipl.-Ing Peter Gruper and Katja Hölzl BSc MSc from the team of Assistant Prof. Dr. rer. nat Aleksandr Ovsianikov for the Polyethyleneglycol and gelmod sample provision.

Contents

Declaration of Authorship	i
Abstract	ii
Acknowledgements	iii
1 Introduction	1
1.1 Background and motivation	1
1.2 Thesis goal	3
1.3 Structure of the thesis	5
2 Equine tendons	7
2.1 Anatomical Basics	7
2.1.1 Collagen and collagen-fibrils	9
2.1.2 Collagen crosslinking	10
Interfibrillar crosslinking	10
Enzymatic crosslinking	12
Intrafibrillar crosslinking	12
2.2 Mechanical properties	14
2.2.1 Tendon	14
Superficial digital flexor tendon	15
Common digital extensor tendon	15
2.2.2 Age-related changes in the tendon	16
3 Atomic force microscopy	18
3.1 The atomic force microscope	18
3.1.1 Basic AFM-setup and measurement principle	19
3.1.2 Cantilever and tip	22
3.2 Imaging modes	24
3.2.1 Contact mode	25
3.2.2 Intermittent mode	27
3.2.3 QI-Mode	28
3.2.4 Non- contact mode	28

3.2.5	Feedback control loop	29
3.3	Force measurements	31
3.4	Indentation- type AFM	34
3.4.1	Nanoindentation	34
3.4.2	Microindentation	35
3.4.3	Analysis	35
	Oliver- Pharr method	36
	Determination of contact area A_c	38
	Determination of A_c using a TGT1 grating	40
	Sharp tips (Nanoindentation)	42
	Spherical tips (microindentation)	44
	Determination of A_c using trench gratings	46
4	Materials and Methods	51
4.1	Sample description	51
4.1.1	Tissue sections (micro-indentation)	52
4.1.2	Collagen fibrils (nano-indentation)	53
4.1.3	Hydrogels	53
	Polyethyleneglycol (PEG) and Gelatine	53
	Agarose	54
4.2	Atomic force microscopy	55
4.2.1	Microindentation	55
	Ideal cantilever spring constant for force measurements	55
	Tendon cryosections	57
4.2.2	Nanoindentation	62
4.2.3	Imaging of individual collagen fibrils	62
4.2.4	Microsphere glueing	64
4.3	Macroscale compression tests	66
4.3.1	SEM imaging of microspheres	68
4.3.2	Statistical analysis	69
5	Results and Discussion	70
5.1	Microsphere diameter evaluation	70
5.2	Validation experiments on Agarose	73
5.3	Microindentation on tendons	77
5.3.1	Micromechanical properties of LC and TC tendon sections	78
5.4	Nanoindentation on individual collagen fibrils	87
5.4.1	Swelling behaviour	90

5.5 Comparison to literature	93
6 Summary, conclusion and outlook	95
A Microindentation on gelmod and Polyethyleneglycol	98
A.1 Gelmod	98
A.2 Polyethyleneglycol (PEG)	103
Bibliography	105

List of Figures

2.1	Forelimb of the horse showing CDET and SDFT tendon	8
2.2	Hierarchical structure of a tendon from the nano to the macroscale	9
2.3	Fibril aggregation (D-banding)	10
2.4	Crimp in SDFT and CDET tendon structure	11
2.5	Inter- and intramolecular-crosslinking of collagen	13
2.6	Stress-strain curve of tendon	14
3.1	Basic AFM-setup	19
3.2	Sensitivity determination on hard surface	21
3.3	Different AFM cantilevers and tips	24
3.4	Imaging- mode regions	26
3.5	Tip vs. sample roughness & tip deconvolution	27
3.6	Block diagram showing feedback control loop	29
3.7	Feedback- loop control	30
3.8	Spring constant determination using Euler-Bernoulli theory	32
3.9	Micro-/ vs. Nanoindentation type AFM	35
3.10	Analysis procedure	36
3.11	Indentation- type AFM	37
3.12	Ac determination with TGT1 grating	41
3.13	TGT1-grating	41
3.14	Tip deconvolution sharp tip	45
3.15	Spherical tip diameter determination limitations using TGT1	47
3.16	Lineprofile of TGT1 image	48
3.17	Trench scanning procedure to determine sphere diameter	49
3.18	Procedure for analysing trench height data	50
4.1	Cryosection samples on glass slide with PMMA ring	52
4.2	Ideal choice of cantilever stiffness for indentation type AFM	56
4.3	Relationship of contact depth and interaction volume for 10 μm and 15 μm spheres	58
4.4	Typical positions having been tested in microindentation	59
4.5	Procedure of nanoindentation and imaging	64

4.6	Procedure of microsphere glueing	66
4.7	Macroscale compression test	67
5.1	Microsphere diameter estimation results	71
5.2	SEM image of an unused and contaminated cantilever	72
5.3	Ratio E_{AFM}/E_{Comp}	74
5.4	Ratio E_{AFM}/E_{Comp} vs. Indentation depth	74
5.5	Boxplot Agarose Validation results	76
5.6	Errorbar E_{AFM} vs. E_{Comp}	76
5.7	Stress-strain curves from compression tests on agarose	77
5.8	Results from microindentation experiments on longitudinal tissue sections	78
5.9	Results from microindenation experiments on transversal tissue sections	79
5.10	Illustration of the fibril orientation in the FM and the IFM	83
5.11	Illustration of the material behaviour when loading tissue in LC and TC	85
5.12	Fascicular and interfascicular matrix on longitudinal cut	86
5.13	Results from nanoindentation experiments on individual collagen fibrils	88
5.14	Boxplots showing swelling behaviour of individual collagen fibrils	91
5.15	Swelling ratio of individual collagen fibrils	91
5.16	Fibril diameter in PBS	92
5.17	Fibril E-modul vs. swelling ratio	92
A.1	Results from microindentation experiments on UV cured gelmod	100
A.2	Results from microindentation experiments on UV cured gelmod	101
A.3	Results from microindentation experiments on UV-exposed gelmod (Boxplots)	102
A.4	Results from microindentation experiments on UV-crafted Polyethylene glycol	104

List of Tables

4.1	Overview of samples having been tested	51
4.2	Parameters for microindentation experiments on tendon sections	60
4.3	Parameters for micro-indentation agarose experiments	61
4.4	Parameters for macroscale compression tests	68
5.1	Diameter results from AFM/ SEM sphere imaging	70
5.2	Results from Agarose validation experiments	73
5.3	Results from microindentation experiments on longitudinal tendon cut samples	79
5.4	Results from microindentation experiments on transversal cut tissue sections	80
5.5	ANOVA on microindentation data of longitudinal cuts	80
5.6	ANOVA on microindentation data of transversal cuts	81
5.7	Buckling consideration from micro and nanoindentation data . . .	84
5.8	Non-parametric test: Wilcoxon rank sum test	87
5.9	ANOVA from nanoindentation data	89
5.10	ANOVA from nanoindentation data	89
5.11	Swelling results of individual collagen fibrills from different samples	90
A.1	Results from gelmod experiments	103
A.2	Results from gelmod experiments	103

List of Abbreviations

AFM	Atomic Force Microscopy
SPM	Scanning Probe Microscope
CL	Cantilever
PID	Proportional Integral Derivative
FM	Fascicular Matrix
IFM	Interfascicular Matrix
LS	Least Square
CDET	Common Digital Extensor Tendon
SDFT	Superficial Digital Flexor Tendon
PEG	Polyethyleneglycol
MTJ	Myotendinous Junction
OTJ	Osteotendinous Junction
AFM	Atomic Force Microscope
FACIT	Fibril Associated Collagen with Interrupted Triple helices
MACIT	Membrane Associated Collagen with Interrupted Teiple helices
LOX	Lysyl Oxidase
DHLNL	Dihydroxylysino-leucine
HLNL	Hydroxylysino-leucine
PYD	Pyro-dinoline
DPD	Deoxy-pyridinoline
AGE	Advanced Glycation End Products
PG	Proteoglycan
GAG	Glycosaminoglycan
SPM	Scanning Probe Microscope
AFM	Atomic Force Microscope
SEM	Scanning Electron Microscope
STM	Scanning Tunneling Microscope
CL	Cantilever
QI	Quantitative Imaging
PT	Perpendicular Trench direction
LT	Longitudinal Trench direction

PMMA	Polymethylmethacrylate
PBS	Phosphatebuffered Saline
FMP	Force-Mapping
FS	Force-Spectroscopy
TC	Transverse Cut
UV	Ultraviolet
ANOVA	Analysis Of Variance
CoV	Coefficient of Variance
IV	Indentation Volume

Physical Constants

Boltzmann's constant $k_B = 2.997\,924\,58 \times 10^8 \text{ J K}^{-1}$ (exact)

List of Symbols

Z	Z-piezo displacement (m)
k	Cantilevers vertical spring constant (N/m)
D	Cantilevers deflection (m)
w_{max}	maximum vertical deflection of the tip (m)
l	Cantilever length (m)
λ	periodicity of surface topography (m)
v	maximum achievable scanning velocity (m/s)
D_v	Damping (Ns/m)
σ	Distance where Lennard-Jones potential becomes zero (m)
ϵ	depth of the local minimum of potential energy of Lennard-Jones potential
r	Distance between two particles (m)
f_r	Cantilevers resonance frequency (Hz)
K_p	Proportional gain
K_I	Integral gain
K_D	Differential gain
M	Section Moment (Nm)
E	Elastic modulus (N/m ²)
E_{AFM}	Elastic modulus from AFM experiments (N/m ²)
E_{COMP}	Elastic modulus from compression tests
b	Cantilevers width (m)
t	Cantilevers thickness (m)
β^*	Correction factor
D_I^*	Effective deflection (m)
Q_f	Quality factor
ρ_f	Density of the fluid (kg/m ³)
ω_f	Resonant frequency of the cantilever (Hz)
ω	Oscillation frequency (Hz)
Γ_i	Imaginary component of the hydrodynamic function
k_r	Stiffness of the reference cantilever (N/m)
s_s	Slope on hard sample
s_r	Slope on the reference

A_c	Projected contact area (m ²)
F	Force (N)
I	Indentation (m)
D	Deflection (m)
ν_i	Poisson's ratio of indenter
ν	Poisson's ratio of sample
E_i	Elastic modulus of indenter (N/m ²)
h_c	Contact depth (m)
D_M	Microsphere diameter (m)
α	Half of spikes opening angle (°) k_s
k_{nom}	Cantilevers nominal spring constant (N/m)
k_{trze}	Cantilevers true measured spring constant (N/m)
d_{nom}	Nominal sphere diameter (m)
p	Statistical p value
R_{TGT1}	Microsphere radius measured using TGT1 grating (m)
R_{LT}	Microsphere radius measured using trench in longitudinal trench direction (m)
R_{PT}	Microsphere radius measure using trench in perpendicular trench direction (m)
IV	Indentation Volume (m ³)
n	number of samples
P_{crit}	Critical force according to buckling (N)
D_{AIR}	Fibril diameter measured in air (m)
D_{PBS}	Fibril diameter measured in PBS (m)

Chapter 1

Introduction

1.1 Background and motivation

The main task of tendons is to transmit forces produced in the muscles to bones and therefore enabling locomotion. Some of these tendons expand their task from being more connecting elements to energy-storing springs. Thereby they recuperate mechanical energy of up to 40% [3] and thus improve the locomotion efficiency. Such specific tendons are the flexor tendons. In contrast, tendons, which are mainly in charge of positioning musculoskeletal structures, are known as positioning (extensor) tendons. The most popular flexor tendon in the equine anatomy is the superficial digital flexor tendon (SDFT) whereas the common digital extensor tendon (CDET) is an ideal example of a positioning tendon. During locomotion, energy storing tendons undergo much higher strains (16.6% SDFT during gallop [52]) than positioning tendons (CDET max *in vivo* of 3% [6]). As a result flexor tendons often get very close to their ultimate strain limit (*invitro* failure strain SDFT= 25.98% and CDET= 20.45% [6]), which makes injuries of these structures as one of the most common reason of lameness in thoroughbred racehorses [41]. A study in 2002 investigated injuries on event horses in one- and multiple day events over a period of one year. Thereby 14.5% of the total injuries were related to the SDFT [49]. It's of great common interest to decrease the amount of tendon fractures or injuries in horses. This might be done defining appropriate trainings based on results of investigations on these kind of tendons. Though the scientific relevance of these two equine tendon types is also given for humans. The SDFT and the human Achilles tendon are functionally and clinically equivalent and no equally appropriate analogues in rodent, rabbit or other animals exist [42]. The CDET on the other hand is an ideal analogous to the human anterior tibialis tendon [28]. Tendons are able to heal naturally. Though, the fact, that these structures are less blood circulated, leads to such injuries recover quite slowly. Further, scar tissue developed

in the impaired structure decreases their flexibility. Therefore these structures hardly reach their original properties and often tend to suffer from repeated injury [50]. Supporting initial tissue growth by special scaffolds could thereby be a better solution against traditional surgical repair techniques, which use sutures and soft tissue anchors. Adjusting these scaffolds to the natural unimpaired mechanical tendon properties, could prevent external loads from being initiated on the injured structures and thereby disturbing the healing process. So investigations giving further insight into how loads exactly being transmitted in tendon structures, might be highly relevant for tissue engineering [31]. In general tendons are hierarchically structured fibre-composite materials built up from the nano- to the macroscale. They are mainly built up by collagen molecules of type I, which aggregate to fibrils and further fuse to larger well orientated dense structures called fibres and fascicles and finally to the tendon itself. These regions, characterised by a high density of well aligned individual collagen, are known as the fascicular matrix (FM). The interfascicular matrix (IFM), a fine sheath of connective tissue, surrounds each of these fascicles and is thought to be important for the high extensibility of the flexor tendons [59]. Such fibre-composite materials in general, tend to have anisotropic material properties, based on mechanical characteristics of the single fibres and the embedding matrix. Whereas in tendons these fibres are the collagen fibrils, the matrix which surrounds and connects these fibrils is mainly built up by a specific protein family called proteoglycans [50]. This arrangement mainly leads to characteristic directions in the material, sustaining higher maximum loads than others. On the one hand tendons adjust their mechanical characteristic by adapting their matrix. This is done using different types of proteoglycans. Here smaller ones are used in tension regions whereas larger ones are more likely in the compression zones [50]. Another adjustable parameter is the morphology of the tissue, by locally distinct distributions of certain fibril diameters [63]. The collagen fibrils might also locally influence the tissues properties as they have the ability to more or less change their diameter (swelling behaviour) [19]. This behaviour or the state of hydration at all might also be a factor which could be correlated with specific mechanical properties on the tendon macroscale level. To completely characterise the anisotropic tendons materials, it is necessary to investigate their mechanical properties in different directions. Although tendons are loaded primarily in tension, still regions exist where they undergo external compression. These are mainly positions, where tendons change direction around bony structures, but also in tensile regions when being extended

[50]. There is already some data available according tendons on the macroscale in tension [6]. Also investigations based on tensile experiments of single fascicles and fibrils can be found but much less [56, 59, 63]. Though, data showing tendons microscale and nanoscale level in different directions (i.e. tendons transverse and longitudinal direction), from different zones (i.e. FM and IFM) combined with investigations on individual fibrils all from one sample is not known to be available so far. Still, such datasets could make it possible to more properly three dimensionally characterize the tendons. This knowledge could then also be used to build up FE-models for further analysing different parameters. The atomic force microscope was found as a good candidate to investigate on biological tissues. It was also already successfully used to test mechanical properties on the nanoscale and microscale of tendon tissue [1, 19, 53]. Another characteristic of tendons, which is worth being investigated is how tendon tissue, especially also their single components change their mechanical properties with age. So far tensile investigations on single fascicles showed a significant increase in failure stress and modulus of the SDFT and a decrease in modulus in fascicles from the CDET [59]. Investigations on the IFM showed that low stiffnesses of the SDFT, which was supposed to be in charge for the high extensibility of this tendon type is lost with increasing age [56]. This finding also suggested to be a reason why old tendons tend to fail more likely due to the risk of fascicles being loaded at an earlier point during tendon extension. So quite some different investigations were done from the macro- to the microscale level but there are still many unsolved questions which might be answered from data of the lowest hierarchical levels of the tendons (fascicles in transverse and longitudinal direction especially the FM and IFM and individual collagen fibrils).

1.2 Thesis goal

Tendons are hierarchical biological fibre reinforced materials built up from the nano to the macroscale. It's well known that mechanical properties of certain levels of such materials are highly influenced by distinct characteristics of the elements from the lower level. Tendons have quite intensely been investigated on the macroscale level, though data on the lower regions especially from the smallest structural elements, the fascicles and fibrils is quite scarce. Fibre reinforced materials like tendons, are highly anisotropic which means that they

respond differently according to the direction external loads are applied. Therefore it is necessary when characterising their mechanical properties to investigate them in different directions. Tendons are structurally aligned and mainly also loaded by tensile forces in their longitudinal direction. Therefore the main directions of interest are the longitudinal and transversal direction. Therefore goal of this thesis was to investigate fascicles, so bundles of single collagen fibrils on the microscale level. It was the aim to get a whole set of information about the mechanical properties in longitudinal direction as well as in transversal direction. Fascicles can further be divided in two specific regions according their density and orientation of individual collagen fibrils. The fascicular matrix (FM) is characterised by having a highly structured morphology, consisting of fibrils densely be packed and aligned in tendons longitudinal direction. The interfascicular matrix (IFM) on the other hand is located in between the FM regions. The morphology of these locations is characterised by a some kind of amorphous structure were single fibrils follow no specific direction. As such differences in morphology commonly also appear to be different in their mechanical properties makes it possible to additionally also investigate these structures independently. Further, individual fibrils, the smallest units the fascicles are build up with, should be tested. Information about these units should make it possible to gain knowledge from connections binding individual fibrils in the FM. to achieve these goals cryosections from longitudinal and transversal cuts of the superficial flexor tendon (SDFT) and common digital extensor tendon (CDET) were investigated from a 3 and 18 year old horse. A couple of individual fibrils were further harvested from the same samples. The main focus was given on spent on the elastic properties mainly characterised by the elastic modulus. Beside the mechanical properties also the morphological characteristics of the the different samples and zones (FM and IFM) should be investigated and if possible related to the the mechanical properties.

The atomic force microscopy (AFM) is known to be an ideal technique to investigate both, mechanical and structural properties of soft biological tissues. Therefore it seemed to be ideal for coping with the various exploration goals. The investigations on mechanical properties were done using indentation type AFM. Here, microindentation characterised by a microspherical indenter was chosen for investigating the cryosections. To identify properties of the much smaller individual collagen fibrils nanoindentation with conventional cantilevers furnished with sharp tips were applied.

Nanoindentation on collagen fibrils has already been validated before [1].

Therefore also the same procedure was chosen for the investigations on these fibrils. Microindentation on the other was is not standardised to far and therefore had to be validated. Here, Agarose hydrogels gels with different concentrations (i.e. different stiffnesses) were tested in conventional compression tests and in the AFM.

For indentation type AFM the cantilever tips geometry (i.e. their diameter) has to be analysed. Therefore a protocol was developed using commercial available test grating (TGT1 and trenches). Several microspherical tips were investigated according this protocol. The diameter results were compared with measurements from investigations on the same microspheres using a scanning electron microscope.

Additionally to the Tendon experiments furthermore UV-cured Gelmod and Polyethyleneglycol samples were tested in microindentation experiments to show the ability of the AFM to detect small differences in mechanical properties in kPa and MPa region.

1.3 Structure of the thesis

In chapter 2 a general background of equine tendons is given and anatomical basics are described. Differences between the two tendon types having been investigated, the superficial digital flexor tendon and the common digital extensor tendon are going to be discussed in more detail and specific findings from previous investigations are presented. Further the characteristic of individual collagen fibrils, the smallest structural units of tendons are going to be presented as also how they aggregate from single collagen molecules to larger structures. Thereby enzymatic and non-enzymatic crosslinks are going to be described. In a further step the mechanical properties of the SDFT and CDET are shown. Furthermore age related changes of these structures are presented.

Chapter 3 gives an insight in atomic force microscopy (AFM), which was the main technique used in the experiments of this thesis. After giving a brief overview about the history and the ability of AFM, the basic measurement principle is described with nowadays mainly used detection methods. Further the AFM cantilever with its tip on the very end side, is described and different shapes and their fields of applications are discussed. Furthermore the main different imaging modes are explained in more detail. Briefly also the feedback control loop, which is mainly in charge for controlling the predefined user

settings is described briefly. As force measurements have been the core experiments in this thesis, the theoretical basics are shown in more detail in this chapter. Here general basics are given expanding an explanation of the AFM type micro- and nanoindentation. Then the Oliver-Pharr method the data was further on analysed with is presented. Another part which is shown in more detail in this chapter is the way how AFM TGT1- and trench test grating can be used, to analyse AFM probes and what the limitations of these procedures are.

Chapter 4 includes the materials and methods, which describe in more detail how the experiments on the tendon and agarose samples were performed. Furthermore the most important point of the sample preparation is presented. The exact procedures having been used in the nano- and microindentation experiments are described as also the imaging of individual collagen fibrils, which was necessary to investigate the swelling behaviour. Also the procedure of how tipless cantilevers are furnished with microspheres for the microindentation experiments is shown in this chapter. Then also the principle of how the macroscale compression tests were performed on agarose gels is given. Finally this sections contains information about the SEM imaging used for investigation on the geometry of the spherical tips. Finally the way of how the statistical data was analysed is described

In chapter 5 the findings of the particular experiments are summarized and discussed.

In chapter ?? the overall summary, conclusion of this thesis as well as future work beyond this thesis are given.

Chapter 2

Equine tendons

2.1 Anatomical Basics

As part of the skeletal system, tendons are the soft connective tissues, that connect muscles and bones to allow body locomotion. The junction between the tendon and the muscle is called myotendinous-junction (MTJ) and the region where the tendon inserts the bony structure, is called osteotendinous-junction (OTJ). The main task of tendons is to transmit forces and therefore enabling joint motion. In cursorial animals some tendons extended their simple positioning role to a more specialized one as energy storing elements. Similar to a spring, they increase the efficiency of locomotion by recuperating energy. Therefore tendons can be divided in flexor (energy-storing-) and extensor (positioning-) tendons. One example of a energy storing tendon is the equine superficial digital flexor tendon (SDFT), located on the posterior lower limb (see fig. 2.1 (a)). Together with other tendinous structures it is acting on the palmar location of the metacarpal region, to support the hyper-extended metacarpophalangeal joint during weight bearing (see fig. 2.1 (b,c)), by releasing energy when the limb is protracted [51]. A typical extensor tendon on the other hand is the equine common digital extensor tendon (CDET). It is located on the anterior lower limb (see fig. 2.1 (a)), originates from the common digital extensor muscle and inserts the end of the long and short pastern bones. The scientific relevance of these two equine tendon types is the fact, that the SDFT and the human Achilles tendon are functionally and clinically equivalent and no equally appropriate analogues in rodent, rabbit or other animals exist [42]. The CDET on the other hand is an ideal analogous to the human anterior tibialis [28]. This makes it possible to easily investigate pathologies like tendinopathy and also facilitated significant advances in changes during maturation and aging of tendons [42].

The molecular composition of tendons in general is dominated by a proteoglycan water matrix, which is about two-thirds of the whole weight of the

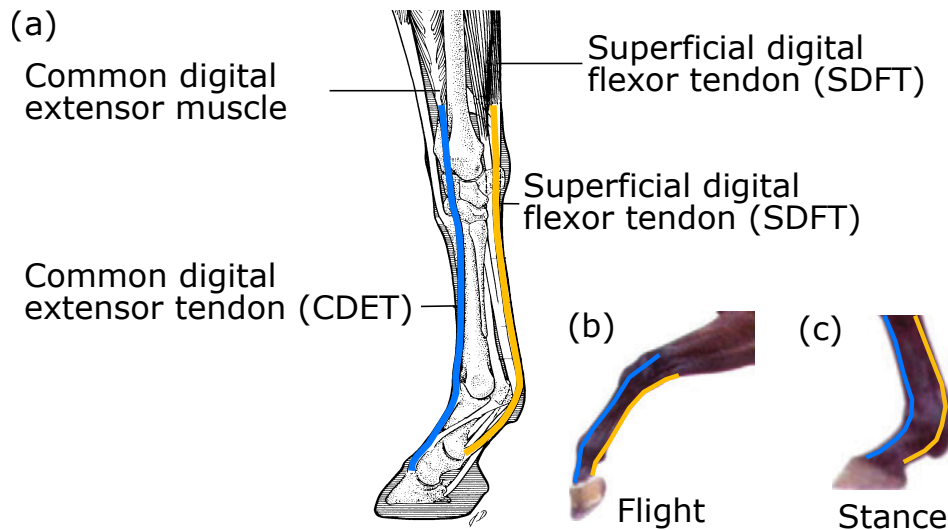


FIGURE 2.1: Illustration of the equine forelimb showing the SDFT and CDET (a) (adapted from [50]). The SDFT is much more extended during weight bearing than the CDET (b,c) (adapted from [6])

tendon in natural wet condition [51]. The remaining one third of the dry mass, mainly consists of collagen type I (65- 80%) and a small portion of elastin (1-2%) [27]. Tendons are multi-scale composites, built up in a hierarchic way by increasingly sized subunits from the molecular scale (nano-scale) to the tissue-organ (see fig. 2.2). The smallest distinguishable units with structural and mechanical function are the collagen fibrils. Collagen fibrils are long cylindrical-line structures that are built up from single tropocollagen molecules. Single fibrils assemble to collagen fibres, whereas these structures once again associate into tendon fascicle. Bundles of fascicle, which are already identifiable with naked eye on the cut surface of a tendon, finally built up the macroscale structure. Each of these bundles is enclosed by a fine sheath namely the endotenon or interfascicular matrix (IFM), which binds the bundles together. The IFM mainly consists of type III collagen and proteoglycans and is synthesized and maintained by a small amount of fibroblasts [56]. This zone furthermore also carries blood vessels, nerves and lymphatics to the deeper portion of the tendon [27]. A very important characteristic of the IFM is the fact, that it provides sliding between the individual bundles. This characteristic also contributes to the different mechanical properties of positioning and energy-storing tendons [59] and might also explain pathologic mutations of the tendon structure [56]. To provide a free movement against the surrounding tissue, the whole tendon is surrounded by the paratenon and directly beneath the epitenon [27].

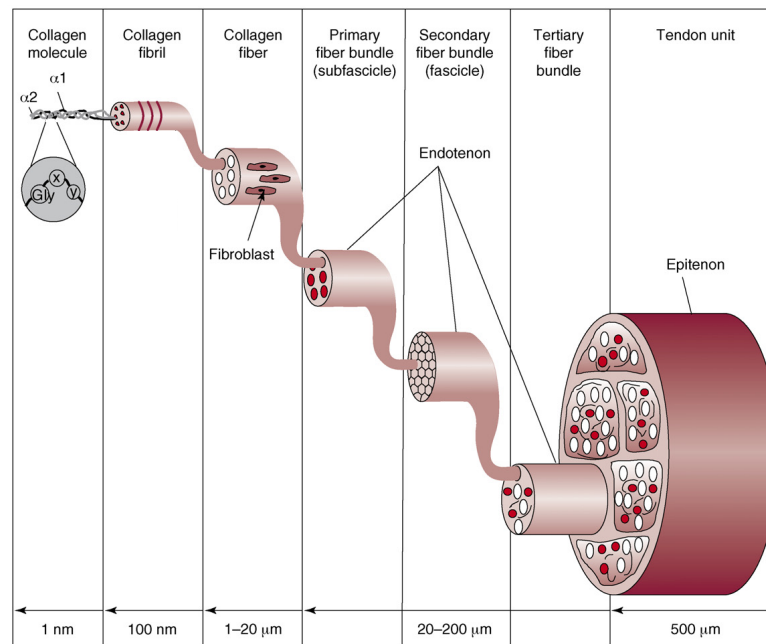


FIGURE 2.2: Schematic illustration of the hierarchical structure of a tendon. On the nano-scale tropocollagen molecules assemble to fibrils, which in further steps aggregate to fibres and fascicles and therefore building up the tendon. Each of this bundles is surrounded by a fine sheath called endotenon, or interfascicular matrix significantly influencing the mechanical properties (adapted from [31])

2.1.1 Collagen and collagen-fibrils

Collagen is not only the most dominant molecule in tendons, but also the most abundant insoluble fibrous protein in mammals [14]. Collagen is a super family of 28 chemically distinct proteins accounting 25% - 35% of the total protein mass [48]. Depending on the function of tissue, collagen types can be divided in fibril assembling collagen (collagen type I, III, V and XI [59]), fibril-associated collagen with interrupted triple helices (FACIT), network-forming collagen, anchoring fibrils, transmembrane collagen with interrupted triple helices (MACIT), basement membrane collagen and others with specific functions [48]. The molecular structure of collagen is distinct to other macromolecules. The tropocollagen molecule is made up by three polypeptide α -chains (not to be confused with α -helices). The α -helices wind up to make a triple-helix. The triple helix is a supertwist of the α chains driven by the amino acid glycine, which is positioned at every third residue along each α -chains. Collagen type I is build up from two $\alpha 1$ and one $\alpha 2$ chains aggregating the so called tropocollagen. This fibril-forming collagen molecule is ≈ 300 nm long and is 1.5 nm in diameter. The end of the tropocollagen are made by a non-helical N- and C-terminal telepeptides which are thought to play a role in tropocollagen molecules

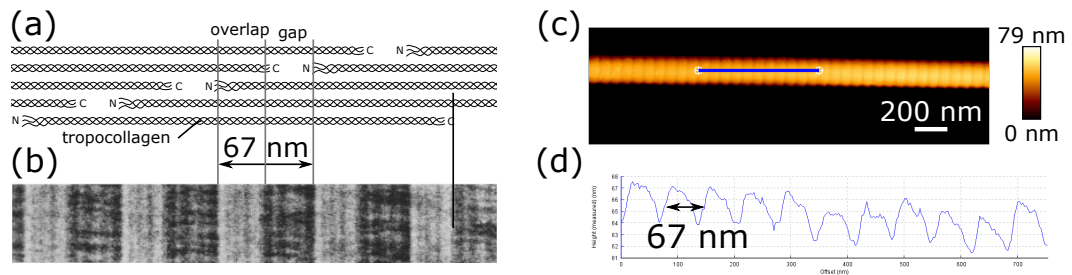


FIGURE 2.3: Tropocollagen aggregates to fibrils resulting in the typical D-banding shape. The periodical alternating (67 nm) pattern of dark and white regions (a, reproduced from [26]) can be seen in sodium phosphotungstic acid stained fibrils, imaged with a transmission electron microscope (b, [26]), as well as on fibrils (CDET from 18 years old horse) imaged in contact mode in air, with the AFM (c). (d) Shows the height profile of the fibril in the blue region shown in (c).

to a fibril. These fibrils assemble in the tissue in a very specific wavy like pattern, known as crimp (see fig. 2.4). As this pattern is able to stretch during tendon elongation, the shape is directly linked to mechanical properties of different tendon types. Collagen fibrils in general are build up in a specific easily identifiable structure. The tropocollagen molecules are stacked together in a way that each molecule overlaps quarter of the adjacent one. This leads to the so called D-banding (described by a model of Petruska and Hodge), which is visible as periodically alternating light and dark regions along the longitudinal axis of the fibril. The distance in between these regions is ≈ 67 nm [43] (see fig. 2.3).

2.1.2 Collagen crosslinking

The structural stability and mechanical integrity of collagen fibrils is maintained by collagen crosslinks, divided in enzymatic driven by the enzymatic lysyl oxidase (LOX) and non-enzymatic cross-links, driven by a non-enzymatic post-translational modification of proteins occurring through the Maillard from sugars with amino acids.

Interfibrillar crosslinking

Due to the LOX enzyme, first divalent immature molecules dihydroxylysinonorleucine (DHLNL) and hydroxylysinonorleucine (HLNL) are formed. This crosslinks are transformed during maturation to the trivalent crosslinks pyridinoline (PYD), deoxypyridinoline (DPD) and pyrrolic analogues. Non-enzymatic crosslinks originate from a glycation process, where extracellular sugars spontaneously

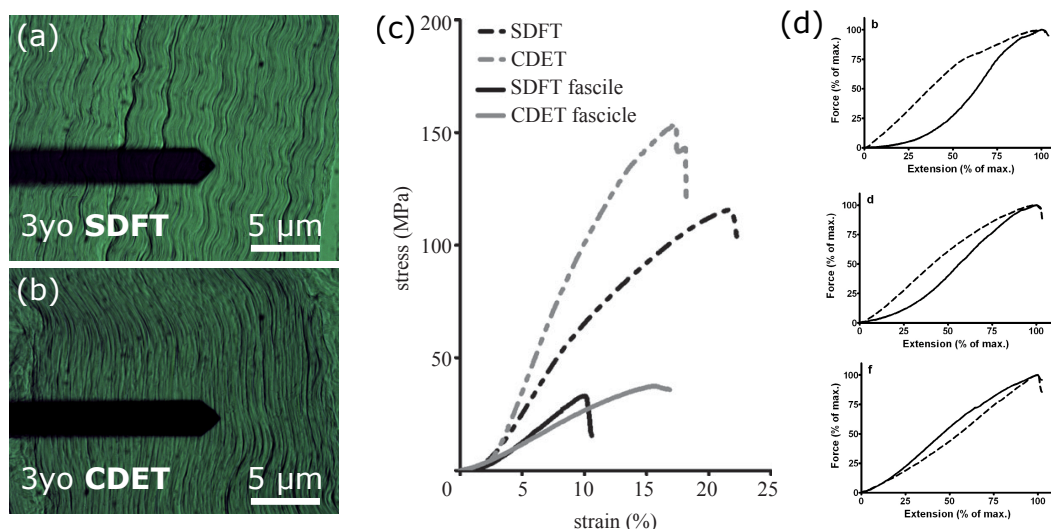


FIGURE 2.4: Fibrils assemble in the tendon in a very specific wavy like formation, called crimp. This shape was suggested being in charge for mechanical properties of the tendon. SDFT-tissue (a) from a 3 years old horse shows more crimp with larger crimp angles and a smaller crimp base length than in the CDET (b) of a horse with the same age. Crimp was related to the shape of the toe region of a tendons stress strain curve. The toe region of the SDFT tendon on the tissue- and fascicular level is much bigger than in the CDET tendon and therefore supports the importance to mechanical properties (c) (adapted from [58]). During ageing the toe region of the normalized force-extension curves of a SDFT IFM becomes smaller which might be in charge for fibrils being loaded at lower strain rates and therefore being damaged and inducing tendinopathy (d) [56]

react with amino acid side groups on proteins, forming molecular entities, called advanced glycation end products (AGEs) [18].

Enzymatic crosslinking

Enzymatic crosslinks always occur between the telepeptides and the neighbored collagen chains, whereas non-enzymatic crosslinks can emerge between any positions on the tropocollagens (see fig. 2.5 (a)). Investigations on SDFT and CDET tendons have shown, that Interfibrillar crosslinks differ according to the type of the tendon. Whereas the predominant mature crosslink in the SDFT was hydroxylysylpyridinoline, the most abundant one in the CDET was histidinohydroxymesodesmosine. Differences were also found according the HLNL, a major crosslink in skin, existing in the CDET but not in the SDFT [6]. These lead to the suggestion that intermolecular crosslinking could highly influences the mechanical properties of tendons. AGEs furthermore were clearly associated to stiffening and brittleness of the tendon tissue, in studies were tendons were incubated by a range of sugars and aldehydes, strengthening this suggestion [16].

Intrafibrillar crosslinking

Collagen fibrils assemble into fibres by increased packing of fibrils to fibres is facilitated by transfibrillar cross-linking molecules. This is done by macromolecules, in tendons mainly proteoglycans (PGs) and fibronectin [61]. Proteoglycans make up just about 1% of the total dry mass of most tensile tendons [62]. These molecules are build up by a "core-protein" which is directly linked to the tropocollagen and sugar molecules called glycosaminoglycans (GAG), which are covalently bonded to the core protein. The most abundant PG is a small molecule called decorin. Proteoglycans have shown to play an important role in tendon mechanics, by providing a viscous environment and therefore allowing collagen fibres to stretch and dissipating the force of sudden loads [13]. PGs are suggested to be lubricating units moving relatively to each other [61]. Investigations on the SDFT and the CDET have shown differences in the amount and the type of PGs on the inter-fibrillar and inter-fascicular level [57]. Furthermore investigating the fascicular (FM) and interfascicular matrix (IFM) of these tendons showed the overall amount of proteoglycans being higher in the SDFT than in the CDET and also being more dominant in the IFM than in the FM.

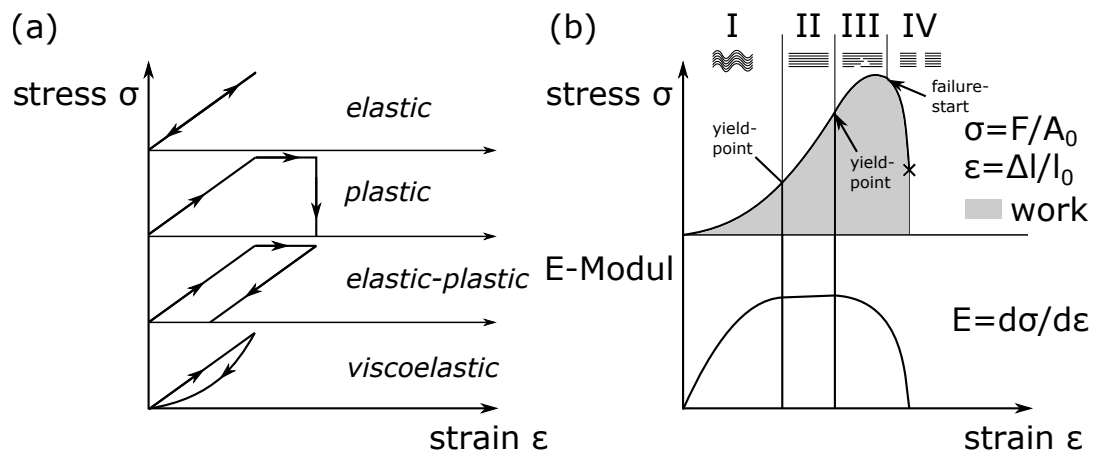


FIGURE 2.6: Material properties can be classified as elastic, plastic, viscous and mixtures of those (a). Tendon are highly anisotropic, leading to a specific stress- strain curve. In the toe (I) region several fibrils loose their wavy structure and align. The elastic region (II) is characterised by elastic reversible stretching of the already aligned fibrils. The plastic region (III) starts from the yield point, where the tissue begins to be damaged due to micro fractions in the fibril structure. From the failure point on, the whole tendon tissue fails (IV).

2.2 Mechanical properties

Mechanical properties describe how a material responds to an external mechanical load. Common materials behave different, whether the external force is static (constant over a certain period of time) or dynamic (load changes periodically, stochastically or even appears as a single impact) and therefore their properties can be roughly classified in static and dynamic material properties. Typical experiments to classify the materials characteristics are uniaxial-stress, tensile, shearing, three-point-bending, indentation and notched-bar-impact tests. Most of these tests are based on continuously or intermittently recording the force applied on the sample and the deformation simultaneously. Thereby material characteristics like hardness, elastic modulus, creep-properties, viscoelasticity, elongation and force at break, ultimate force etc. are deduced. Materials can be classified as elastic, plastic, viscous or a mixture of those properties (see fig. 2.6 (a)). Biological tissues are highly anisotropic complex structures consisting of elastic, plastic and viscous elements.

2.2.1 Tendon

A typical-stress strain resulting from a tensile test is shown in fig. 2.6. The whole curve can be divided in four main zones:

- I Toe zone: The nonlinear region is due to stretching of the wavy crimp-like like arrangement of the fibrils.
- II Elastic zone: In this linear region of the stress-strain relationship stretching of the tendon is still reversible and in case of removing the force the tendon returns to it's initial shape. The slope of the graph in this region defines the elastic modulus E. The linear zone ends with the yield point.
- III Plastic zone: Further stretching of the tendon induces microfractures in the fibril structure.
- IV Material failure: Further stretching leads to a fatal failure of the tendon

As the SDFT and the CDET are flexor- and extensor- tendons respectively several differences also exist according their mechanical properties. These are discussed bellow.

Superficial digital flexor tendon

Flexor tendons are in charge for increasing locomotion efficiency. Investigations on the SDFT showed an maximal recovery of mechanical work of 40%, when the horse changes from walk to slow trot and 36% when changing from walk to gallop [3]. Using a Hall-effect strain sensor, maximum strains in vivo of 7.6% at trot and 16.6% at gallop were measured [52]. In vitro ultimate strain of the SDFT was shown to be 25.98% [6]. This data leads to the suggestion, that injuries in tendons, like the SDFT and the human Achilles tendon, are likely as the safety margin is quite low. Furthermore the ultimate stress and the elastic modulus of this tendon is 115.74 MPa and 970.8 MPa respectively [6]. The morphology of the fibrils crimp in the SDFT (see fig. 2.4 (a)) shows a high density of wavy structures with large crimp angles and small crimp base lengths. This leads to the suggestion of giving the tissue more ability to stretch at the low strains leading to a larger toe region in the stress-strain relation (see fig. 2.4 (c)).

Common digital extensor tendon

The main tasks of positioning tendons is to directly transmit the force to the bone produced in the muscle to the bone. Investigations on the fibril morphology of the CDET have shown crimp with small crimp angles and long crimp base lengths [3]. This characteristic could also be observed on CDET samples in this thesis (2.4 (b)) and leads to the suggestion of being also in charge for a

narrower toe region in the stress strain relationship on the tissue and even more on the fascicular level (see fig. 2.4 (c)). Maximum in vivo strains in the tendon were estimated with 3% and in vitro failure strains of 20.45% showing a much higher safety margin, which explains why injuries in this type of tendons are not that common, as in flexor tendons [6]. The maximum stress being measured in vitro is 136 MPa with an elastic modulus of 1236.3 MPa [6].

Investigations through tensile tests on SDFTs and CDETs on the tissue and fascicular (FM and IFM) level have shown that differences on the macroscale level are mainly related to mechanical properties of the IFM and less attributable to differences in single fascicles [58]. The linear moduli of single fascicles of the CDET (335.82 MPa) and the SDFT (310.24 MPa) showed no significant differences and were interestingly much lower than the elastic modulus of the whole tendon (CDET= 613.8 MPa; SDFT= 1012.26 MPa). Interestingly failure strain differences between the CDET and the SDFT on the gross level inversely behave to those on the fascicular level. While the failure strain on the tissue level is higher for the SDFT tendon, this is not the case for individual fascicles. This leads to the hypothesis that the IFM achieves the strain rates on the tissue level.

2.2.2 Age-related changes in the tendon

One main characteristic of biological materials is the changes of their chemical structure due to ageing and external loads. Investigations on this topic are very important to develop ideal training routines according the age and the intensity to prevent injuries and to achieve best results. Furthermore it is also important to develop ideal therapies for specific pathologies (e.g. tendinopathy common in human and horses), which are more likely in old tendons. Investigations [56] on the FM and IFM of SDFTs and CDETs from 3 to 20 years old equines showed, that the mechanical properties of the whole tendon did not alter significantly during ageing. Single fascicles did not show any significant differences from the SDFT and on the CDET but the strain at failure showed changes during ageing. Also the mechanical properties of the IFM of each tendon (extension at failure, force at failure) did not significantly change during ageing. Only the extension at failure of the IFM from the old CDET was higher than the one from the old SDFT. Real changes in the force-extension graphs of the IFM of the SDFT. The toe region became much smaller with increasing age (see solid line in fig. 2.4 (d)). A large toe region enables large extension at minimal force. As the region becomes smaller the fascicles therefore become loaded earlier when the tendon is loaded and therefore fascicles from old tendons might be more

likely damaged when the tendon is operated in the common extension range during locomotion.

Chapter 3

Atomic force microscopy

3.1 The atomic force microscope

The atomic force microscope (AFM), member of the scanning probe microscope (SPM) family, was first described in 1986 by Binnig et al. [4]. The main characteristic of SPMs is a sharp probe, brought close to the surface of interest. Because of the small distance between the probe and the surface (several nm), forces between the surface and the probe are generated. The magnitude of the interaction forces are related to the distance between the probe and the sample. Keeping the resulting interaction forces constant by controlling the z-position of the tip, while it is scanned over a surface, high resolution images can be obtained. The fact, that there are no specific requirements for the specimen material or the environment it is being tested in, distinguishes the AFM from other SPM and high-resolution imaging techniques (e.g. SEM etc.). Measuring with the scanning tunneling microscope (STM) for example, requires that the surface is conductive [5]. Therefore non-conductive specimens have to be coated with a specific metal layer. This makes it impossible to measure biological samples (i.e. cells, proteins and tissues) or polymers in their native state. Current technological advances in AFM have made the technique highly attractive for the field of life sciences. It is possible to measure samples in near physiological environments (hydration in salt solutions, adjusted pH and temperature). Additionally, the mechanical properties can be mapped across the surface topography of the sample. This allows co-localization with specific structural characteristics and elements of the sample surface enabling in certain circumstances to infer the structure-mechanical relations, which is important for understanding the function of biological samples.

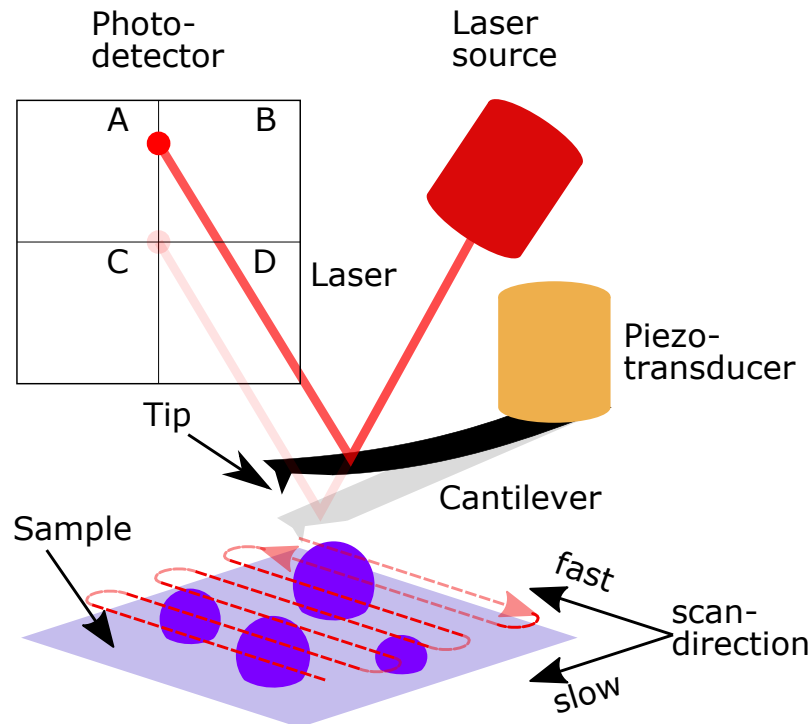


FIGURE 3.1: Due to the interaction of the tip and the surface the cantilever (CL) is bent. The laser, produced by the laser source and reflected off the upper side of the CL, therefore hits the photodetector at a position shifted from the neutral center position. Recording these changes leads to a high-resolution image of the surface.

3.1.1 Basic AFM-setup and measurement principle

Fig. 3.1 shows the main parts of a commonly used AFM (cantilever, piezo-electric-transducer, laser and photodetector) and its basic measurement principle. The heart and also most important component of the AFM is the cantilever with its tip on the very end side. The detection system, translating the bending of the cantilever into an electrical signal in most cases consists of a laser beam produced by the laser source and the photodetector. The movement of the cantilever is usually administered by a piezo electric transducer.

Measurement principle

The AFM was initially developed to measure sample topographies. The basic principle is shown in fig. 3.1. Thereby the cantilever is brought directly in contact with the surface or close enough to feel long- or short-range surface forces (i.e. Van der Waals forces) and is then scanned over the sample row-by-row, resulting in a slow and fast scanning direction. Due to the sample's topography the cantilever is bent. This bending can be translated into a high resolution image of the surface using different detection methods like the optical lever

method, which is most commonly applied in current AFMs. Other methods available are e.g. the interferometry-, the capacitive sensor- and piezoresistive/pieoelectric method. The AFM used in this thesis also operated with the optical lever method. In the following sections therefore this, but also the other more uncommon detection methods are described.

Detection methods

Optical lever method

The beam bounce or optical lever technique is the most commonly used detection method in nowadays AFMs [44]. Here a laser is reflected off the upper side of the cantilever, towards a photo-detector (fig 3.1). The photodetector is commonly divided in four quadrants, separated by a vertical and a horizontal line. By comparing the electrical signals of the different quadrants, the movement of the lever is estimated. Referring to the labeling of quadrants of the photodetector, with A, B, C, D as in fig 3.1, the deflection of the cantilever is calculated by comparing the signals $A + B$ versus $C + D$, whereas the torsional bending or lateral deflection results from calculations of the $A + C$ vs $B + D$ signal data [9]. It is important to point out here that this technique does not directly measure the deflection on the very end of the cantilever, where the force is initiated, but rather the slope of the cantilever at the position where the laser is reflected. If the laser is exactly positioned over the tip (the position where the force is initiated) the Euler- Bernoulli beam theory can be used to connect the change of the slope (so the change in voltage of the photo-detector) and the deflection by

$$\left(\frac{dw}{dx}\right)_T = \frac{3}{2l}w_{max} \quad (3.1)$$

with $\left(\frac{dw}{dx}\right)_T$ as the slope and w_{max} as the vertical deflection of the tip [2]. Equation 3.1 is valid, as long the laser is reflected from the same position (exactly over the tip) and the cantilever keeps the same length l (m).

Practically the most common way to relate the change of the photo-detector voltage signal with the deflection (sensitivity) of the cantilever is a calibration procedure, which is mandatory before each experiment. Here the cantilever is brought into contact and deflects over a very hard surface (glas, mica). Assuming the AFM tip not indenting into the surface of the very stiff substrate, the

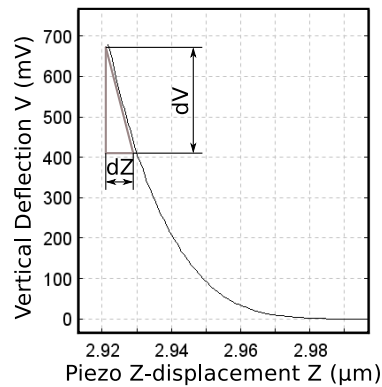


FIGURE 3.2: Because the substrate is much stiffer than the cantilever, the piezo movement is completely translated into cantilever deflection leading to a linear part in the upper curve region. The slope of this linear part is defining the sensitivity.

whole movement of the piezo is translated into cantilever deflection. Measuring the slope of the deflection- piezo movement curve in the upper linear region leads to the inverse of optical lever sensitivity (see fig 3.2).

$$\text{sensitivity} = \frac{dZ}{dV}, (\text{nm} \cdot \text{Volts}^{-1}) \quad (3.2)$$

Interferometry

Another optical method, to measure the bending of the cantilever, is based on interferometry between a laser beam, which is reflected from the cantilever and a reference beam. This technique is very sensitive and measures directly absolute small displacements of the CL. [44]. This method is able to cope with large deflections and the signal to noise ratio is superior over the optical lever method. However, AFMs based on interferometry are more difficult to setup, require an optical table for sufficient vibration and acoustic isolation and are susceptible to thermal drift and variation in laser frequency [33, p.18].

Capacitive Sensor

Capacitive sensors are based on the principle that two conductive plates separated from each other, have a specific capacity (cf. capacitor) when voltage is applied between the plates. Changing the gap between the plates, also changes the capacity which can be measured. This characteristic can be used if one of the plates is the bending cantilever and the second one is a rigid part of the chip parallel to the CL. The advantage against optical techniques is that these kind of sensors are much smaller, do not need any alignment of the laser and

just consist of reactive components, which keep them free of parasitic resistive noise [7]. Furthermore, this technique is very sensitive and measures the absolute displacement. The main disadvantage is the small gap between the CL and the rigid electrode (1 μm), which limits the roughness of the specimen that can be scanned. Moreover, the capacitive sensor cannot be used in electrolyte solutions because of Faradic currents. This is perhaps the greatest disadvantage of the capacitive sensor, as it cannot be used for experiments on biological tissues, that have to be maintained hydrated in solution during the experiment. [60].

Piezoresistive/ piezoelectric cantilevers

Embedding piezoelectric layers in the cross-section of the cantilever makes it possible to measure the stress, while the CL is bending, which directly represents the deflection. The advantages of this technique are the same as for the capacitive type sensors, extended with the possibility to also measure in non-transparent solutions. Nevertheless the architecture of such CLs is complex and therefore commercial availability is limited ([44][24]).

3.1.2 Cantilever and tip

The cantilever with its tip on the very end bottom side is one of the most important parts of the AFM and can be seen as a mechanical spring (see 3.3). Cantilevers with different spring constants (e.g stiffnesses) exist (0.006 N/m¹- 450 N/m²). The stiffness is directly linked to the first harmonic of oscillation, a fact, which is on the one hand used to analyse cantilever spring constants. This is necessary as manufacturers provide them with large fluctuation margins. Cantilever stiffness is also directly related to high imaging speed in oscillation modes (AC-mode). When using the AFM for imaging, either soft cantilevers are used in contact mode, to prevent damaging of the surface or stiffer ones in AC modes such that high enough frequencies can be generated. Generally the maximum achievable scan rates described in [15] by

$$v \ll \frac{\lambda D_v}{2m} \quad (3.3)$$

with v (m/s) being the maximum achievable velocity, λ_t (m) the periodicity of surface topography, D_v (Ns/m) the damping, k the cantilever spring constant, m (kg) the effective cantilever mass, in case of low damping occurs. These

¹ <http://probe.olympus-global.com> access on 10.01.2017

² <http://www.brukerafmprobes.com> access on 10.01.2017

equations show that higher velocities can be reached if the spring constant is increased and the mass is decreased which results in using short stiff cantilevers for high speed imaging.

When investigating the mechanical characteristics of materials by doing AFM-type indentation experiments, it's important that the cantilever stiffness is similar to the stiffness of the sample being tested. This comes from the fact that cantilevers which are too soft do not indent into the sample and therefore the deflection does not gain any information about the material. If the cantilever is too stiff on the other hand, the tip indents but no deflection signal is generated. Cantilevers also come in different shapes (described in more detail in sec. 4.2.1). Most common are triangular and rectangular ones (fig. 3.3 (a)). It was initially suggested that the V-shaped CLs are less sensitive to lateral forces. However, Sader showed in an analytical approach [46] that actually V-shaped CLs are less resistance to lateral forces, which are not desirable in scanning as they might lead to damage of the sample or the probe. The author(s) also suggested that a rectangular shape should be preferred for scanning in both, contact- or non-contact imaging modes. Conversely having a higher lateral sensitivity, lateral forces can be an advantage in friction measurements, which can make V-shaped CLs attractive for such experiments [46]. Typical rectangular cantilevers have a length from 90-500³ μm and a width from 25-50³ μm . Due to this very small geometry, CLs are generally attached to a larger chip, which makes handling and fixation in the AFM holder possible.

Commonly used materials for CLs are silicon (Si) or silicon nitride (SiN). Conventionally CLs are made via lithography and etching. To increase the reflectance of the laser, the top side of the CL is often coated with gold [44] or aluminium. Also other coatings like platinum (Pt), chromium (Cr), diamond or cobalt (Co) are available, to make the tip surface more resistance against damage, or to interrogate material properties, such as the magnetic structure of the surface via magnetic force microscopy. The tip, located on the very end bottom side of the CL is the only part of the AFM, which is physically directly interacting with the surface. Therefore it is clear, that its properties play an important role for interpretation of these interactions.

³ MikroMasch[®] SPM probes & test structures product catalogue 2015

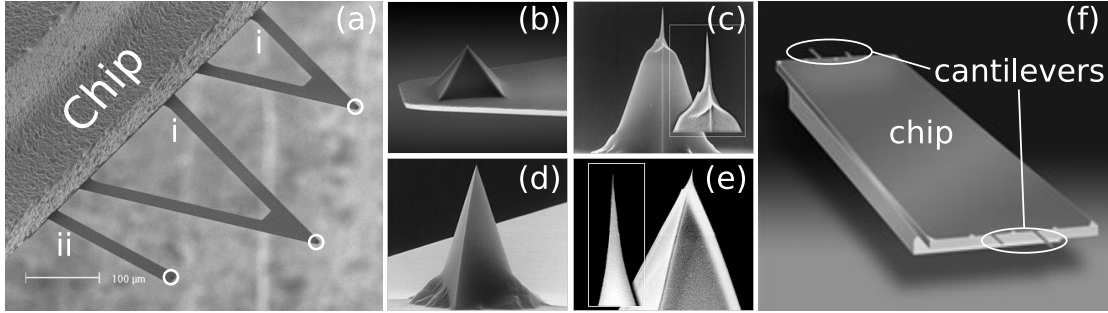


FIGURE 3.3: (a) Different shapes of cantilevers: V-shape (i), rectangular (ii) white circles represent position of the tips [8], (b)-(e) different tips [36][34][35][37], (f) chip with four rectangular cantilevers [36]

3.2 Imaging modes

Depending on the properties (stiffness, roughness etc.) of the sample, different imaging modes are available. In all of these modes the cantilever is scanned over the surface as shown by the red track in fig. 3.1. The main difference of the modes is given by the distance between the AFM cantilever tip and the surface (tip-sample separation) while the tip scans over the surface and whether the cantilever is externally oscillated (AC-modes) or not. Depending on the size of the tip-sample separation, also different surface forces act on the cantilever. The Lennard-Jones potential, presented in the following section, shows the dependency of specific long-range or short-range forces, which makes it also possible to present and describe the different imaging modes in more detail (see fig. 3.4).

Lennard-Jones potential

The Lennard-Jones potential is a simple approximation for the interaction between two particles/ surfaces including the long-range attractive Van der Waals- and the short-range electron shell repulsion forces. These are the forces mainly being measured with the AFM. It can be written as

$$w(r) = 4 \cdot \epsilon \left[\left(\frac{\sigma}{r} \right)^{12} - \left(\frac{\sigma}{r} \right)^6 \right] = -\frac{A}{r^6} + \frac{B}{r^{12}} \quad (3.4)$$

with ϵ as the depth of the local minimum of the potential energy, σ (m) the distance where the Lennard-Jones potential becomes zero, r (m) the distance between particles and, A and B as the attractive and repulsive components, respectively [9]. The very right-hand side of the diagram (see fig. 3.4) is the area where no interaction between the cantilever tip and the surface appears

as the cantilever is too far from the sample. Decreasing the distance the tip is first being pulled towards the surface due to the longer range Van der Waals forces (attractive zone). While further extending the piezo, the tip gets that close to the surface that it feels the short-range electron shell repulsion forces (repulsive zone), which are more dominant at this distances. In general the attraction zone is smaller than the repulsion zone. The three main imaging modes (contact-, intermitten- and non-contact mode) are acting in the attraction, the repulsive or in both zones (see fig. 3.4). The contact mode which was historically the first mode, is conventionally performed only in the repulsive zone, as the tip is in direct contact with the surface all the time. The non-contact mode, performed by oscillating the cantilever very close to the surface, on the other hand is operating only in the attractive zone. This mode gives the possibility to image the sample without being in direct contact with the surface and therefore avoiding damaging of the sample or the AFM tip. However, in this mode it is complicated to define the correct parameters to guarantee imaging in the attractive zone only. A mixture of these two modes and therefore a more user-friendly mode is the intermitten-contact-mode, which also counts to the oscillating modes but where the CL tip is periodically in contact with the surface. Therefore, this mode is overlapping between the repulsive and the attractive zone. These three modes are presented in more detail in the following sections.

3.2.1 Contact mode

In this mode, the tip remains in contact with the sample surface throughout imaging. Nevertheless, this mode can be divided in two different types, depending on whether the deflection (force) or the height of the CL is controlled ((i) constant height, (ii) constant deflection). Constant height means, that the piezo is extended to a certain length, while the tip is scanning over the surface. The topography is thereby directly derived from the change in deflection. During constant-height imaging the deflection, i.e. the force between the CL and the sample surface changes, which can lead to damaging of the sample or the tip. Therefore, this mode is not popular at all. A different approach employing constant deflection which is achieved by a feedback loop (see 3.2.5). In brief, when the cantilever starts to deflect, due to a change of topography, the piezo extends or retracts, to keep the predefined deflection constant. Scanning in contact mode is the simplest way of imaging a surface with the AFM. Other

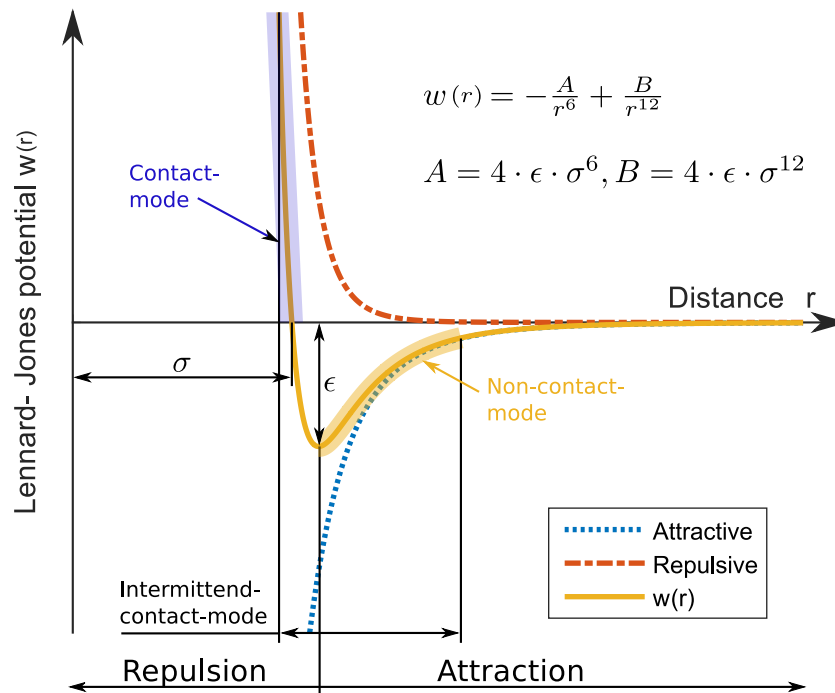


FIGURE 3.4: Lennard-Jones potential curve with the typical AFM imaging modes. (adapted from [9, p.37]). The blue dotted line shows the attractive Van der Waals forces whereas the red dot-dashed line shows the short-range electron shell repulsion forces. These forces combined result in the Lennard-Jones potential $w(r)$ (yellow)

drawbacks of this mode are underestimation of height when imaging soft samples, tip wear which can't be completely avoided and contamination of the tip with sample material picked up during imaging. So the contact mode should just be preferred if stiff surfaces, with a smooth topography, are investigated [9, p. 9]. Typically CLs used in this mode have a stiffness of $k=0.01 \text{ N/m}-1.0 \text{ N/m}$ and a resonance frequency of $f_r=7-50 \text{ kHz}$. These soft CLs minimize the force between the CL and the sample surface and therefore reduce the problem of damaging the surface, or the tip [33, p. 38]. User given setpoints in this mode are the deflection of the cantilever or the height, the piezo should be extended depending on whether imaging is done with constant height or constant deflection. The recorded channels in this mode are the Error signal (vertical deflection signal subtracted by the setpoint), height, height measured, lateral deflection and vertical deflection.

Resolving the variations of the surface topography of the sample is limited by the aspect ratio of the AFM tip. Manufacturers therefore offer high- and low aspect ratio tips 3.3 (c),(e). Imaging a surface results in a convolution of the tip geometry and the topography of the surface also known as envelope effect. If the object being imaged is very sharp (i.e step) the image directly represents the

tip geometry 3.5 (II). This phenomena can be used to determine the exact geometry of the tip, which is necessary in indentation- type AFM (see 3.4). Channels which are recorded in this mode are the error signal, height, measured height, vertical deflection and lateral deflection.

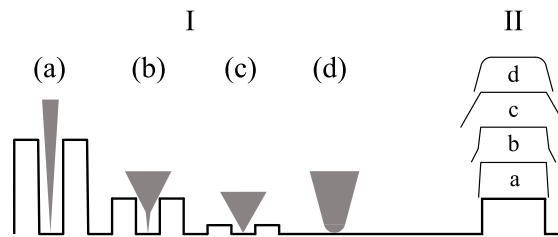


FIGURE 3.5: (I) The shape of the tip mainly influences the depth of the field of an image . (a) High aspect ratio tip, (b) low aspect ratio tip with sharp apex (c) low aspect ratio tip, (d) blunt or rounded tip. (II) Results of scanning a step with different types of tips . (adapted from [33, p.13])

3.2.2 Intermittent mode

The intermittent-, tapping or AC-mode overcomes the problem of lateral forces and reduces tip wear and the possibility of contamination generated during contact mode. In this mode, the cantilever oscillates close to its resonance frequency and at a certain oscillating amplitude over the surface. Topography variations change the oscillation amplitude. For example, the oscillation amplitude decreases when the tip meets an increase in height of the topography. Then the piezo drives the cantilever upwards to reach the user given setpoint of amplitude. The movement of the piezo is equal to the size of the change in height topography. Measuring the changes in piezo movement gives a direct estimation of the height topography of the sample surface. When measuring in air adhesion forces caused by thin layers of absorbed water can cause artefacts or issues. Cantilevers with higher stiffness are used to allow the AFM tip to penetrate the thin water layer and reach the sample surface ($k=7 \text{ N/m}$ - 60 N/m $f=250 \text{ kHz}$ - 350 kHz [33, p. 38]). However, softer CLs can be used when imaging in fluid. This mode can be further applied to extract mechanical and adhesive characteristics of a surface, as the phase of the drive and the oscillation frequency changes, if variations of these properties occur [9, p. 9]. Channels which are recorded in this mode are the height, amplitude and phase.

3.2.3 QI-Mode

The quantitative imaging mode (QI-mode) is a force curve based imaging technique with the main benefit compared to the other conventional contact- and AC-mode, that there is no need for setpoint or gain adjustment while scanning the sample. Thereby the tip is quickly imaging the surface in a specific user defined pattern, producing one whole force-curve for each pixel. Automatically quick analysis of these curves by the software gives the user the possibility to precisely control the force and therefore even a height image at zero force can be calculated. Well known drawbacks of conventional imaging modes like damaging or moving very soft or loosely attached samples in contact mode due to lateral forces can thereby be solved when using this mode. In conventional AC mode it's also not possible to directly control the vertical force which can also lead to compression of the sample and leading to problems during imaging. The QI-mode is furthermore independent of cantilever stiffness and therefore the user can freely choose whether he wants to use cantilevers $k < 0.01$ N/m for imaging very soft or loosely attached samples or if hard samples are investigated according their mechanical properties which calls for cantilever with spring constants $k > 40$ N/m. Another big advantage of this mode is that each of the pixel-wise produced force curve is recorded and analysed automatically at once which makes it possible to simultaneously get high resolution topography information combined with the mechanical properties of the sample at a same speeds as imaging with conventional modes. The QI-mode therefore was also the ideal candidate for investigating individual collagen fibrils in PBS to quickly find a proper position on the sample consisting of enough individual fibrils without moving them due to the loose contact with the glass slide. Channels which are recorded in this mode are the height, measured height, adhesion and slope calculated from the force curves. Here the channels height, measured height and the slope are calculated from the extend curves. the adhesion channel is calculated from the retract curve.

3.2.4 Non- contact mode

In this mode the cantilever is also oscillating, similar as in the intermittent mode. The main difference in this mode is that the tip never gets in contact with the surface. Furthermore the amplitude is much smaller and just the differences between the CLs- and the driving oscillation frequencies are measured.

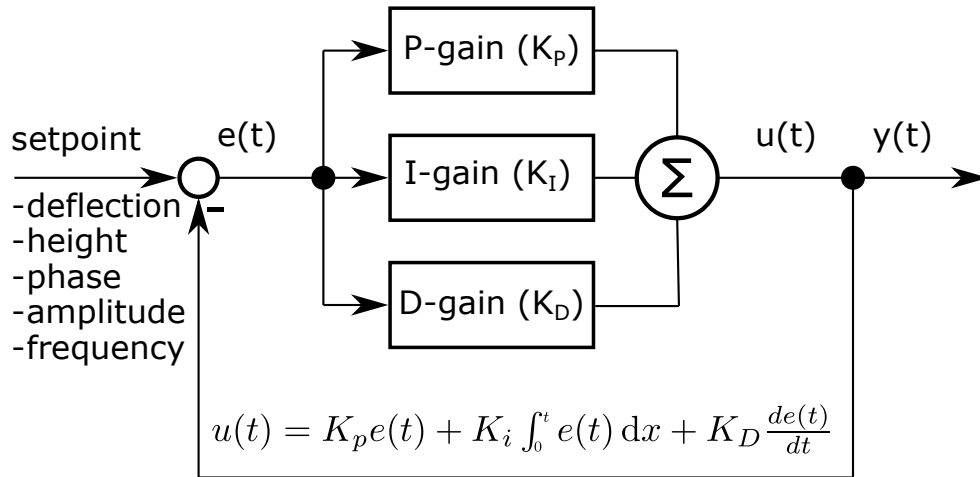


FIGURE 3.6: Shows the blockdiagram with the three gains, proportional gain (K_P), the integral gain (K_I) and the differential gain (K_D), whereas the first two can commonly be adjusted by the user.

In a further step they are also used as an input for controlling the piezo, to prevent the tip from coming into contact. The shifting of the frequencies occur when the tip is brought that close to the surface, where long range interactions like Van-der Wals and electrostatic forces are generated between the tip and the surface. [12, p. 11]. Cantilevers typically used for this mode have a stiffness of $k=0.5 \text{ N/m} - 5 \text{ N/m}$ and a resonance frequency of $f_r=50 \text{ kHz} - 120 \text{ kHz}$ [33, p. 38]. The channels being recorded in this mode are the height, amplitude and phase

3.2.5 Feedback control loop

For all imaging modes, except the "constant height contact mode" (the piezo height is not changed during imaging), it is necessary to adjust the position of the cantilever to keep the control parameters (i.e deflection, oscillation amplitude, etc.) constant. This is done, by changing the height of the piezo, which is desirable to be performed as fast and accurate as possible. AFMs therefore commonly use (P)roportional (I)ntegral (D)ifferential - controller (PID). Figure 3.7 schematically shows how the PID controller works and fig. 3.6 shows a block diagram of the controlling principle. A specific setpoint of deflection or oscillation amplitude is defined by the user, while the controller tries to maintain this setpoint, by changing the length of the piezo. The proportional term of the controller thereby amplifies the error between the signal and the setpoint, to establish the size of the correction signal required.

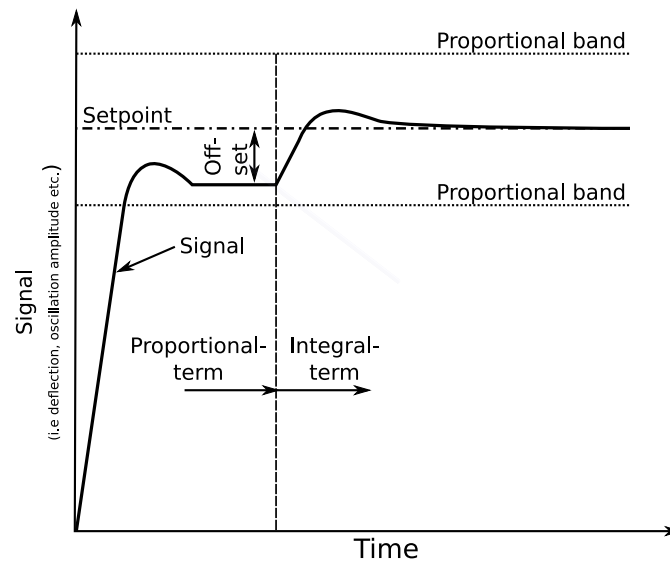


FIGURE 3.7: A certain setpoint is predefined by the user. The proportional term minimizes the offset by multiplying it with a proportional factor (a final offset still remains). The integral term sums (integrates) the offset over a certain time (eliminates the offset completely). reproduced and adapted from [33, p. 26]

This is done by defining a proportional band. Its size is some percentage of the total span of the controller and the actual percentage is the gain. The width of the proportional band defines how much the controller reacts to an error signal (i.e. proportional gain of 2 results from a bandwidth of 50% and a proportional gain of 4 results from a bandwidth of 24%). Because the offset is always amplified by a constant proportional factor, K_p it is not possible to reach exactly the set-point. This means that the signal always settles above or below the predefined value. Theoretically the offset could be decreased by making the proportional bandwidth smaller (by increasing the P-gain). This can hardly be realised as the signal always has to be in between the proportional bandwidth to prevent oscillations of the controller. To eliminate the offset totally, an integral term is used which sums (integrates) the error over a small time period and amplifies the sum with a specific integral factor K_i . It is important that the integrating time is not smaller than the reaction time of the piezo, as otherwise oscillations occur. The last part of the AFM controller is the derivative term, which reacts proportional to the changing rate of the signal. It prevents the system of erratic behaviour, as it responds quickly to large deviations. This term is also useful for reacting to small perturbations close to the setpoint. Commonly AFM users can control the proportional gain and the feed integral gain whereas the differential gain is controlled automatically. Thereby a good rule of thumb is to set the proportional gain 10-100 times higher than the integral gain [33, p.

26-27]. In practice it is common, adapting the I- and the P-gain during scanning so starting with low values and then slightly increasing the I-gain, up to a point just before oscillations occur and afterwards slightly increasing the P-gain. A good overlaying of the trace and the retrace signal during imaging (shown in the real time oscilloscope) indicates a well defined gain set-up.

3.3 Force measurements

The fact that the heart of the AFM, the cantilever, is a mechanical flat spring, enlarges the field of application from imaging, towards quantitative force measurements. Therefore interrogating the mechanical properties of materials is possible. Basically, a linear spring like the cantilever, provides a force which is directly proportional to its elongation (e.g. deflection). The proportional factor is thereby the spring constant k_c . In AFM the elongation is simply the deflection of the cantilever. Therefore Hooke's law which describes this physical relationship can be written in the following form

$$F = -k \cdot D \quad (3.5)$$

whereas F (N) is the force produced by the spring, where k (N/m) is the spring constant and D (m) the elongation from the neutral position. The minus in the equation is due to the fact, that F is always acting against its elongation. With this equation deflection vs. Z -displacement data can be transformed into force vs. Z -displacement curves by simply multiplying the deflection data with the cantilever's spring constant.

Cantilever stiffness calibration

The fact that k_c values, given by the manufacturer, usually fluctuate significantly around their nominal values, makes it necessary to determine the stiffness of the specific cantilever being used to do quantitative measurements.

One method to estimate the spring constant is to assume the cantilever to be an ideal rectangular beam with a certain length l (m), thickness t (m) and width b (m) (see. fig. 3.8). Furthermore assuming small deflections, the differential equation of the Euler-Bernoulli beam can be used,

$$\frac{d^2 w}{dx^2} = -\frac{M(x)}{E \cdot I} \quad (3.6)$$

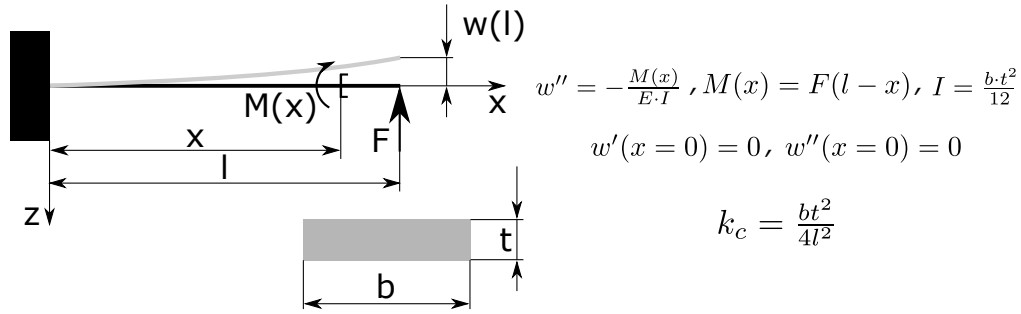


FIGURE 3.8: Assuming the cantilever having an ideal rectangular cross section with the thickness t the width b and a length l the Euler-Bernoulli theory can be used to calculate the spring constant k_c from these parameters.

with $\frac{d^2y}{dx^2}$ as the change in slope and $M(x)$ (Nm) the section moment at a certain position x (m), E (N/m²) as the elastic modulus and I (m⁴) as the 2nd moment of area. Using the boundary conditions $w''(x=0) = 0$ and $w'(x=0) = 0$ and the section moment $M(x=l) = F \cdot l$ with F (N) as contact force acting on the tip of the cantilever, the deflection on the very end of the cantilever is given by

$$w(x=l) = -F \frac{4l^3}{bt^3} = -\frac{F}{k} \quad (3.7)$$

and finally results in the spring constant

$$k = \frac{bt^3}{4l^3} \quad (3.8)$$

with k (N/m) as the cantilevers stiffness, b (m) as the cantilevers width, t (m) as the cantilevers thickness, l (m) as the cantilevers length. Therefore measuring the geometry and assuming a homogeneous material with a specific E makes it possible to directly calculate the spring constant k .

Another method to determine k_c , which was also used in this thesis, is the thermal noise method which is based on work of Hutter et. al [23]. Thereby the cantilever is defined as a harmonic oscillator. The fact that the mean square deflection of the cantilever $\langle \Delta D^2 \rangle$ is linked to the thermal fluctuation of the cantilever by

$$\frac{k}{\langle \Delta D^2 \rangle} = \frac{1}{2} k_B T \Rightarrow k = \frac{k_B T}{\langle \Delta D^2 \rangle} \quad (3.9)$$

with k_B (J/K) the Boltzmann's constant, T (K) the temperature D (m) the deflection and k (N/m) the stiffness of the cantilever provides an opportunity to determine k . The mean square deflection for an ideal spring is $\langle \Delta D^2 \rangle =$

$k_B T/k_c$. As the rectangular cantilever does not represent such ideal spring, several vibration modes are possible, resulting in a spectrum of a couple of peaks. Commonly just the first peak is taken for analysis, fitted with a Lorentzian curve and integrated to get the mean square deflection of that peak $\langle D_I^2 \rangle$. $\langle D_I^2 \rangle$ is linked to the total mean square deflection $\langle \Delta D^2 \rangle$ by $\langle D_I^2 \rangle = \beta \langle \Delta D^2 \rangle$ with $\beta = 0.971$. Another important fact which has to be taken into account and has already been mentioned before, is the fact that the optical lever method measures far more the inclination, than the deflection of a cantilever. The deflection and the inclination are proportional as shown in 3.1.1 in case of equilibrium, so for very slow motions. But that's not the case if the cantilever is oscillating very fast. This is taken into account by using the correction factor β^* . Finally the spring constant can be calculated by using

$$k = \beta^* \frac{k_b T}{\langle D_I^{*2} \rangle} \quad (3.10)$$

with D_I^* being the effective deflection derived by correcting the voltage-deflection signal with the sensitivity (e.g 3.2) and using the final correction factor $\beta^* = 0.817$ [12].

Another method having been used in this thesis to determine the cantilevers spring constant k is presented by Sader et. al [45]. Hereby k can be calculated by knowing the quality factor Q_f of the surrounding medium, which has to be $\gg 1$ (for cantilever oscillations in air), the width w , the length l and the resonant frequency ω_f of the cantilever by using the relation

$$k = 0.1906 \rho_f w^2 l Q_f \Gamma_i(\omega_f) \omega_f^2 \quad (3.11)$$

where k (N/m) is the spring constant, ω (1/s) the oscillation frequency, l (m) the cantilevers length, ρ_f (kg/m³) is the density of the fluid (air, liquid), Γ_i the imaginary component of the hydrodynamic function, which just depends on the Reynolds number $Re = \rho_f \omega w^2 / (4\eta)$ and ω_f the resonant frequency of the fundamental mode.

Another method which can be used if many different cantilevers with the same range of k are used in the experiment, is based on a reference cantilever whose k is already known. Thereby the CL with the unknown k is pressed on the reference cantilever and also on a very hard surface (e.g glass mica). Measuring the slopes of the repulsive regions of their force-distance curves makes it possible to calculate the unknown stiffness by using the relation $k = k_r (s_s/s_r - 1)$, whereas k (N/m) and k_r (N/m) are the stiffnesses of unknown

and the reference CL and s_s and s_r are the slopes from the measurements on the hard surface and on the reference CL [21]. There are some potential challenges according to this technique. First of all you need a very precise microscope with high magnification, to overlay the two cantilevers very properly. Furthermore, the technique makes it necessary not to just invest in the cantilevers, which are needed for the experiments, but also purchasing the reference cantilevers with spring constants similar to the unknown ones [11].

3.4 Indentation- type AFM

The previous chapters have already shown, that the AFM gives the opportunity to measure displacements and their corresponding forces simultaneously (force-displacement curves). This characteristic makes it possible to use the system for tensile-, indentation- or three point bending experiments which are commonly used to identify material characteristics like stiffness, elastic modulus or viscoelastic properties. The outstanding versatility of the AFM therefore promises it to be an ideal candidate for analysing biological materials with hierarchical structure and to separately investigate mechanical properties of single components of nanocomposite materials like tendon. In the following sections indentation type AFM (nano- and micro-indentation) should be described, as this type of experiment was the core of this thesis.

3.4.1 Nanoindentation

Nanoindentation is a widely used technique, to determine material characteristics on the nano-scale e.g. of thin films, cells and biological structural materials. AFM is well suited for soft material properties (e.g. red blood cells <1kPa - 50kPa; muscle cells 2kPa - 100kPa; cartilage 300kPa-2000kPa) . The indentation technique is historically based on a standard Brinell's hardness test, where specific well defined geometrical probes are pressed into a surface with a predefined force. Thereby, the post-indentation size of the residual imprint is measured by optical microscopy and gives information about the hardness and other material properties. At very small scales (micro and nanometre), these imprints cannot be determined any more, which led to the idea of measuring hardness and the elastic modulus directly, by analysing the continuous load vs. indentation data from the experiments [10]. The projected contact area A_c , which is nevertheless needed is extracted from a function, relating A_c to the

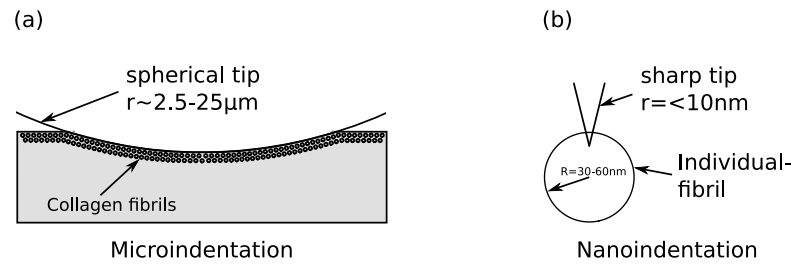


FIGURE 3.9: (a) Large tip radii are used to investigate larger areas of the sample (b) Tip radii with $< 10 \text{ nm}$ make it possible to investigate individual collagen fibrils with $d \approx 60-120 \text{ nm}$

indentation depth. In non-AFM nano-indenter experiments, most commonly three sided diamond pyramids, so called Berkovich tips, are used but there are also others like a the four-sided pyramidal Vickers or Knoop indenter. [30]. Instead for nanoindentation- type AFM Si or SiN_3 probes with a tip radius of $< 10 \text{ nm}$ are used.

3.4.2 Microindentation

In nanoindentation- type AFM a sharp tip with typical tip radius of $< 10 \text{ nm}$ is pressed into the sample of interest. In this thesis thereby A_c 's of $0.0005- 0.03 \mu\text{m}^2$ were reached which makes it possible to investigate collagen fibrils with diameters from 60 nm and upwards. In Microindentation on the other hand, much larger tip radii are used, typically ranging from $2.5- 25 \mu\text{m}$. Similar contact depths therefore lead to a much higher A_c ranging from $4- 36 \mu\text{m}^2$. This large differences in A_c make it possible to investigate much larger areas. In this thesis nano-indentation- type AFM was used, to analyse the mechanical properties of individual fibrils (see fig. 3.9 (b)), whereas microindentation was used for investigating larger tissue sections, consisting of several hundreds of fibrils 3.9 (a)). The latter makes it possible to analyse micro mechanical properties of tissue sections.

3.4.3 Analysis

A typical analysis approach for indentation experiments can be seen in fig. 3.10. In the first main steps the raw AFM data (Photodetector voltage vs. piezo Z-displacement) is converted into a force/ tip-sample separation (indentation)-curve by applying the sensitivity, k_c and the fact that the Z-piezo displacement is the sum of deflection and indentation, i.e. $Z = D + I$ (see fig. 3.11 (a)). The resulting force-indentation data can be analysed by two different commonly used

analysis procedures; the Hertz and the Oliver-Pharr method (see fig. 3.10). The Hertz method is based on the very early analytical investigations of Heinrich Hertz, who solved the problem of two deformable elastic spheres with different radii being in contact [20]. The main characteristic of this approach is assuming an ideal elastic deformation of the materials. Therefore the loading or the unloading part of the F vs. I curve is taken and fitted by the function of Hertz, whereas the elastic modulus is the fitting parameter. The Oliver-Pharr method on the other hand, allows also for inelastic, transient processes and material behaviour. That is why this approach in conventional nanoindentation is most commonly used and why it was also used in this thesis. This approach takes the most upper part of the unloading curve for the analysis, as this part should just represent elastic behaviour of the material.

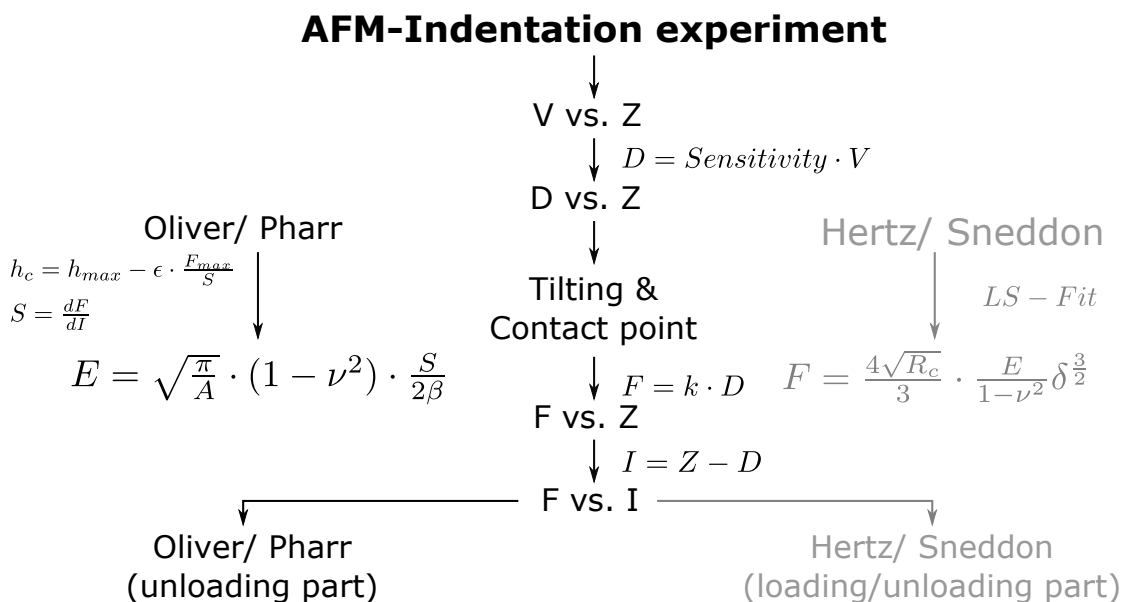


FIGURE 3.10: From the AFM indentation experiment you get the photo-detector voltage V vs. piezo Z -displacement Z data. This data is transformed into force F vs. Indentation I data by using the sensitivity, tilting and finding the contact point, and using a relationship between the indentation I , Z and the cantilever deflection D . In further steps the elastic modulus can be calculated by using the Hertz/ Sneddon (analysing the loading- part of the F vs. I data) or the Oliver & Pharr method (using the unloading part)

Oliver- Pharr method

Indentation experiments produce force vs. indentation data. The curve consists of a loading, optionally a holding and an unloading part (see fig. 3.11(c)). The Oliver - Pharr method mainly developed for analysing data from conventional

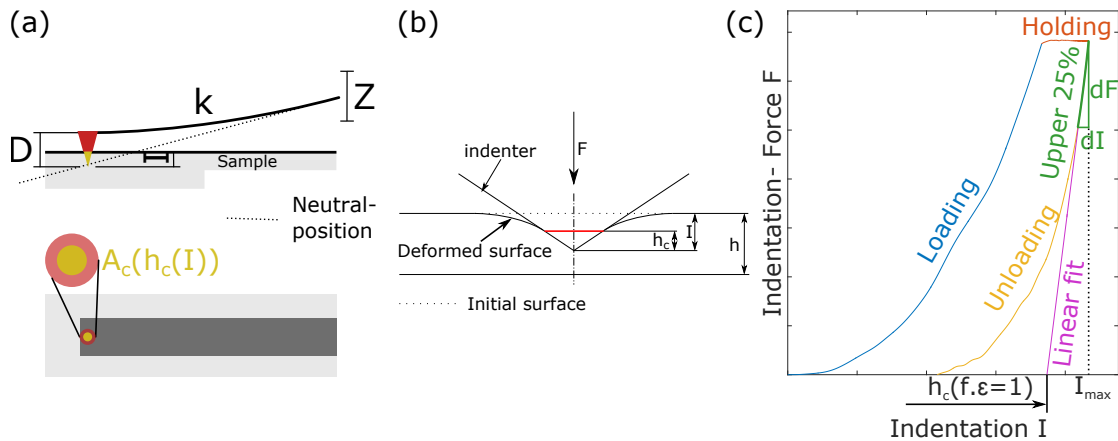


FIGURE 3.11: (a) AFM cantilever with tip during AFM- type indentation. The Z-piezo displacement (the overall vertical movement of the cantilever) is transformed into the deflection D and the indentation depth I . (b) A more detailed illustration of the inprint. The curvature of the deformed surface is far more curved than exactly following the indenter's shape. Therefore for calculating the contact area A_c the contact depth h_c has to be taken. (c) Typical force vs. indentation curve with holding the piezo in extended position for some time.

nano-indentation was first presented in 1992 [40] and improved over the years. This technique is not limited to sharp cantilever tips but can also be used for spherical (microindentation experiments) or other axisymmetric tips [39]. During indentation both, the sample and the indenter undergo mechanical stress and therefore deform. The reduced elastic modulus E_r of two elastic bodies in contact is described by [40]

$$\frac{1}{E_r} = \frac{(1 - \nu_i^2)}{E_i} + \frac{(1 - \nu^2)}{E} \quad (3.12)$$

with E_i and ν_i as the elastic modulus and the Poisson's ratio of the indenter and E and ν the same parameters for the sample. The purpose of this thesis was to establish a working protocol for measuring the elastic modulus of soft materials, such as hydrogels, and soft biological tissues as tendons, ligaments and cartilage. A pilot study in our laboratory indicated that the elastic modulus of such materials measured by AFM cantilevers-based indentation is the range of 0.5 kPa to 3 MPa. Because the elastic modulus of the indenters used in this thesis are in the range of 100 GPa (silicone nitride >100 GPa [22], borosilicate glass 64 GPa⁴) equation 3.12 essentially reduces to [64]

$$\frac{1}{E_r} = \frac{(1 - \nu^2)}{E} \quad (3.13)$$

⁴ <http://www.azom.com/article.aspx?ArticleID=4765> access on 10.01.2017

The sample stiffness is defined as the slope of the upper part of the unloading curve and linked to E_r by

$$S = \frac{dF}{dI} = \beta E_r \sqrt{A_c} \frac{2}{\sqrt{\pi}} \quad (3.14)$$

with dF/dI as the slope of the upper 25% of the unloading curve (see fig 3.11(c)). The true contact stiffness, S was corrected with a reference slope derived from pretests on the glass surface, that the sample was attached on. This was done by simple subtraction [1]. The correction factor β is a dimensionless parameter for taking into account deviations in stiffness, due to the lack of axial symmetry of the indenter. This parameter varies in a range of $1.0227 < \beta < 1.085$ and can be defined with a procedure shown in [39]. For the analysis in this thesis the parameter was set to 1. Substituting 3.14 in 3.13 leads to the final equation for the sample elastic modulus E

$$E = \frac{\sqrt{\pi}}{2\beta} (1 - \nu^2) \frac{S}{\sqrt{A_c}} \quad (3.15)$$

The problem that during indentation the surface is not exactly following the shape of the indenter, which leads to the fact that h_c is not equal to the indentation I , but has far more a curved shape (see fig. 3.11(b)), can be solved by taking the equation of [39] connecting h_c with the Stiffness S , the maximum indentation I , a correction factor ϵ and the maximum indentation force F_{max}

$$h_c = I - \epsilon \frac{F_{max}}{S} \quad (3.16)$$

The correction factor ϵ is a constant, which depends on the geometry of the indenter. Typical values are $\epsilon=0.72$, 0.75 and 1.00 for a conical punch, paraboloid of revolution (approximates also spheres of small depths) and flat punch in the same order. For the microindentation experiments, which were done with spherical indenters, ϵ was chosen to be 0.75 . For the nanoindentation experiments on the individual fibrils the indenter's shape was conical and therefore ϵ was 0.73 .

Determination of contact area A_c

The contact area A_c is defined as the cross-sectional area of the indenter being in real contact with the surface (red line in fig. 3.11(c)). Three standardised techniques are presented in ISO 14577-2 (specifies methods for verification and

calibration of testing machines for instrumented indentation tests) to determine A_c as a function of the contact depth h_c [47]:

- (1) Scanning the indenter and thereby determining the function using a traceable atomic force microscope
- (2) Indirect determination using a material with a known elastic modulus
- (3) Indirect determination by measuring the difference between the measured depth-dependent hardness and the depth-independent hardness of a reference material.

The most common technique used nowadays in conventional nanoindentation is (2) by taking a reference material with a well known elastic modulus used as E_r in Eq. 3.14 and solved for A_c :

$$A(h_c) = \frac{\pi}{4} \left(\frac{S(h_c)}{E_r} \right)^2 \quad (3.17)$$

Thereby several indentations with different contact depths are performed on the reference material and the stiffness is calculated from each indentation curve. The measured stiffnesses combined with the reference material (mostly fused silica with an $E_r = 69.6$ GPa [47]) makes it possible to calculate A_c for different contact depths. This point-by-point measurement can then be transformed into a function $A(h_c)$ by fitting a polynomial of the form:

$$A = C_0 h_c^2 + C_1 h_c + C_2 h_c^{1/2} + C_3 h_c^{1/4} + C_4 h_c^{1/8} + \dots + C_8 h_c^{1/128} \quad (3.18)$$

with C_{0-8} as empirical constants which make it possible to fit the data over a wide range of depths and therefore describe many different indenter shapes [39].

AFM indentation type experiments on soft materials like gels or biological tissues call for using cantilevers with stiffnesses in a range of 0.05- 7.4 N/m. Berkovich indenters commonly used in conventional indentation experiments are made of diamond with elastic moduli ranging from 800 GPa to 1200 GPa [17] which shows that this technique is not suitable for analysing the tip shape of AFM cantilevers. Alternative soft reference substances are not available for this purpose.

A different approach similar to the one described in ISO 14577-2 (2) was used in this thesis to produce the area function $A_c(h_c)$. It's based on the convolution effect already described in chapter 3. Scanning a surface with an AFM

always results in an image presenting a convolution of the surface topography and the shape of the tip (see fig. 3.5). Knowing the topography of the surface makes it possible to deconvolute the shape of the tip from the height data of the scanned surface. If the surface consists of very sharp edges or spikes and the tip radius is quite big in relation to the radii of the surface the produced image even represents the tip geometry at once. Such surfaces, commercially provided as "calibration gratings", are TGT1 or trench gratings and are commonly produced on Si wafers.

Determination of A_c using a TGT1 grating

TGT1 gratings consist of an array of very sharp tips with a tip radius of smaller than 10 nm. The structure of the TGT1 chip used in this thesis (NT-MDT Spectrum instruments) is presented in fig. 3.13. All of the tips, used in the micro- and nano indentation experiments, where scanning the TGT1-grating with the following procedure:

1. Approaching on the TGT1 surface
2. Producing an overview image by scanning an $10\ \mu\text{m} \times 10\ \mu\text{m}$ area with a solution of 512 pixels \times 512 pixels and a line rate of 1- 3 Hz (see fig. 3.12(a))
3. Selecting several spikes of the overview image and making a detailed image with a size of $1.5\ \mu\text{m} \times 1.5\ \mu\text{m}$, a solution of 512 pixels \times 512 pixels and a line rate of 0.5 Hz- 5 Hz (depending on if the tip is a sphere, then the linerate can commonly be higher or a very sharp tip as used in nanoin- dentation which calls for lower line rates)(see fig. 3.12 (b)).

It's very important to choose the lowest possible force for imaging to prevent both, the TGT1 spikes and the tip from damaging. To achieve that the contact force is decreased up to the point the trace and retrace lines in the real time oscilloscope of the JPK software are no more overlapping. If this happens the force should gently be increased again. In a second step the P- and the I-gain are increased as close as possible to the point oscillations in the trace or retrace lines appear. This parameters now should lead to the best possible image. For both of the tips having been used in the nano-indentation- and the micro in- dentation experiments, different approaches were chosen to analyse the TGT1 image data which is presented in the following sections.

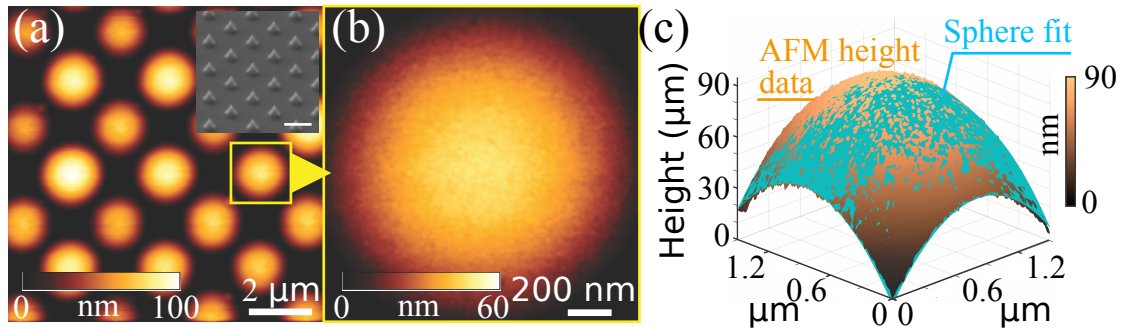


FIGURE 3.12: Figure shows procedure of the A_c determination with the TGT1 grating. This procedure is advisable for small spherical indenters used in microindentation experiments and sharp tips as used in nanoindentation experiments on single fibrils. (a) shows the overview image of $10\ \mu\text{m} \times 10\ \mu\text{m}$ as described in TGT1 procedure point 2. (b) shows detailed image of $1.5\ \mu\text{m} \times 1.5\ \mu\text{m}$ as described in TGT1 procedure point 3. (c) shows the data (orange) and the fitted sphere (blue) to determine the sphere diameter

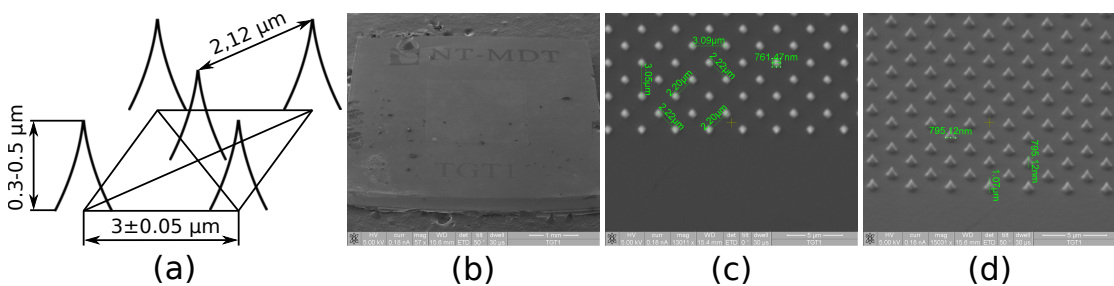


FIGURE 3.13: (a) Shows the nominal dimensions of the TGT1 grating having been used in the thesis (NT-MDT). The opening angle on the very tip end is $50^\circ \pm 10^\circ$. (b) Shows a 50° tilted SEM image of the whole TGT1 chip (size of the whole chip is $5\ \text{mm} \times 5\ \text{mm} \pm 0.5\ \text{mm}$) glued on a glass slide. (c) Shows a detailed SEM image of the top of the spikes. (d) Shows a 50° tilted SEM image of the spikes showing their conical sharp shape.

Sharp tips (Nanoindentation)

The analysis script written in MATLAB (version 2015b) to get the indenter's shape of very sharp tips as used in the nano indentation experiments was developed together with Orestis Andriotis, PhD. The script is build up in the following way:

- **Read image data:** The AFM image file consists of the following parts:
 - Thumbnail
 - Height (retrace)
 - Height measured (retrace)
 - Vertical deflection (retrace)
 - Lateral deflection (retrace)
 - Error-signal (retrace)
 - Height (trace)
 - Height measured (trace)
 - Vertical deflection (trace)
 - Lateral deflection (trace)
 - Error-signal (trace)

Each of these parts consists of the following tags: Filename, FileModDate, Filesize, format, format version , width, height, bit depth, color type, format signature, byte order, new sub file type, bits per sample, compression, photometric interpretation, strip offsets, samples per pixel, rows per strip, strip byte counts, x-resolution, y-resolution, resolution unit, colomap, planar configuration, tile width, tile length, teile offsets, tile byte counts, orientation, fill order, gray response unit, max sample value, min sample value, thresholding, offset, sample format and unknown tags. The matlab function "imfinfo()" was used, to save the information in a matlab structure, to use it in further analysis steps. In the following steps the tag "UnknownTags" is often used as it consists of important information (e.g. channel name, scansize etc.) which are characterize by specific IDs.

1. Identify the position of the "height-measured" channel by going through all channels and looking for the ID= 32851 in each tag "UnknownTags" of the image info.
2. The identified raw data is loaded with the MATLAB command `imread()`.
3. The scansizes of the image in x- direction (ID=32834) and y-direction (ID=32835) are read from the "UnknownTags" of the "height-measured" channel.
4. The multiplier (ID=33028) and the offset (ID=33029) are read from the "UnknownTags" of the "height-measured" channel.
5. The multiplier and the offset are transforming the raw image data (V) in a height image data (m) by using the formula

$$\text{Height (m)} = \text{Multiplier} \cdot \text{Rawdata (V)} + \text{Offset}$$

- **Linewise-planefitting:** Commonly images having been taken with the AFM can be slightly tilted, as perfectly plane clamping of the microscope slides on the motorized stage is fundamentally impossible and line to line variations can also occur due to the piezo actuator. For an accurate analysis of the tip it's necessary that the image is as plane as possible.
 1. Create a mask to identify the tip from the rest of the image by manually surrounding the region in the image which can be identified as the tip (light region) with a polygon (MATLAB function `roipoly()`) as shown in fig. 3.14 (a).
 2. The mask is converted and applied on the image data so that just the surrounding of the tip (the flat surface next to tip) is selected
 3. The height data of this selection is line-wise linearly least-square-fitted.
 4. The linear fits are subtracted line wise from the whole image data.
- **Deconvolution:** The deconvolution of the TGT1 image is done by simulating the TGT1 spike as a perfect cone with a fixed opening angle of 50° (as predicted by the manufacturer). The tipradius of the spike can be defined as input.

1. The scanning range of the image has to be given as input ($1.5 \mu\text{m} \times 1.5 \mu\text{m}$)
2. The suggested tip radius of the TGT1 spike has to be given as input ($<10 \text{ nm}$).
3. The cone with the given specifications is created in the center of the image.
4. The tip of the spike in the original data is identified as the maximum value of height. This position is needed to locate the tip of the simulated cone exactly on the maximum position of the image which has to be deconvoluted
5. The deconvolution is done by subtracting pixel wise the height of the cone from the original image. (see fig. 3.14(b)) [29], [1].

- **Projected area function $A_c(h_c)$**

1. The stepsize of h_c (nm), A_c should be created with, has to be predefined as input.
2. At each step A_c in pixels is calculated by using the MATLAB function `bwarea()`.
3. The area in pixels is transformed in m^2 using the size of the whole image and the total amount of pixels (see fig. 3.14 (c)).

Spherical tips (microindentation)

Microindentation as already described in chapter 3.4.2 was performed by using borosilica microspheres. Companies like "spi-supplies"⁵ provide such spheres with guaranteed diameters of $2.5 \pm 0.5 \mu\text{m}$, $5 \pm 0.5 \mu\text{m}$, $8 \pm 0.8 \mu\text{m}$, $10 \pm 1 \mu\text{m}$, $14.5 \pm 1 \mu\text{m}$ and $19.9 \pm 1.4 \mu\text{m}$ (quality checked by NIST traceable methods with optical microscope). In the micro-indentation experiments nominal diameters of $10 \mu\text{m}$ and $15 \mu\text{m}$ were used. The uncertainties given above can lead to errors in A_c of 10.3% and 7% for nominal diameters of $10 \mu\text{m}$ and $14.5 \mu\text{m}$ respectively, taking a mean contact height of $0.3 \mu\text{m}$ as it was typical in the experiments. Therefore analysing the diameter of the used spheres with a much

⁵ <http://www.2spi.com/search/microspheres/> (27.01.2017)

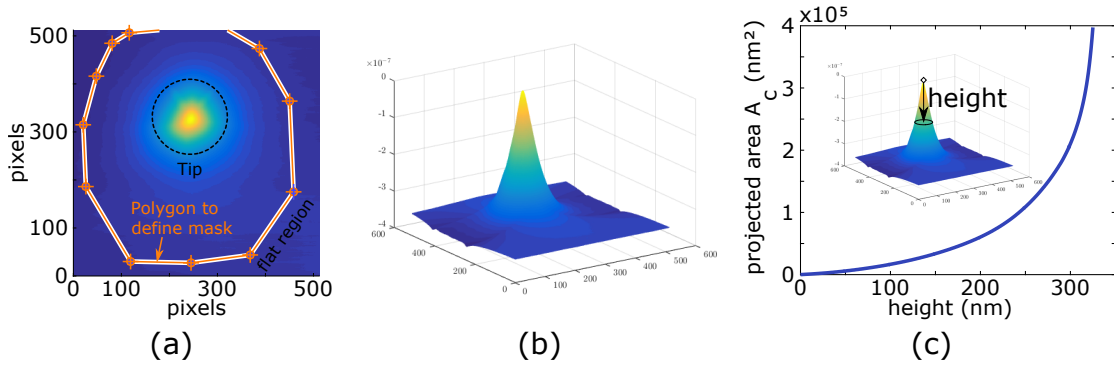


FIGURE 3.14: The fig. shows the procedure to get A_c from deconvoluting a height image of a TGT1 grating scanned with a sharp tip as used for the nanoindentation. (a) Shows the manual selection by the user of the region consisting of tip height data to separate it from the flat region which is needed for panefitting. (b) Shows an image of the deconvoluted height profile of the tip. (c) Shows the final function contact area A_c vs. height of the tip.

more precise method (AFM) than used by the manufacturer (light microscope) is advisable for this purpose a MATLAB (version 2015b) script was written aiming at determining the true diameter of the sphere. This diameter D_M is then used in the mathematical relation $A_c = \pi \cdot (D_M \cdot h_c - h_c^2)$ for calculating the contact area at a specific contact depth h_c to use it in equ. 3.15. This script consists of the following steps:

- **Read image data:** As described in sec. 3.4.3 (sharp tips- Nanoindentation).
- **Spherical least-square (LS) fit :** The height data is fitted by a spherical LS- fit⁶ as described in [25].

Analysing the real sphere diameter using TGT1 height data leads to some limitations according the size of the sphere. The smallest sphere radius which can be analysed is given by the envelope effect, which has to be avoided. This effect, already described in chapter 3, becomes existent when the sphere's angle α is smaller than the half of the opening angle β of the TGT1 spike (see fig. 3.15 (a)). Assuming the spike to be an ideal cone and the sphere being ideally spherical, leads to the following expression for D_{Mmin}

$$D_{Mmin} = \frac{2h_s}{1 - \sin\left(\frac{\alpha}{2}\right)} \quad (3.19)$$

⁶ The matlab script includes the code "Sphere Fit (least squared)" available on <http://www.mathworks.com/matlabcentral/fileexchange/34129> were used in the script.

with h_s as the height of the spike. To avoid getting an envelope effect, at any position of the TGT1 grating, $h_s = 0.5 \mu\text{m}$ and $\alpha = 60^\circ$ are the critical limit values, given by the manufacturer. Using them in equ. 3.19 leads to the smallest measurable sphere diameter without getting an envelope effect of $D_{Mmin} = 2 \mu\text{m}$. The smallest sphere diameter, to reach the bottom between the TGT1 spikes and therefore resulting in the most geometrical information of the sphere in the image can be expressed by

$$D_{Mhmin} = h_s + \frac{(p/2)^2}{h_s} \quad (3.20)$$

with h_s as the spike's height and p as the distance (period) between to neighbored spikes. Taking $h_s = 0.5 \mu\text{m}$, $p = 2.12 \mu\text{m}$ which is the most crucial case of any position on the TGT1, leads to an $D_{hmin} = 2.75 \mu\text{m}$. This case can occur if a TGT1 spike is imaged as presented by the blue square in fig. 3.15 (c) and not as it was commonly done in this thesis (presented by the red square), which also leads to a larger imaging height.

The theoretical maximum value of imaging height for a $15 \mu\text{m}$ sphere of $h = 152 \text{ nm}$ could also be observed when analysing an AFM image height profile along the imaging direction with a mean value of 147.58 nm (see fig. 3.16 (a)). Here just three arches of the profile were measured and it is likely the mean value of the measurements approximates the theoretical value much better if more height profiles are investigated.

For large spheres it's far more the lack of imaging height that makes the TGT1 grating not suitable. To reach the same span of height in the TGT1 image of the sphere as the indentation height ($0.3 \mu\text{m}$), which was common, the maximum sphere diameter would be $8 \mu\text{m}$. Nevertheless for small spheres this technique can definitely be used.

Determination of A_c using trench gratings

The quality of the spherical LS-fitting is mainly dependent on the amount and scattering of the data. During the glueing procedure it sometimes happens that the very bottom side of the sphere is slightly contaminated exactly in the range the TGT1 grating is imaging the sphere. Although these contaminations can mostly be eliminated by rinsing Ethanol gently over the sphere right after glueing, it sometimes happens that there are still some non spherical irregularities on the surface, which are not influencing the indentation experiment but can affect the spherical fitting. One way to overcome this problem is to gain

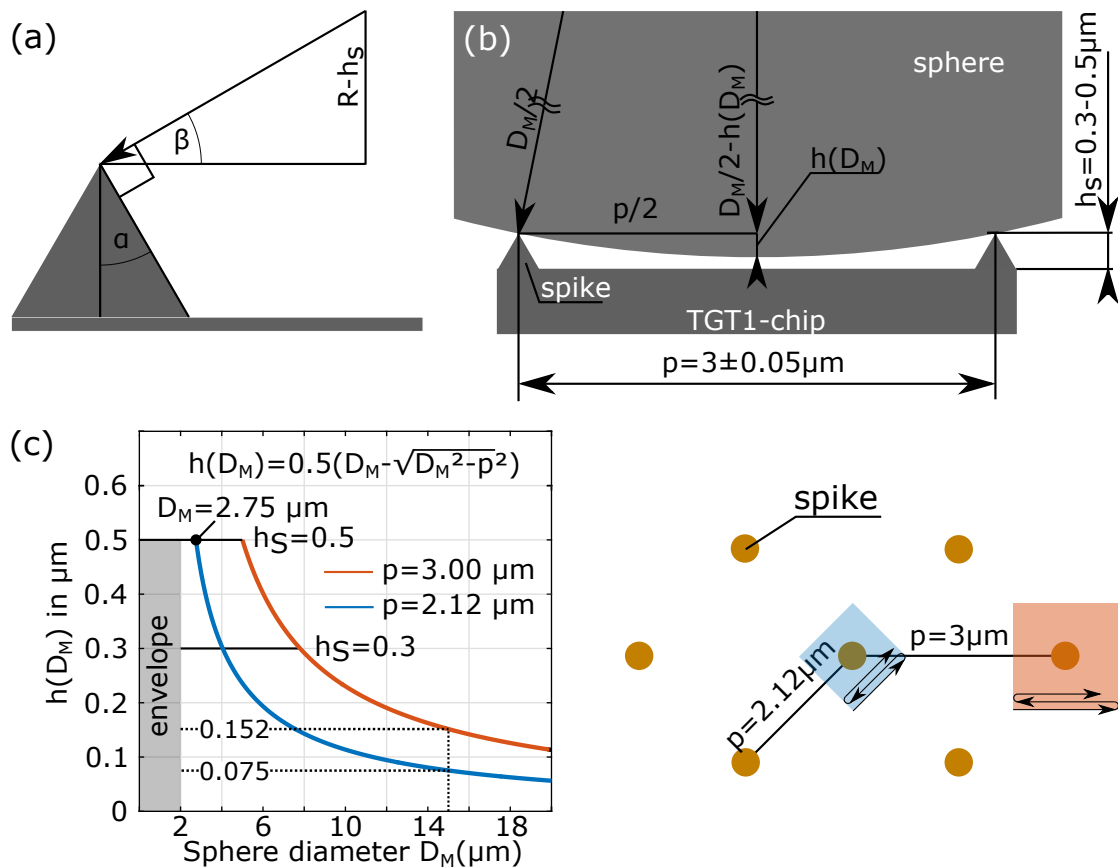


FIGURE 3.15: There are two main limitations according the sphere diameter determination procedure with a TGT1 grating. (a) Firstly spheres with a diameter less than $2 \mu\text{m}$ the envelope effect becomes dominant. (b) Secondly the distance in between the spikes of the TGT1 grating limits the imaging depth and therefore the amount of data of the sphere which is needed for the spherical LS- fitting. (c) Shows the maximum depth of imaged cap of the sphere for certain sphere diameters and imaging directions. Also the scanning direction influences the maximum height that can be scanned for a certain sphere diameter. Imaging a $15 \mu\text{m}$ sphere as shown with the red square leads to a maximum theoretical height of 152 nm whereas turning the direction by 45° reduces the maximum height to 75 nm (blue) due to the fact that the p is different in both cases.

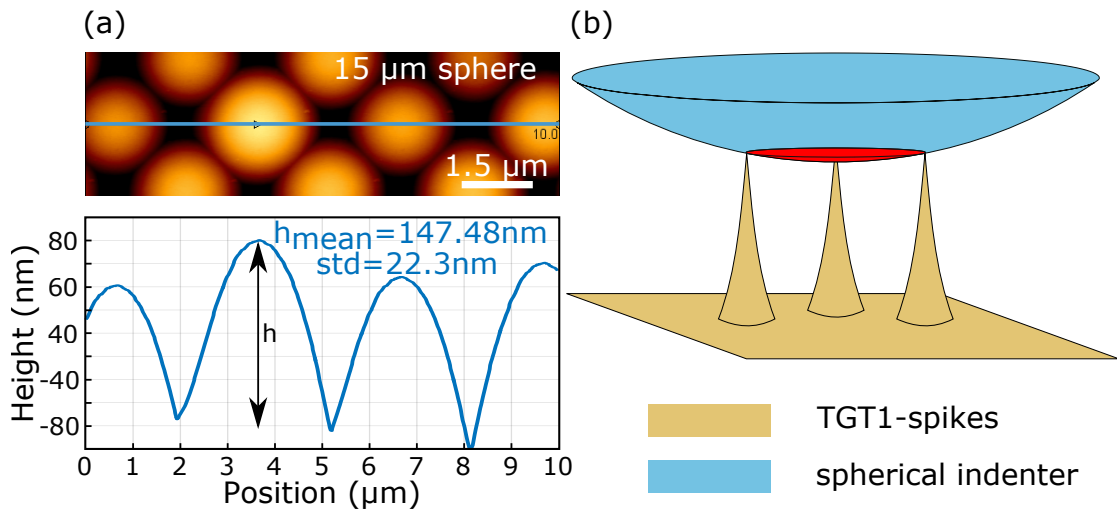


FIGURE 3.16: The height profile of one line of the overview image (d) proves the quality of the TGT1 grating as the measured mean height of the spherical cup of $h_{mean} = 147.48 \mu\text{m}$ corresponds to the theoretical value shown in (fig. 3.15(c)) of $147 \mu\text{m}$ for a sphere with $d = 15 \mu\text{m}$. (e) shows an illustration of the sphere scanning the TGT1 grating. The portion of the sphere being scanned is coloured in red.

more height data of the sphere. This implies use of a different type of grating. TGT1 gratings with higher spikes and a greater distance in between the spikes. However such gratings are not available commercially. Therefore a different approach to the TGT1 scanning was investigated in this thesis to determine the sphere diameter. Custom-made silicone trench gratings provided by David Grech (University of Southampton, UK), consisting of widths with $0.8 \mu\text{m}$, $0.9 \mu\text{m}$, $1 \mu\text{m}$, $2.5 \mu\text{m}$, $5 \mu\text{m}$, $10 \mu\text{m}$, $25 \mu\text{m}$ and $50 \mu\text{m}$ (see fig. 3.17 (a)) and a depth of $0.9 \mu\text{m}$ were used. This height leads to 6 and 4.5 times more information of a $10 \mu\text{m}$ and $15 \mu\text{m}$ sphere, respectively. Even if $4.5 \mu\text{m}$ spheres are measured on a position on the TGT1 grating characterised with spikes with a height of $0.5 \mu\text{m}$ the information obtained from trench grating would still be nearly twice. As the chip with the applied trenches was glued on a glass slide, always just one line of the sphere's profile was imaged. In the future this could be improved by fixing the chip in a way that it can be rotated after each imaging, which would make it possible to gain more information of the sphere shape.

All of the spherical tips were scanned using the $50 \mu\text{m}$ trenches by the following procedure:

1. Approaching in the flat region next to the trench
2. Producing an image of $5 \mu\text{m} \times 5 \mu\text{m}$ with a resolution of $256 \text{ pixels} \times 256 \text{ pixels}$ and a line rate of $0.5 \text{ Hz} - 3 \text{ Hz}$ (depending on the stability of the laser and the scan direction) in a way that half of the image is the flat

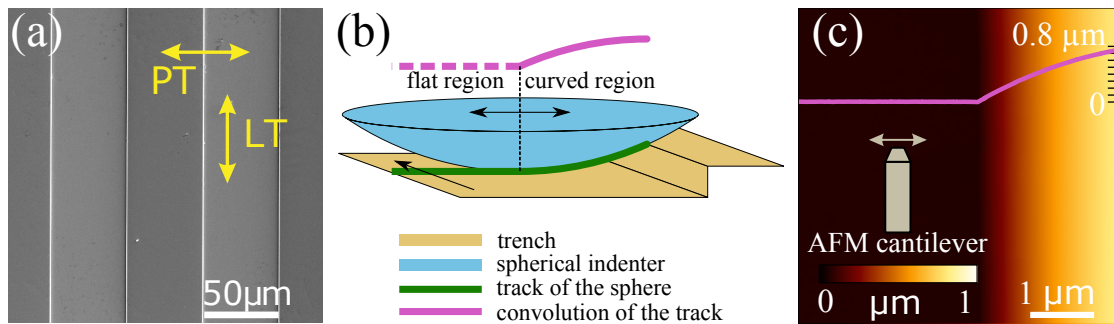


FIGURE 3.17: Shows the diameter determination procedure, using trench gratings. (a) Shows an SEM- image of the $50\ \mu\text{m}$ trenches (having been used) and the scanning direction (longitudinal/ LT-, and perpendicular/ PT direction). (b) Shows the scanning procedure in PT direction. When scanning the trench edge just one line of the spheres curvature is imaged multiple times (purple). (c) Shows an AFM image of the trench. The dark region is the flat region between the trenches which is needed as reference for line wise plane fitting. The purple line in (c) shows the actual height line profile of the sphere having been imaged at this position.

region next to the trench and half of it consists of curved height data of the sphere (see fig. 3.17 (c)) by scanning perpendicular to the trench direction (PT). Furthermore the image should be made so that the trench-axis is ideally vertically or horizontally aligned.

3. Scanning the same region by moving the cantilever in trench direction (LT)

The main difference between using TGT1- and trench gratings is that the data resulting from the trenches consist of just one curvature line of the sphere (see fig.3.17 (b)) whereas the images resulting from the TGT1 grating are a three dimensional image of the spherical cap.

The custom made MATLAB script (version 2015b) to analyse the trench height data is build up in the following way:

- **Input:** The user selects the *.jpg image file and is asked to give the scan direction ("in trench direction", "perpendicular to trench direction"), the image was produced in.
- **Read image data:** Same way as described in sec. 3.4.3 (sharp tips- Nano-indentation).
- **Line wise plane fitting:** The region consisting of the scanned edge is selected to differentiate it from the flat region next to the edge. The flat region data is then fitted line wise with a linear LS- fit and subtracted from each line of the whole image (see fig.3.18 (a)).

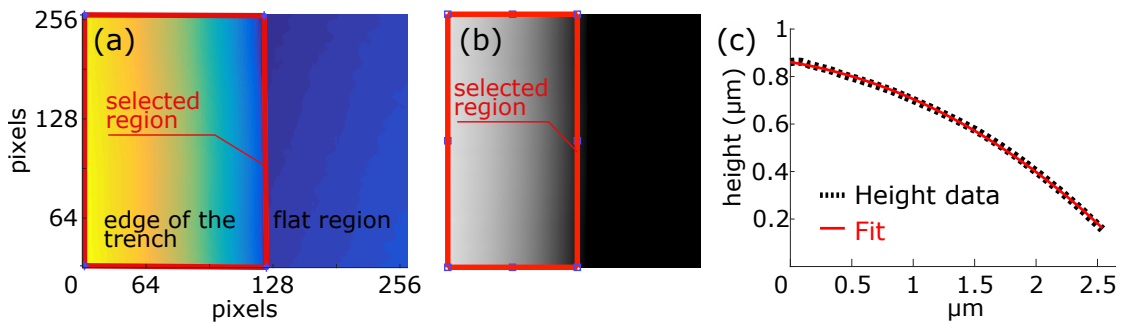


FIGURE 3.18: Shows the procedure used to analyse the trench height data. (a) The colour gradient of the flat region indicates the need of plane- fitting. Therefore the flat region is fitted line wise with linear LS- fits which are afterwards subtracted from the whole image data. Therefore the user has to manually select the region consisting of the sphere height data. (b) The region containing of curved height data of the sphere has to be selected in the image to crop it from the rest. This data is LS- fitted linewise by a circle. The mean value of the circle results lead to the sphere diameter (see also fig.3.17(c)). (c) Shows one line of the measured- height image data (black) and the corresponding LS- fitted circle (red).

- **Crop trench region:** The region consisting of the imaged trench- edge is cropped by manually creating a rectangular mask (see fig.3.18 (b)).
- **Line wise circle fit:** The cropped data is fitted line wise with a least-square circle fit⁷ (see fig.3.18 (c)).
- **Sphere diameter:** The diameter of the sphere is finally the mean value of the LS-circle fits of each line.

⁷ The circle fit was done using a MATLAB code by Richard Brown provided on <https://de.mathworks.com/matlabcentral/fileexchange/15060-fitcircle-m?requestedDomain=www.mathworks.com>

Chapter 4

Materials and Methods

4.1 Sample description

It was the aim of this thesis to determine the elastic properties of individual collagen fibrils and cryosections from the common digital extensor tendon (CDET) and the superficial digital flexor tendon (SDFT) from 3 years and 18 years old horses (see. table 4.1). The cryosections from each tendon type originated from longitudinal and transverse cuts and were provided by Chavaunne T. Thorpe and Hazel R.C. Screen (Institute of Bioengineering at the Queen Mary University of London) together with the macroscale tendon tissue, the individual fibrils were produced from. All of the samples were ethically sourced. As indentation type AFM and the derivation of material properties from such experiments are non standardised, calibration materials were also investigated. Here, agarose gels with different concentrations were tested on the AFM and a conventional mechanical testing machine. Additionally, experiments were performed using laser-cured Polyethylenglycol (PEG) and gelatine, which were differently crosslinked by varying the laser intensity. These samples were prepared by Peter Gruber and Katja Hölzl (Institute of Material Science and Technology at the TU Wien).

Tendon samples (QMUL)								Gel (TUW)		
CDET				SDFT				Agarose	PEG	Gelmod
3yr		18yr		3yr		18yr				
CSS	CFS	CSS	CFS	CSS	CFS	CSS	CFS			
LC	TC	LC	TC	LC	TC	LC	TC			

TABLE 4.1: Overview of samples having been tested (QMUL=Queen Mary University London, TUW=Technical University Vienna, CDET=common digital extensor tendon, SDFT=superficial distal flexor tendon, CSS=cryosection sample, CFS=collagen fibril sample, LC=longitudinal cut, TC=transverse cut)

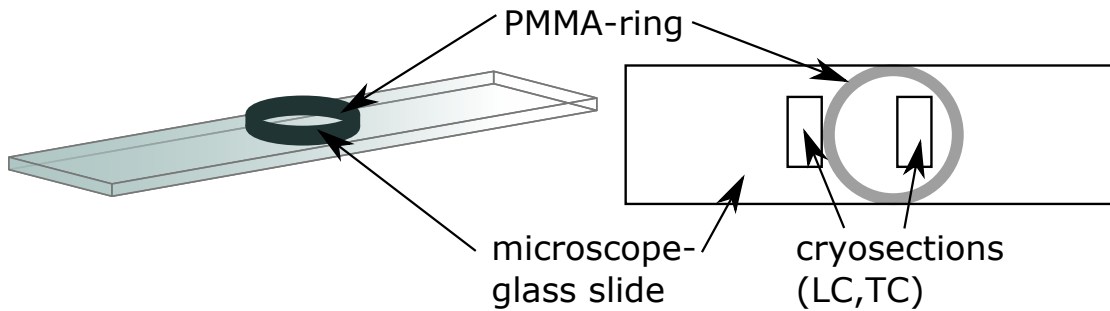


FIGURE 4.1: Two cryosections are located on each glass slide. For the microindentation experiments just one of them was investigated. The PMMA ring is glued on the glass slide, so that the sample of interest is slightly shifted from the center, which is necessary for measuring the reference slope on the glass next to the sample.

4.1.1 Tissue sections (micro-indentation)

The cryosections, located on microscope glass slides, were stored in a freezer at -80° up to the day of testing to prevent them from degradation. Each of these slides consisted of two sections located close to the middle of the glass slide (see fig. 4.1). One sample of each tendon (CDET and SDFT) and section type (longitudinal and transversal) was tested. The choice was made by optically analysing the sections using an inverse optical microscope (Axio Observer.D1, Zeiss) and identifying optically the one with best cutting quality and highest amount of IFM regions. Therefore in total eight cryosections were tested. Before the experiments were started, the samples were gently defrosted with distilled water avoiding damage by not pushing the water directly on the sample. Further on a PMMA (Polymethacrylate) ring with an outer diameter of 25 mm, an inner diameter of 21.5 mm and a height of 6.5 mm was glued on the glass slide with two parts silicone (picodent twinsil[®], mixed 1:1). The glueing was done by mixing the two parts of the silicon in a weighing tray (Rotilabo[®], PS, Item no. 1878.2, Carl Roth GmbH+Co. KG) with a stirring spatula (Item no. 4893.2, Carl Roth GmbH+Co. KG) until it was totally mixed. The edges of the fluid cell were gently dipped into the silicone to be slightly coated. The fluid cell was then placed on the glass slide, surrounding the cryosections in a way that their position was slightly shifted from the centre of the fluid cell (see fig.4.1). This was necessary to have enough space for measuring the reference slope on the glass next to the sample (see sec. 3.4.3). During the pre-analysing procedure with the microscope to find the best cryosection, both samples on the glass slide were kept hydrated, whereas during the micro indentation experiments just the one located in the fluid cell was kept in wet condition using Phosphatebuffered Saline (PBS) (pH 7.4).

4.1.2 Collagen fibrils (nano-indentation)

Up to this point the tendons were stored in a freezer at -80° to prevent them from degradation. For the preparation of individual collagen fibrils, sections with a thickness of about 5 mm were cut transversely from the SDFT and CDET tendons using a scalpel. The period of having the tendon tissue outside the freezer for the cutting procedure took 5-10 min so that it was still completely frozen when it was put back into the freezer. The harvested cross-sections were additionally surrounded with water soaked paper tissue and aluminium foil to keep them hydrated during defrosting. Afterwards they were directly put into plastic tissue culture dishes (BioLite 35 mm, Thermo Fischer Scientific, Prod. No 130180) filled with distilled water. By using sharp tweezers (DUMONT SWISSMADE, Item no. PK78.1, Carl Roth GmbH+Co. KG) collagen fibres were pulled out of the fascicular region of the cross section. A very small amount of the tissue was put on a poly-l-lysine coated glass slide (Thermo scientific). As long as the collagen fibres were wet they could easily be pulled over the glass slide held with tweezers. When they started to dry, the tissue began to smear on the glass and the collagen fibre package was uncoiled resulting in region consisting of several single collagen fibrils for nano-indentation analysis. If this uncoiling procedure did not work properly the sharp tweezers were also used to push fascicle tissue apart. Samples were stored in a freezer at -80° up to the day the experiments were done. To analyse the fibrils in wet and dry condition the fluid cell, which was also used in the micro-indentation experiments was placed and fixed in the same way as already described above (tissue sample shifted from the centre of the fluid cell)

4.1.3 Hydrogels

Polyethyleneglycol (PEG) and Gelatine

For the laser-cured PEG and gelatine gels, several geometries were examined to find the best one for fixation and testing in the AFM:

1. The gel was poured into silicon moulds with a diameter of ~ 4 mm and a height of ~ 1 mm, which were fixed on glass slides. Then the moulds were peeled off the glass and the gels were stored in conventional polycarbonate plastic laboratory bottles in a fridge at 4°C . The bottles were filled with distilled water to keep the samples hydrated. For the experiments, the gels were glued directly on a glass slide with dental silicone (prepared

as explained above) by putting a very small amount on the bottom side of the gels and pressing them slightly on the glass. During the experiments in wet condition most of the gels lifted off the glass after some time, which made this method inappropriate. Another problem of this method was, that the contact between the glass and the gel is not guaranteed as a homogeneous layer of silicone between the silicone and the gel was mostly not achieved. Additionally although the silicone is much stiffer than the gels, there is an uncertainty of what is measured (results are a mixture of silicone and gel properties).

2. The gels were poured into silicone moulds, which were placed onto a conventional glass cover-slip. The moulds were peeled off and the gels remained directly on the surface. After laser-curing the cover-slip was fixed on a glass slide by putting dental silicone on its edges. This technique assured that the gel had an ideal contact with the glass. But still during testing in wet conditions the gel lifted off which was noticeable by untypical indentation curves, showing that the cantilever was not properly approaching on the sample. This might be due to liquid getting under the gel in regions where it was slightly detached from the surface while peeling- off the silicone mould.
3. A gel droplet was directly poured onto a microscope slide resulting in spreading the gel over a bigger region. This procedure led to an ideal contact between the glass slide and the gel. Furthermore the gel did not lift off during measurements in liquid. The only issue might be that pouring gel on a surface leads to a curved surface on the crest of the gel, which should be prevented in indentation experiments. As long as the droplet is large enough i.e. the radius of curvature is much larger compared to the AFM tip radius this curvature is negligible.

Agarose

Agarose/ water -gels (powder low EEO, Sigma, product no. A9539) with 0.5 % w/v, 0.75 % w/v, 1 % w/v, 1.25 % w/v, 3.5 % w/v and 5 % w/v concentrations were prepared using the following procedure:

1. 100 ml de-mineralised and distilled water was poured into an Erlenmeyer flask.

2. The amount of agarose powder needed for the respective concentration was weighted using a scale (AX4202, Sartorius) and disposable weighing boats (VWR international).
3. The powder was gently put into the liquid while simultaneously swivelling the flask.
4. The mixture was heated using a conventional microwave (M515, Whirlpool). The flask was repetitively taken out of the the microwave and swivelled to guarantee proper and even dissolution of the agarose powder. This was done until the mixture appeared transparent.
5. Using a pipette (eppendorf Research[®] plus) 0.5 ml of the the warm gel was poured into three tissue culture dishes (BioLite 35mm, Thermo Fischer Scientific, Prod. No 130180).
6. The dishes were covered and stored in a fridge at 4°C.
7. The same agarose gels were also poured into Teflon moulds consisting of 5 holes with 8 mm in diameter and 9 mm in height. The bottom side and the top of the holes where covered with conventional glass cover slips to prevent the gel from leaking on the bottom and to get a very flat surface on the end faces of the cylindrical samples.
8. The samples were gently pushed out of the moulds using a plastic spatula.
9. The samples were stored in distilled water in a fridge at 4 °C.

4.2 Atomic force microscopy

The AFM was used for micro-indentation experiments on longitudinal, transversal tendon tissue sections and on hydrogels as well as for nano-indentation experiments on individual collagen fibrils. AFM was also used for imaging individual collagen fibrils in air and wet conditions to analyse their swelling behaviour and for imaging cantilevers for tip-shape characterization.

4.2.1 Microindentation

Ideal cantilever spring constant for force measurements

One challenging but very important part in indentation type AFM is the selection of the ideal cantilever stiffness, to reach ratio of the cantilever deflection D

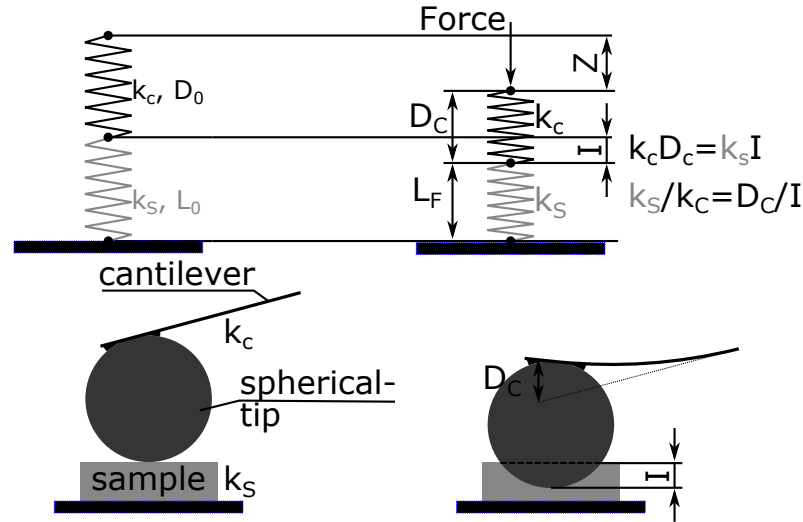


FIGURE 4.2: shows an AFM cantilever provided with a colloidal probe indenting the surface of a sample. This process can be simulated by a mechanical two spring model. When the cantilever is just getting in contact the cantilever (black spring) and the sample (grey spring) are not deformed. The Z-piezo moves towards the sample by a distance Z and pushes the colloidal tip against the sample and deforms the sample by $I = L_f - L_0$ and the cantilever by $D_C = D_f - D_0$.

and the piezo displacement Z also known as DZ-slope in a range of $0.2 < DZ\text{-slope} < 0.8$. This mainly comes from the state that the AFM sensitivity (not to be confused with the 'inverse of optical lever sensitivity' which was described in equation 3.2) is highest if the DZ-slope is 0.5, where the information of indentation is half coming from the cantilever deflection D and half from the extension Z , of the piezo, which is directly linked to the cantilever stiffness and the diameter of the spherical tip. This can be shown by modelling the contact of the cantilever and the material as two springs connected in series [64], whereas one represents the stiffness of the cantilever and one the stiffness of the sample (see fig. 4.2). While indenting into the material, the same force is acting on the cantilever and on the material, leading to a certain cantilever deflection D and deformation I of the sample. Therefore $F = k_c \cdot D = k_s \cdot I$ or $k_s / k_c = D / I$. As maximum AFM-sensitivity is reached when $k_s = k_c$ and the fact that the Z-displacement of the piezo is equal to the sum of the cantilever deflection and the indentation ($Z = D + I$) leads to $D / Z = 0.5$.

Due to variation of the materials mechanical characteristics, this theoretical ideal value cannot be reached on every single indentation point and therefore the acceptable range for the DZ slope was set to 0.5 ± 0.3 with the upper limit being more than the lower one. By filtering the data according this range ≈ 9.1 % of the whole microindentation data points were excluded whereas the data

of the longitudinal cuts changed by $\approx 19\%$ and data of the transversal cuts by $\approx 5\%$.

Tendon cryosections

The cryosections used in the micro-indentation experiments were longitudinal (LC) and transverse cuts (TC) of equine tendons with $\approx 10\ \mu\text{m}$ in height. The longitudinal sections made it possible to optically differentiate the fascicular (FM) and interfascicular matrix (IFM) and were therefore used to analyse these regions independently. The IFM was investigated by performing single indents on several representative positions (e.g. fig. 4.4 (a)) using the force-spectroscopy (FSP) mode (for JPK AFMs). The FM (e.g. fig. 4.4 (b)) was analysed by indenting nine times (squared pattern) in a region of $30\ \mu\text{m}$ by $30\ \mu\text{m}$ using FSP or force mapping (FMP) depending on the roughness of the sample. The FSP-mode is a function of the AFM to perform force distance measurements. Primarily made to investigate distinct single points it can also be used to define specific patterns the tip should indent over a certain region on the surface. In combination with the experimental planer a extended function of the AFM having been used in this thesis (JPK NanoWizard 3), makes it possible to also automatize movements of the motorized stage and therefore increasing the range of motion of the piezo actuators. This function makes it even possible to define any specific patterns and retract procedures on every point of indent, which makes it possible to also investigate rougher surfaces. The FSP-mode stores each of the indentation curves as single files in a predefined folder. The FMP-mode on the other hand is an extension of the simple FSP-mode which is made to investigate sample surfaces in a rectangular or squared pattern in a predefined region and a specific amount of pixels. In this mode each of the pixels represents a single force curve. The main difference of this mode compared to FSP is that the fact that surfaces of interest have to be flat enough as the cantilever is not able to retract as much as it's the case in the force spectroscopy mode in combination with the experimental planer. In this mode similar to the FSP-mode parameters can be predefined e.g. extend speed, extend and retract delay and maximum force. A big difference is the storage of the data. The FMP-mode saves the whole set of force curves and additionally predefined channels which are automatically calculated from the force curves (e.g. adhesion, slope, height data from the trace and retrace). A further extension of the FMP-mode is the QI-mode which was already described in chapter 3.

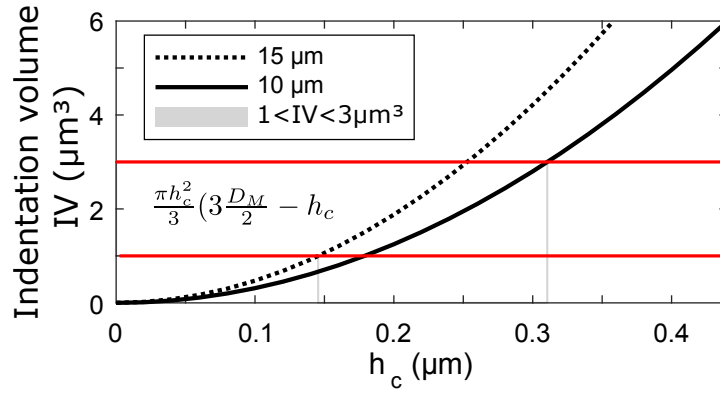


FIGURE 4.3: To reach the target interaction volume of $1 \mu\text{m}^3$ - $3\mu\text{m}^3$ a certain contact depth is needed depending on the micro-sphere diameter D_M having been used.

The transverse cuts (e.g. fig. 4.4 (c)) were used to characterise the tendon tissue in the natural stress direction (longitudinal direction) of the tendon. To make results more comparable it is advisable to aim for similar indentation depths, and interaction volumes when testing micro- and nanocomposite structures. Commonly the contact depth is tried to be in a certain range. In this thesis different diameters of the microspherical tips were used, which was necessary to increase the deflection of the stiff cantilevers used in the TC-samples. The contact volume for each experiment was controlled via the applied peak force with the aim to keep it between $1 \mu\text{m}^3$ - $3 \mu\text{m}^3$. As AFM experiments are always force (deflection) controlled, pretests on each sample were done, to find out which force was required (2.5 nN - 5 nN for IFM, 4 nN - 20 nN for FM, 140 nN - 350 nN for TC-samples) to reach a contact depth leading to the target interaction volume of $1 \mu\text{m}^3$ - $3\mu\text{m}^3$ for the used microsphere diameter (see fig. 4.3). Filtering the original microindentation data according to this range leads to an overall reduction of $\approx 46\%$ of data points whereas the longitudinal data reduce by $\approx 34.7\%$ and the transversal data points reduce by $\approx 52.8\%$. Applying also the filter according the DZ slope as described above leads to a reduction of the whole micro indentation data by $\approx 49.8\%$ whereas the longitudinal cut data reduces by $\approx 41.1\%$ and the transversal cut data points by $\approx 53.5\%$.

To reduce viscoelastic effects, the indenter was kept in extended position for 4s or 8s (holding time). Tipless cantilevers (High-Quality AFM probes CSC 38 with $k_{nom}(k_{true})= 0.03 \text{ N/m} (0.0423)$; $0.05 \text{ N/m} (0.0681)$ and CSC 37 with $k_{nom}= 0.3 \text{ N/m}$ and $k_{true}=0.1615 \text{ N/m}$; All-In-One, Budget Sensors with $k_{nom}= 7.4 \text{ N/m}$ and $k_{true}=7.5286 \text{ N/m}$ furnished with $10 \mu\text{m}$ or $15 \mu\text{m}$ glass spheres were used. The experiments were done in wet condition to reproduce a natural environment. Therefore PBS with a pH of 7.4 was used. A summary of the

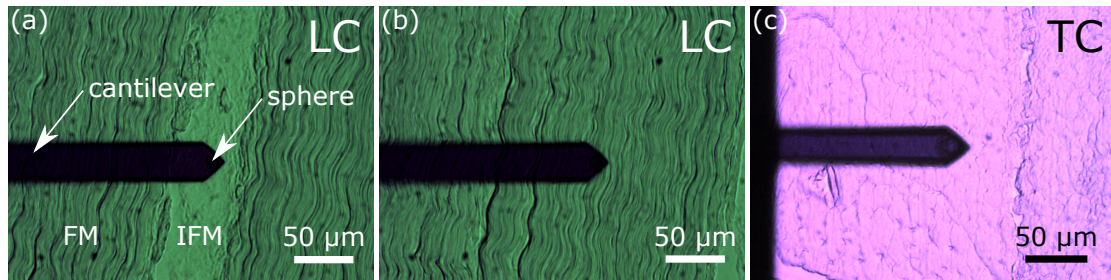


FIGURE 4.4: Shows typical samples and positions tested in micro-indentation experiments of a SDFT tendon from a 3 years old horse on longitudinal cryosections. (a) The FM is separated by the IFM which can be easily identified in the longitudinal cut samples. (b) Shows a typical position for testing the FM. Therefore nine indents were done in a region of $30\ \mu\text{m}$ by $30\ \mu\text{m}$. (c) Shows a typical position having been tested on a transverse cut sample. The FM and the IFM cannot be identified in the transverse cryosections. The reason for the different colour for the image (c) compared to (a) and (b) are different colour filter settings of the camera to make the identification of the structure easier.

whole experimental parameters is given in table 4.2.

sample	CDET young				CDET old				SDFT young				SDFT old					
	LC	IFM	FM/IFM	TC	LC	IFM	FM/IFM	TC	LC	IFM	FM	FM/IFM	TC	LC	IFM	FM	FM/IFM	TC
indents	17	16	103	74	18	17	74	74	15	17	15	72	72	14	10	14	10	33
indentation force (nN)	4	2.5	150	280	10	5	280	280	10	3	10	140	140	20	2.5	20	2.5	350
holding time (s)	4	4	4	4	4	4	4	4	4	4	4	4	4	8	8	8	8	4
cantilever	CSC38	CSC38	AIO	AIO	CSC38	CSC38	AIO	AIO	CSC38	CSC38	CSC37	AIO	AIO	CSC37	CSC37	CSC37	CSC37	AIO
cantilever spring constant (N/m)	0.042	0.042	7.53	7.53	0.068	0.068	7.53	7.53	0.042	0.042	0.042	7.53	7.53	0.16	0.16	0.16	7.53	
sphere diameter (μm)	10	10	15	15	10	10	15	15	10	10	10	15	15	15	15	15	15	15
mode	FSP	FSP	FMP	FMP	FSP	FSP	FMP	FMP	FSP	FSP	FSP	FMP	FMP	FSP	FSP	FSP	FSP	FSP

TABLE 4.2: Experimental parameters having been used in the micro-indentation experiments on tendon tissue samples (LC= longitudinal cut, TC= transverse cut, FM= fascicular matrix, IFM= interfascicular matrix, FSP= force- spectroscopy mode, FMP= forcemapping mode). For each of the longitudinal and transverse sample one cryosection was tested leading to 2 tested sample for each tendon type and therefore 8 samples in total.

concentration w/v (%)	0.5	0.75	1	1.25	3.5	5
samples	3	3	3	3	3	3
indentation force (nN)	5	5	5	5	500	400
holding time (s)	4	4	4	4	4	4
indentation speed ($\mu\text{m/s}$)	0.5	0.5	0.5	0.5	0.5	0.5
cantilever	CSC38	CSC38	CSC38	CSC38	AIO	AIO
cantilever spring constant (N/m)	0.0681	0.0632	0.0681	0.0632	7.895	7.553
sphere diameter (μm)	10	10	10	10	15	15
mode	FSP	FSP	FSP	FSP	FSP	FSP

TABLE 4.3: Experimental parameters for micro-indentation experiments on agarose samples (FSP= force- spectroscopy mode, FMP= forcemapping mode)

Agarose

On each agarose sample 9 indents were done in a range of 30 μm by 30 μm (squared pattern) using the FSP on three different positions over the sample with different indentation forces. To reduce viscoelastic effects a holding time of 4 s was chosen. Tipless cantilevers (High Quality AFM probes CSC38, Spmtips; All-In-One, Budget Sensors) furnished with glass spheres (diameters of 10 μm and 15 μm) were used. All of the experiments were done in liquid condition using distilled water. A summary of the parameters having been used in these experiments is shown in table 4.3.

PEG and gelatine

PEG and gelatine samples were used to study the dependency of mechanical properties of hydrogels according indentation force and holding time. This was needed to define proper parameters for the experiments on the tendon and agarose samples. Both sample types were cured with ultraviolet (UV) light to increase their initial amount of crosslinks leading to different mechanical properties. Whereas the PEG was exposed as a whole with UV light, a stripe structure was produced on the Gelmod sample by using different light intensities (40 mW, 60 mW, 80 mW and 100 mW). Using AFM type-microindentation the gels were repetitively investigated indenting in a 3 by 3 squared pattern in a range

of 30 μm by 30 μm . The indents were done changing the holding time step by step (0 s, 2 s, 4 s, 8 s, 16 s) using FSP. For each holding time also the indentation force was changed stepwise (2.5 nN, 5 nN, 10 nN, 20 nN). The experiments were done with a tipless cantilever (High Quality AFM probes CSC38, Spmtips; $k=0.1615\text{ N/m}$) provided with a 15 μm glass sphere.

4.2.2 Nanoindentation

At least six individual collagen fibrils were tested from one sample of each tendon type. To achieve this a force map over a length of 2.5 μm on the fibril consisting of 16 pixels in this direction was produced (see fig. 4.5 (d)). The width of the forcemap was chosen in a way that approximately one third of the whole map's width consisted of fibril data whereas at least 10 pixels were located on the fibril in this direction. The whole nano-indentation procedure was done in wet condition using PBS with a pH of 7.4. The experiments were done using Pyrex Nitride Probe - Diving Board cantilevers (PNP- DB, Nano World Innovative Technologies) (see fig. 3.3 (b)) and consisting of a pyramidal tip with a nominal spring constant of $k_{nom}=0.48\text{ N/m}$.

4.2.3 Imaging of individual collagen fibrils

Individual collagen fibrils were imaged with the AFM in dry and wet condition to analyse the swelling behaviour. For this the same cantilevers as in the nano-indentation experiments (PNP-DB) were used. The following procedure describes how the imaging was performed:

1. A promising position consisting of several individual collagen fibrils was identified using the inverted light microscope on the AFM (see fig. 4.5 (a)).
2. The position was imaged with AFM contact mode in a region of 20 μm by 20 μm with a resolution of 512 pixels by 512 pixels. It is important to use the lowest possible force to avoid damaging the fibrils (see fig. 4.5 (b)).
3. Assessment of the position as suitable if at least 6 individual fibrils are visible and can be measured separately. It is necessary that the fibrils are not too close to each other as the distances in between might change as fibrils swell, when adding PBS. If the position is rejected search for another one.

4. Imaging of at least 6 of the fibrils in contact mode in a range of 1.5 μm by 1.5 μm . The longitudinal axis of the fibril should be aligned as well as possible parallel to the long side of the image. This step also allows to check whether the fibril of interest is really one fibril or a strand of several fibrils. For this the typical D-banding of ≈ 67 nm can be used as an indicator (see fig. 4.5 (c)).
5. Retraction of the cantilever after imaging the fibrils in air, so that there is enough space to pour the PBS into the fluid cell using a pipette (eppendorf Research[®] plus). The PBS should be added very gently, not to move the sample on the glass slide. Furthermore the user should avoid pushing or touching the glass-slide. Otherwise the relative position between the cantilever and the imaged positions can change and making it very difficult to scan the same fibrils again in liquid.
6. Leaving the sample within the PBS for at least 30 min such that thermal equilibrium can be achieved. It can happen, that air bubbles appear on the sample. If that is the case, they can be removed by periodically aspirating and gently releasing PBS while keeping the pipette in the liquid.
7. Imaging the same position again in a range of 20 μm by 20 μm to ensure, that the fibrils have not moved due to the adding of PBS by using the quantitative- imaging mode (QI- mode, see chapter 3) in the JPK software. This mode is necessary as imaging contact mode would move the fibrils from their initial position.
8. As described in the previous section (Nanoindentation) a force map is applied on the same fibrils in the same region. This force map consists of an image including the height information of the fibril in wet condition (see fig. 4.5 (d)).

The swelling behaviour is quantified by the swelling ratio SR

$$SR(\%) = \frac{D_{PBS}}{D_{AIR}} \quad (4.1)$$

with D_{PBS} (nm) as the height of the fibril's crest in wet and with D_{AIR} (nm) as the height in air respectively. of a fibril was defined as the change in height of the crest of the fibril in dry and wet condition. The reason for measuring just the height of the crest and not its width is due to avoid the envelope effect (see section 3.2.1).

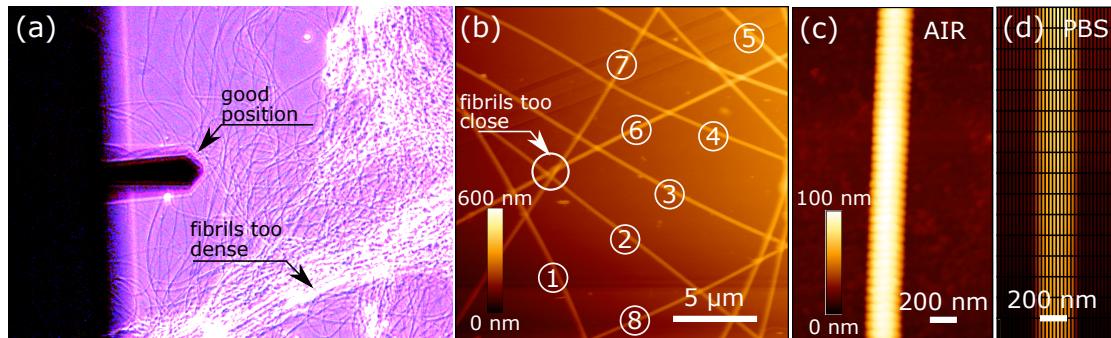


FIGURE 4.5: (a) Light- microscope image of a sample for nano- indentation experiments, consisting of several individual fibrils. (b) Overview image (AFM, contact mode) of 20 μm by 20 μm showing at least 8 appropriate positions to image and indent individual collagen fibrils in air and PBS respectively. (c) Single fibril imaged in air in a range of 2.5 μm by 1.5 μm . (d) The same fibril imaged in PBS. The raster shows the locations which were tested during force- mapping.

4.2.4 Microsphere glueing

Micro-indentation experiments were performed using custom-made spherical tips. Borosilicate glass micro-spheres (02715-AB; SPI Supplies, West Chester, PA) were glued on tippless cantilevers (CSC38 $k_{nom} = 0.03 \text{ N/m}$ & 0.05 N/m ; CSC37, $k_{nom} = 0.3 \text{ N/m}$ series, MIKROMASCH, USA and AIO, $k_{nom} = 0.3 \text{ N/m}$, BudgetSensors) by the following procedure:

1. The AFM cantilever is mounted on the AFM holder
2. The optical lever sensitivity is determined by performing at least 10 deflection (Volts)- Z displacement (nm) curves in contact mode on a freshly cleaved mica surface. The inverse upper slope of each curve is calculated. The average of the values is the inverse optical lever sensitivity.
3. The spring constant is determined by using the thermal noise method (implemented in the JPK software).
4. The glass spheres are prepared on a glass slide by diluting 1 mg of glass micro-spheres in 10 ml of ethanol. The glass spheres should be dispersed by spinning the solution using a vortex. 50 μl of the solution are resided on the glass slide using a pipette. While the glass slide is under the microscope the ethanol evaporates. If the glass spheres are densely packed they can be spread by residing about 50 μl of ethanol on the glass slide with the spheres.
5. A location is searched consisting at least of one separate sphere (see fig. 4.6 (a)).

6. The cantilever is approached next to the sphere on the glass slide and the position of the Z stepper motors is set to zero. Then the cantilever is retracted by twice the nominal diameter of the spheres e.g 30 μm for a 15 μm sphere diameter.
7. To visualise the sphere when the cantilever is positioned over it, the DIC filter is used.
8. The cantilever is retracted up to about 100 μm .
9. The AFM head is removed from the stage and about 2 ml epoxy (90 min hardening epoxy, UHU[®] PlusENDFEST) is prepared by mixing about 1 ml from each part thoroughly with a spatula.
10. Using a very sharp specimen (e.g. an hair of a hair brow) a very small droplet of epoxy is put close to the sphere of interest.
11. The AFM stage is moved to the right side to locate the droplet on the right border of the circular field of view of the inverted optical microscope (see fig. 4.6 (b)).
12. The AFM head is placed on the stage.
13. The edge of the cantilever is approached onto the border of the epoxy droplet. When the cantilever touches the surfaces of the epoxy it should be quickly retracted about 10 μm (see fig. 4.6 (c)).
14. The amount of epoxy is minimised on the cantilever by approaching several times on the glass slide next to the sphere of interest (see fig. 4.6 (d)).
15. The cantilever is approached on the sphere so that the sphere is centred on the longitudinal axis of the cantilever. In this position the cantilever is kept to let the epoxy dry at least for an hour (see fig. 4.6 (e)). Then the cantilever can be taken out of the cantilever-holder. To ensure that the epoxy is completely hardened the cantilever should ideally not be used for another 24 hours.

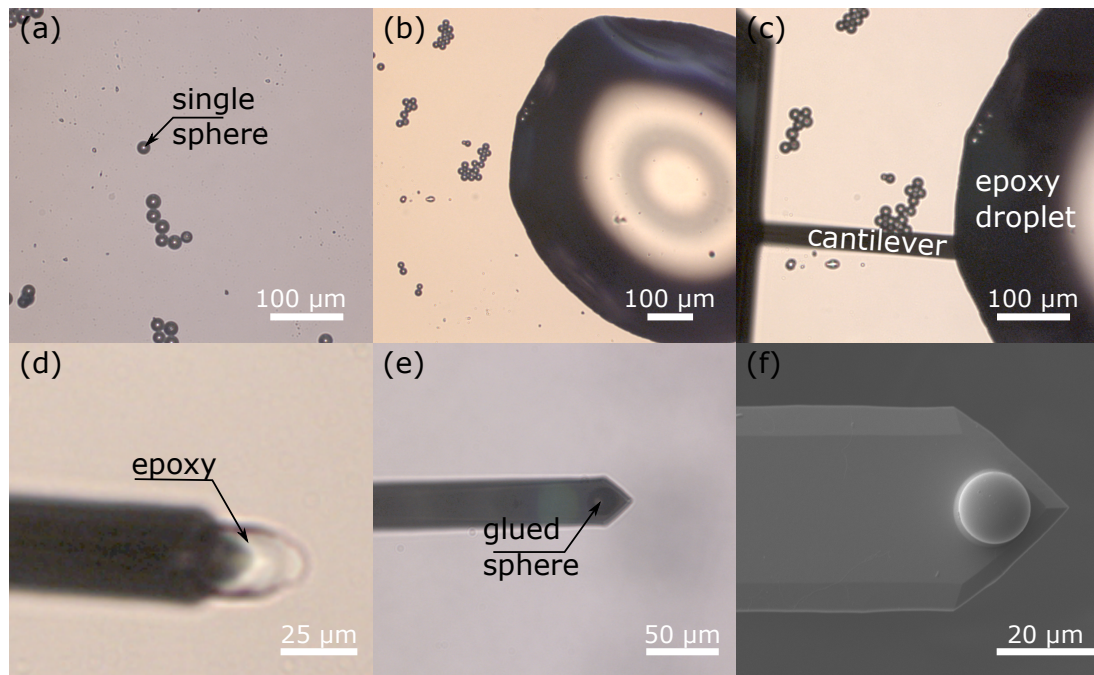


FIGURE 4.6: Shows the main steps for glueing micro spheres on a tip-less cantilever. (a) Location consisting of at least one separate sphere. (b) Positioning a droplet of epoxy on the glass slide. (c) Picking up some epoxy on the very end of the cantilever. (d) Minimizing the amount of epoxy by approaching on the glass slide next to the sphere of interest. (e) Approaching on the sphere to glue it. (f) SEM image of a glued sphere.

4.3 Macroscale compression tests

For cross-comparison, the agarose having been tested in micro-indentation experiments, was also analysed in uniaxial compression tests. In these experiments I was assisted and supported by knowledge about the system, by Martin Frank (Institute of Lightweight and Structural Biomechanics at the TU Wien). Therefore a conventional servo-electric miniature load frame (SEL-mini001, THELKIN AG) employed with a 10 N load cell (HBM S2M) was used. The cylindrical agarose samples were positioned in between the bottom of a custom made fluid-cell (filled with DI-H₂O) and a conventional microscope glass slide which was directly fixed to the load cell. The regions the sample was in contact with the fluid-cell and the glass slide were provided with teflon stripes to minimize friction between the sample and the surface and therefore providing uniaxial stress in the sample (see fig.4.7 (a, b)).

The mechanical tests were performed displacement control with a maximum displacement of 0.9 mm, which corresponds to a strain of the sample of 10 %. Each sample was tested with a compression speed of 0.3 mm/ min and 0.1 mm/ min. In between experiments the samples were left in DI-H₂O

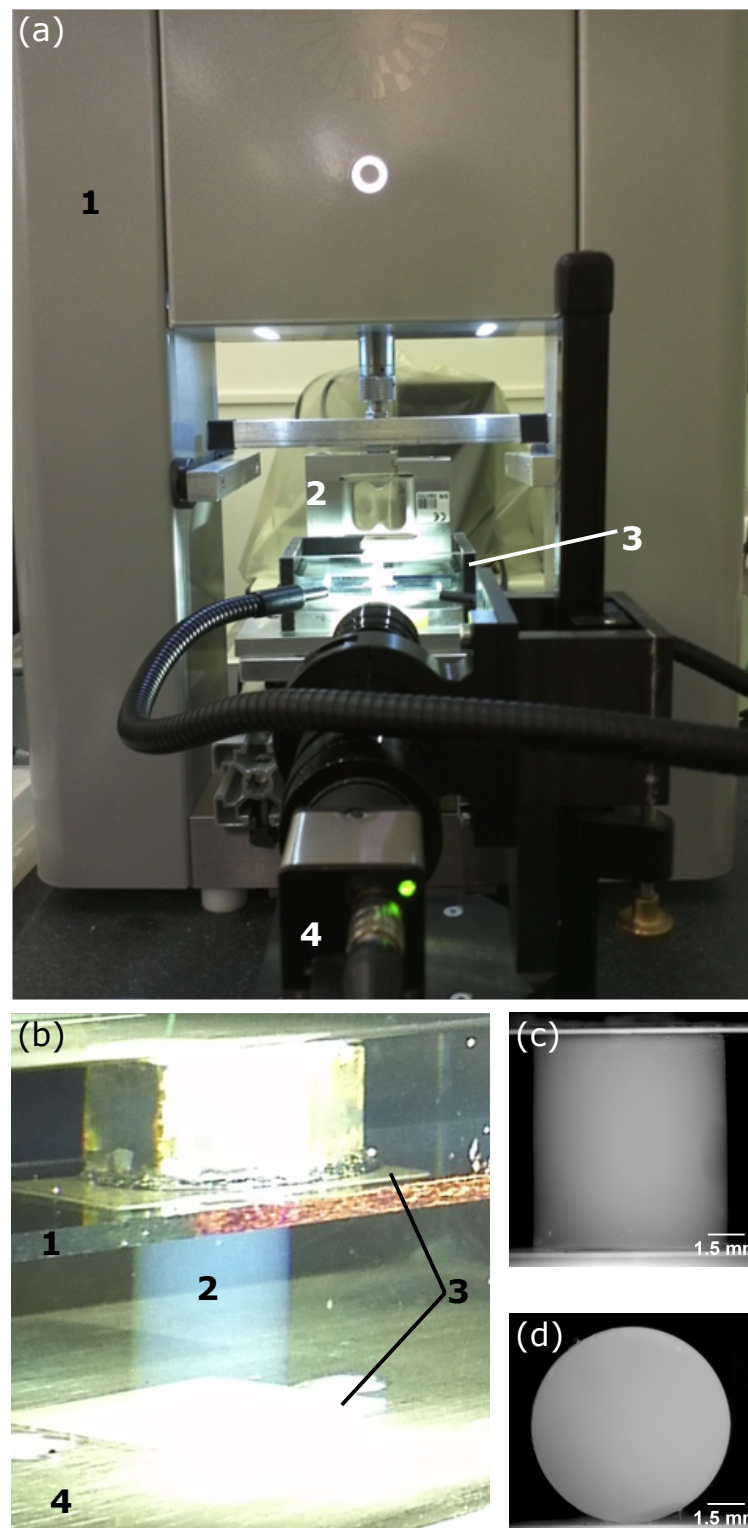


FIGURE 4.7: Procedure of macroscale compression experiments on agarose. (a) experimental setup (1= Thelkin miniature load frame, 2= load cell, 3= fluid cell). (b) Agarose sample (2) located between microscope glass slide (1) and bottom of fluid cell (4). Teflon stripes guarantee uniaxial compression. (c) Frontview of the cylindrical agarose sample to define initial height. (d) Topview of the sample to define the diameter. (e) Stress-strain curves for different agarose concentrations (0.5%, 0.75% and 1%). (f) Slope of the stress- strain curve in a strain range from 1%- 2% defines the compression modulus

concentration w/v (%)	0.5	0.75	1	1.25	3.5	5
samples	3	4	3	6	5	6
strain rate (1/min)	0.01/ 0.03	0.01/ 0.03	0.01/ 0.03	0.01/ 0.03	0.01/ 0.03	0.01/ 0.03

TABLE 4.4: Experimental parameters on of macroscale compression experiments on agarose gels.

for at least 5 min to let them recover completely. To achieve a flat contact between the gel-fixating glass on the top, 0.03-0.05 N preload was applied. The displacement data was taken from the internal measurements system of the load frame. The accuracy of this system was verified by independently measuring the displacement of the microscope glass slide using a video capturing system (UI-3250CP-M-GL) at 5 Hz frame rate. These data was then analysed using the Messphysik Videoextensometer ME46 software (MESSPHYSIK MATERIALS TESTING GmbH) and compared to the internal system displacement data. The system was also used to identify the initial geometry (height, diameter) of the agarose samples by taking images of the bottom, the top and the side of the sample, which was necessary to calculate the axial strain and stress of the sample. Using "imageJ" the circular peripheries of the top and the bottom of the cylindrical samples were manually fitted with circles. The initial cross-sectional area was calculated by assuming it to be ideal circular and using the mean of the fitted circle diameters of the top and the bottom of the sample (see fig. 4.7 (c, d)).

4.3.1 SEM imaging of microspheres

All of the microspherical tips used in the microindentation experiments were imaged before performing the experiments, using TGT1- and trench gratings as described in sec. 3.4.3. Also the trenches and the TGT1 grating was additionally imaged. The tips which didn't get lost due to unforeseeable events (e.g. breaking of the cantilever), were also obtained afterwards with a Scanning Electron Microscope (SEM) of the Quanta 200 3D DualBeam System (FEI, Hillboro, oregon, USA), which incorporates a motorized stage with a tilt range of 60°. This imaging was highly supported with knowledge about the principle of SEM imaging by Vedran Nedelkovski (Institute of Lightweight and Structural Biomechanics at the TU Wien). Prior to SEM imaging, the cantilevers were sputter coated with a 5 nm gold-palladium layer in the Q150T S High Resolution

Sputter Coater (Quorum Technologies Ltd, East Sussex, United Kingdom) to reduce negative charging effects, which cause loss of resolution or astigmatism. Subsequently, the cantilevers were fixed on a conventional SEM stub holder with a carbon tape and mounted in the vacuum chamber of the SEM. Imaging was performed in the secondary electron mode, at a working distance of 15.2 mm, using acceleration voltages of 5 kV and 10 kV and currents of 0.12 nA, 0.18 nA and 0.23 nA. The trenches were obtained using an acceleration voltage of 10 kV and a current of 0.23 nA whereas the TGT1 grating was investigated using an acceleration voltage of 10 kV and a current of 0.18 nA. Length measurements were performed with the calibrated software of the instrument.

4.3.2 Statistical analysis

Statistical differences between tendon types or age groups were determined using predefined functions in Matlab (R2015b). The original and also transformed data (logarithmus, square root, reziproke) data was tested for equality of variance using the Levene test (implemented in Matlab function `vartestn()`). The data set with the highest similarity in variance (original or specific transformed one indicated by the highest Levene's test p-value e.g see table 5.5) was tested using analysis of variance (ANOVA) (implemented in Matlab function `anovan()` with $\alpha = 0.05$). The null-hypothesis whether the PBS-diameter data comes from continuous distributions with equal medians was tested by using a non-parametric Wilcoxon rank sum test, with the hypothesis being accepted for $p > 0.05$.

Chapter 5

Results and Discussion

5.1 Microsphere diameter evaluation

Results from imaging micro-spherical tips ($d_{nom} = 10 \mu\text{m}$ and $15 \mu\text{m}$) with the AFM (TGT1; trenches: LT,PT) compared to the SEM, show no statistically significant differences ($p_{10\mu\text{m}} = 0.81$, $p_{15\mu\text{m}} = 0.29$) in measured diameters. For $10 \mu\text{m}$ spheres the coefficient of variance (CoV) showed comparable results between the TGT1 (16%) and the SEM (14%) method. The other methods showed much higher CoVs (LT= 45%; PT= 52.4%). For the $15 \mu\text{m}$ nominal diameter spheres, both trench- imaging methods showed comparable results (LT= 6.5%; PT= 16.2%) to the SEM (8.3%). For this diameter the TGT1 showed a higher CoV (32%). A summary of the mean diameter values and their standard deviations is shown in table 5.1.

The aim, for investigating different imaging techniques and testing gratings, was to find an alternative, for analysing micro-sphere diameters with SEM, which is often used to estimate geometries on the micro-scale. Since an SEM might not always be available, alternative AFM-based methods are of interest. Also, using the AFM directly is quicker compared to SEM imaging. Using diameter data of the microspheres for analysis given by the manufacturer might also be a choice but not advisable, as this data is often given with high tolerance ranges of around 10%, which also increase the overall error of the results.

methode	SEM	TGT1	LT	PT
d_{mean} (SD) (μm); $d_{nom} = 10 \mu\text{m}$	10.65 (1.5)	10.46 (1.69)	12.92 (5.81)	11.25 (5.89)
d_{mean} (SD) (μm); $d_{nom} = 15 \mu\text{m}$	14.02 (1.17)	12.21 (3.9)	13.73 (0.89)	15.14 (2.23)

TABLE 5.1: Diameter results from different imaging methods and micro-spheres ($10 \mu\text{m}$, $15 \mu\text{m}$): SEM (scanning electron microscope), AFM (atomic force microscope) with different test gratings (TGT1, trenches); LT= imaging in longitudinal trench direction, PT= imaging perpendicular to longitudinal trench direction.

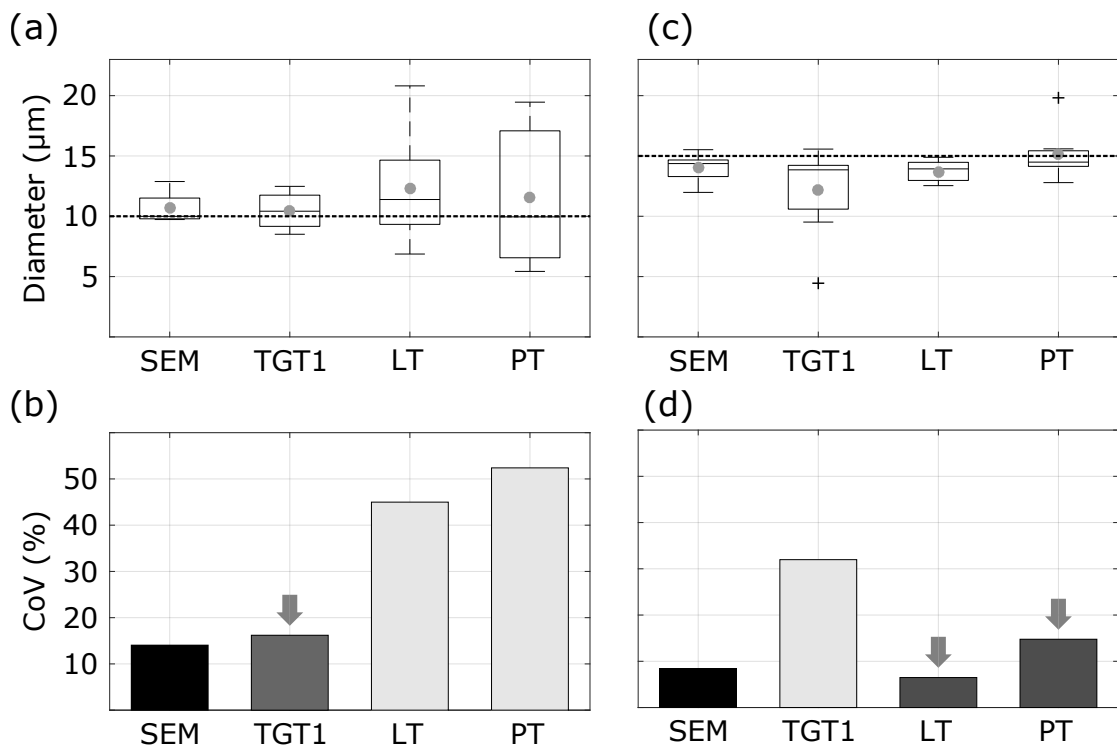


FIGURE 5.1: Results from diameter estimation of the microspherical tips using different methods: SEM (scanning electron microscope and AFM using different gratings (TGT1, trenches). The trench grating was imaged longitudinal (LT) and perpendicular (PT) to the longitudinal trench-axis. Boxplots for the diameter results for 10 μm (a) and 15 μm (c) imaged with the different methods with their median (solid lines) and mean (filled circle) values. (b,d) Shows the corresponding coefficients of variance (CoVs) for the certain method and diameter.

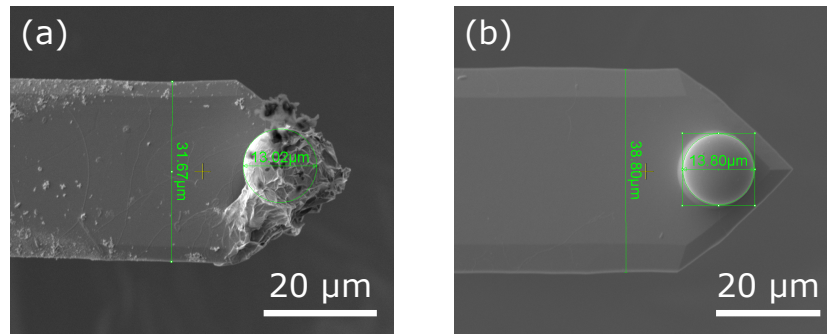


FIGURE 5.2: Shows an SEM image of an unused cantilever (a) and one which is contaminated with agarose gel, which was picked up during indentation experiments. Such contamination makes it difficult to clearly define the spheres periphery and to get the diameter.

Furthermore SEM imaging also implies the danger of damaging the cantilever during preparation procedures (e.g coating which is necessary to reduce negative charging effects which causes loss of resolution or astigmatism). In this thesis the cantilevers provided with the spherical probes, were SEM imaged after having done the microindentation experiments, as it was unclear whether coating influences the mechanical properties or not. This lead to two main problems. Due to unforeseeable events some of the cantilevers broke and so also the microspheres were no more available for being analysed in the SEM.

The other problem was contamination of the tips during the indentation experiments, which made it difficult to clearly identify the periphery of those spheres to precisely measure their diameter (see fig. 5.2). These events could be averted if experiments existed, showing that preparations needed in SEM imaging e.g. coating, do not influence the cantilevers mechanical characteristics (spring constant) or indentation results. Then SEM imaging could also be performed, together with the AFM imaging, before performing indentation experiments. In this case the risk of loosing geometrical information about the sphere, if the cantilever breaks, could be averted and a larger amount of data would be available. Further this, experiments focusing on the comparison of the spring constant before and after SEM coating would gain helpful knowledge. Producing test gratings similar to the TGT1, with higher spikes and larger periods (distances in between the spike) might also improve results. Then it would be possible, to create a similar function, which precisely describes the contact area for specific indentation depths, as it was used in the nanoindentation experiments (see fig. 3.14). The results show that it is possible to use AFM techniques for micro-sphere diameter estimation. For small spheres $>3 \mu\text{m}$ (theoretical limit see chapter. 3 and proven by the results) using the TGT1

grating leads to similar results as in SEM imaging. For larger spheres (i.e 15 μm) using trenches leads to better results, which might be due to the larger portion of the sphere being imaged, improving the LS-fitting. As the amount of data was quite scarce from these experiments (10 μm = 4; 15 μm = 7) it would be good to keep on gathering geometrical data of the microspherical tips, using all of the three imaging techniques (AFM-trench- and TGT1 imaging and SEM imaging), making it possible to further prove the efficiency of AFM-based tip imaging techniques.

5.2 Validation experiments on Agarose

The reason for doing experiments on agarose gels, was to validate, that AFM is able to identify differences of mechanical characteristics from "homogeneous" materials on the micro-scale level. The AFM results were compared with standard compressions tests on the macro-scale level. This knowledge is necessary, to validate the results from AFM-type microindention experiments from the horse tendon. Ratios of the mean values of the AFM- and the compression test results (E_{AFM}/E_{Macro}) are shown in fig. 5.3, fig. 5.4. A summarize of the elastic modulus of the compression tests and the ones from the AFM experiments is given in table 5.2. Typical stress-strain curves from the standard compression experiments and an enlargement of the region, the slope, which was used to calculate the elastic modulus is taken from, (1-2% strain) are shown in fig. 5.7.

Compression tests were done in displacement control with speeds of = 0.01 mm/min, 0.3 mm/min, leading to strain rates of 0.01 min^{-1} and 0.03 min^{-1} respectively. Previous studies on gellan gels showed no influence on mechanical

Agarose concentration (%w/v)	0.5	0.75	1	1.25	3.5	5
E_{Comp} (SD) in kPa strain rate = 0.01 1/min	5.1 (1.5)	9.4 (0.4)	27.4 (9.2)	45.1 (2.7)	424.7 (22.3)	562.3 (205.6)
E_{Comp} (SD) in kPa strain rate = 0.03 1/min	7.9 (0.9)	13.7 (1.4)	38.6 (6.9)	58 (3.5)	517.3 (18.7)	603.8 (289.8)
$E_{AFM}(SD) \text{ in kPa}$	5.7 (1.7)	6.2 (1.8)	24.5 (9.4)	23.8 (2.4)	513 (82.9)	764.6 (111.7)
$n_{0.01 \text{ min}^{-1}}$	2	4	3	6	5	6
$n_{0.03 \text{ min}^{-1}}$	3	4	4	6	5	6
n_{AFM}	3	3	3	3	3	3

TABLE 5.2: Shows results from the Agarose validation process. In the compression tests (Comp) two different compression speeds were investigated (0.1 mm/s, 0.3 mm/s).

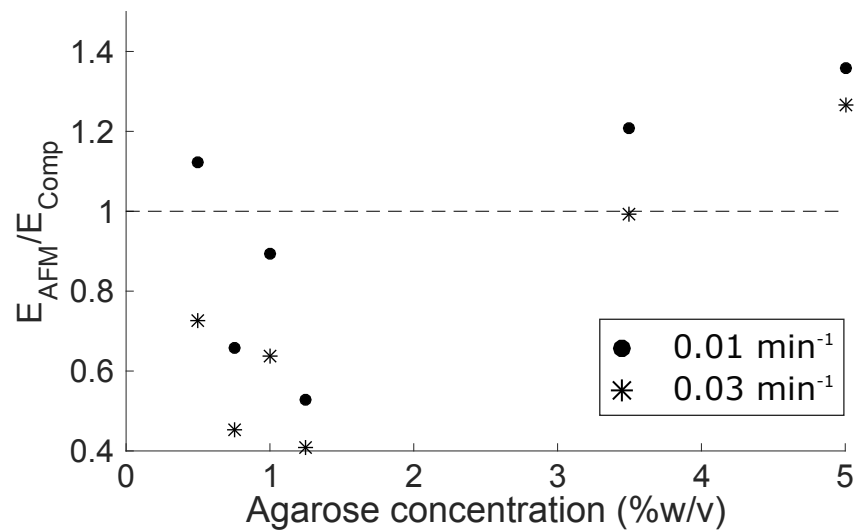


FIGURE 5.3: Shows the ratio between the elastic modulus from the AFM microindentation experiments (E_{AFM}) and the results from the conventional compression tests (E_{Comp}). In conventional compression test two different strain rates were investigated (0.1 min^{-1} and 0.3 min^{-1}).

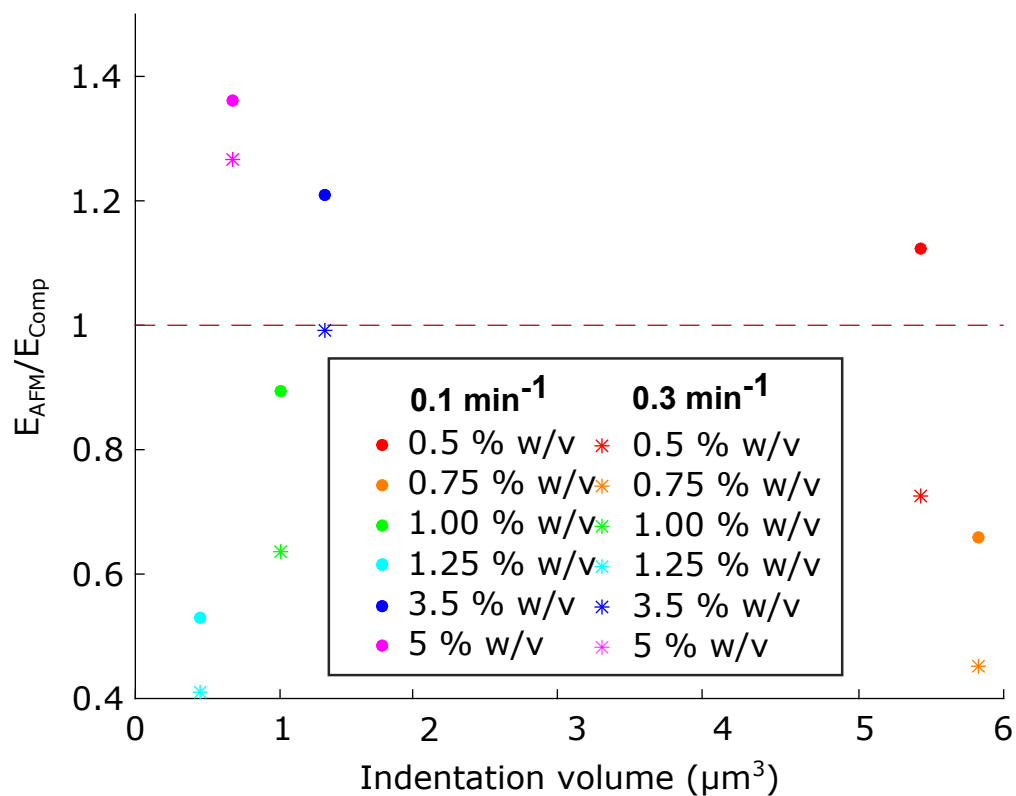


FIGURE 5.4: Shows the ratio between the elastic modulus from the AFM microindentation experiments (E_{AFM}) vs. the mean indentation volume and the results from the conventional compression tests (E_{Comp}) for each agarose concentration and compression speed. In conventional compression test two different strain rates were investigated (0.1 min^{-1} and 0.3 min^{-1}).

parameters when performing strain rates of 3 min^{-1} to 15 min^{-1} [54]. Compression tests on Agarose gels with similar concentrations as in this thesis were done with strain rates of 0.26 min^{-1} and 0.13 min^{-1} [38]. A standardised compression test on agarose gels with different concentrations to validate AFM nanoindentation results from experiments on porcine cartilage was used in [53]. Standards like DIN ISO 7743:2016-08 used for investigating rubber by compression tests demand strain rates of 1.25 min^{-1} and 2.5 min^{-1} . For this thesis it was assumed that, to possible speed dependent-phenomena (viscoelasticity), when using even lower strain rates, as have been chosen for previous studies. This assumption was, however, not be supported by the results as the elastic modulus decreases for nearly all of the gels from high to the low compression speed (see fig. 5.1). As AFM experiments were done with just one piezo-extension speed= $0.5 \text{ }\mu\text{m/s}$) the lower ratios for higher strain rates in (agarose conc. $<1.5\%$) figure 5.5 originate from higher compression moduli of the compression tests (see table 5.2). However, results from the compression tests show similar values compared to the ones presented in [38]. Agarose gels with concentrations of $0.5\%w/w$, $0.7\%w/w$, $1\%w/w$, $2.5\%w/w$ and $5\%w/w$ were investigated and elastic moduli of $5.3\pm 0.25 \text{ kPa}$, $14\pm 1 \text{ kPa}$, $38\pm 2 \text{ kPa}$, $254\pm 20 \text{ kPa}$ and $929 \pm 48 \text{ kPa}$ were derived for these, respectively. The results indicate that differences in mechanical properties of homogeneous materials identified on the macro-scale, show similar values when investigating the same material using microindena-tion type AFM (see fig. 5.5 and fig. 5.6).

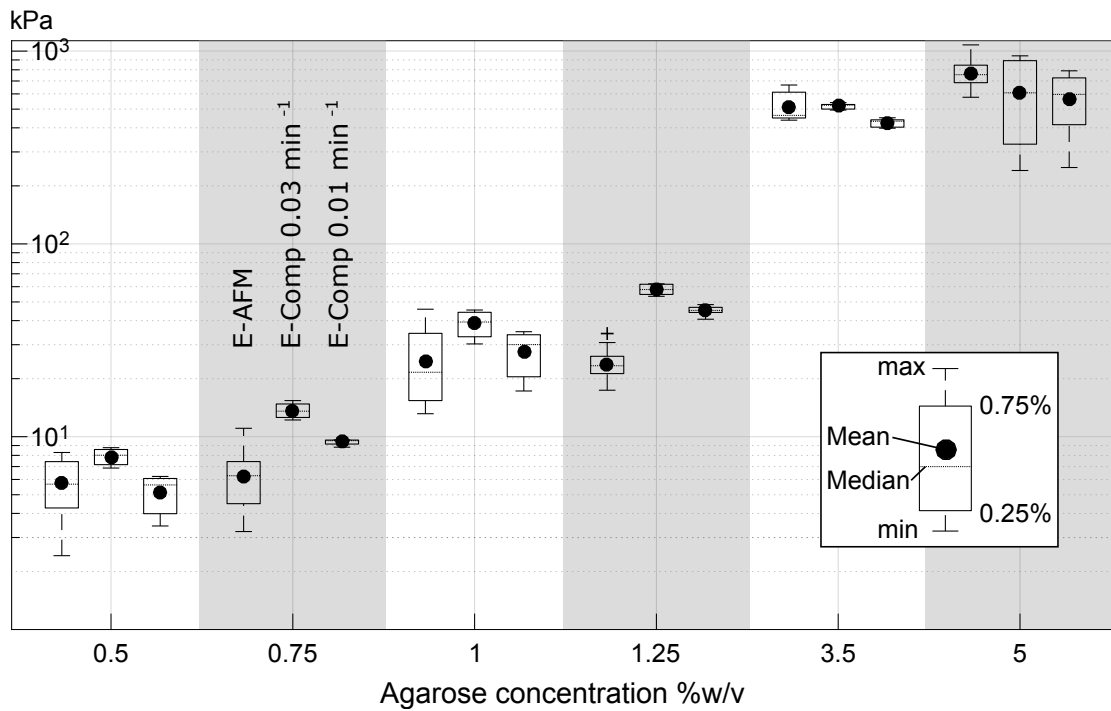


FIGURE 5.5: Shows the results from AFM-type indentation experiments and the conventional compression tests on agarose gels. The results confirm that trends from homogeneous materials with gradually different mechanical properties on the macro-scale (compression tests) can also be detected by using microindentation type AFM.

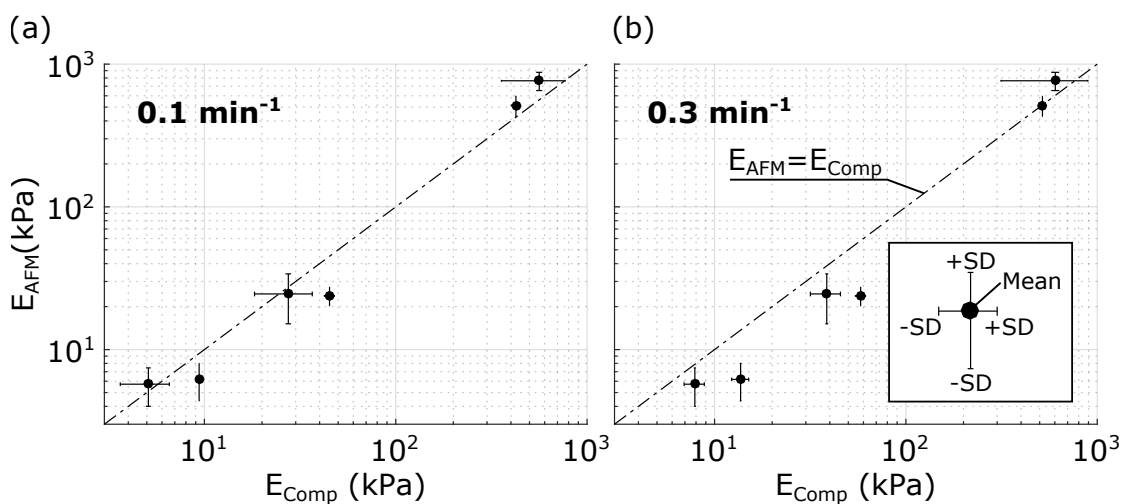


FIGURE 5.6: Shows the mean- and the corresponding standard deviation values for the different agarose concentration of the indentation- (AFM) and the compression (Comp) experiments presented using error-bars. (a) Shows the data for the low compression speeds (0.3 min^{-1}) and (b) the data for the high compression speed (0.3 min^{-1}).

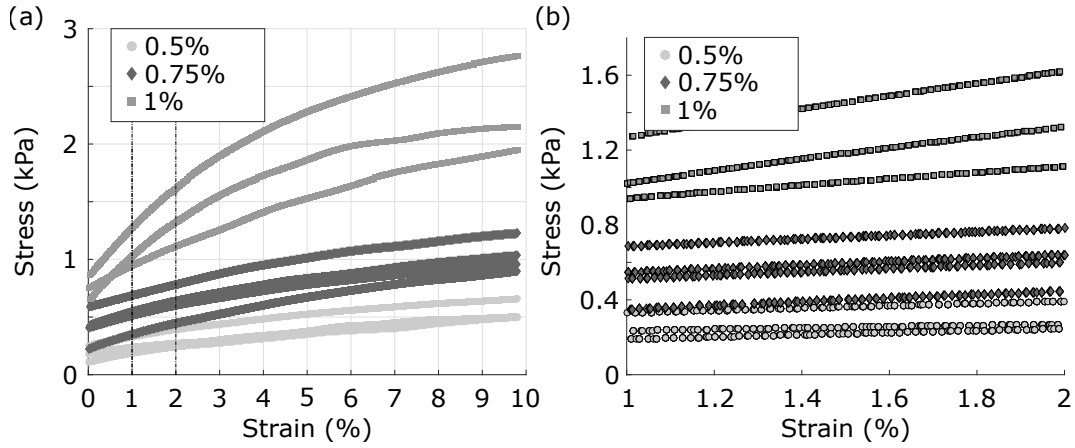


FIGURE 5.7: The macro-scale compression modulus of the cylindrical samples was calculated as the slope of the stress-strain diagram, in the strain range of 1- 2% (see fig. 4.7 (a)). The stress strain data was obtained by normalising the displacement data with the initial height of the sample and by normalising the force data from the load cell by the initial cross sectional area (see fig. 4.7 (b)).

5.3 Microindentation on tendons

Data from microindentation type AFM on longitudinal- and transversal tissue cut samples was analysed according to sections 3.4.3, 4.2.1 and 4.3.2. These results are summarized in figs. 5.8 and 5.9 and tables 5.3, 5.4, 5.5 and 5.6 and answer the main questions of the thesis by showing differences in the indentation modulus according the type of tendon (CDET and SDFT), the tendon zones (FM and IFM) and age (3 years old and 18 years old tendons). To compare micro-indentation results from composite structures, it is necessary that interaction of the tip and the material is similar for all types of samples and zones. If just one micro-sphere diameter is used in the experiments similar contact depths guarantee comparability. In this thesis two different sphere diameters were used (10 μm and 15 μm) and therefore the indentation volume (IV), so the spherical cap of the tip being in real contact with the sample was chosen as target parameter to guarantee comparability. The indentation volume is defined as

$$IV = \frac{\pi h_c^2}{3} (3R_{TGT1 \text{ or } LT} - h_c) \quad (5.1)$$

with h_c (μm), R_{TGT1} (μm) or R_{LT} (μm) the contact depth and the sphere radius from TGT1 (10 μm spheres) or trench imaging in longitudinal direction (15 μm spheres) respectively. Then the data was filtered to be in the range of $1 \mu\text{m}^3 < IV < 3 \mu\text{m}^3$ as already described in 4.2.1 (There also the percentual amount of excluded data is presented). Significant differences can be seen with increasing

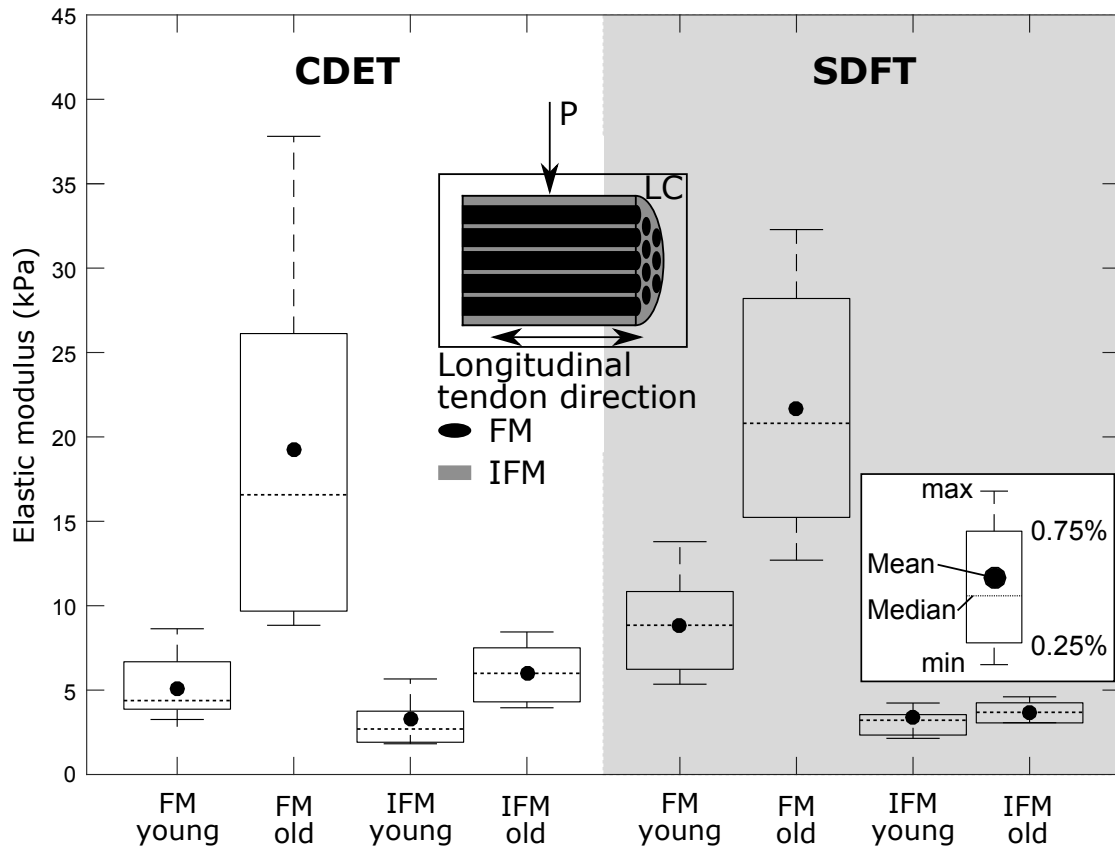


FIGURE 5.8: Shows the results from the microindention type AFM experiments on longitudinal tissue sections from common digital extensor- (CDET) and superficial digital flexor tendons (SDFT). Both fascicular- (FM) as also interfascicular matrix (IFM) was investigated from one young (3 years) and one old (18 year) horse.

age in both tendon types for the fascicular matrix (FM) and for the interfascicular matrix (IFM). The results from experiments on longitudinal tendon sections are shown in figure 5.8 and table 5.3 whereas results from the transversal cuts are presented in figure 5.9 and table 5.4. In these samples the FM and IFM could not clearly be identified. Therefore the elastic modulus from these samples could not be assigned to the FM or the IFM.

5.3.1 Micromechanical properties of LC and TC tendon sections

Results from the longitudinal cut samples show a significant increase in elastic modulus for the fascicular (FM)- and the interfascicular (IFM) matrix for both tendon types with age (see tab. 5.5). Thereby the changes from young to old in the FM are 275% and 225% and in the IFM 111% and 65% for the CDET and the SDFT respectively, related to the young tendons (see tab. 5.3). The IFM of

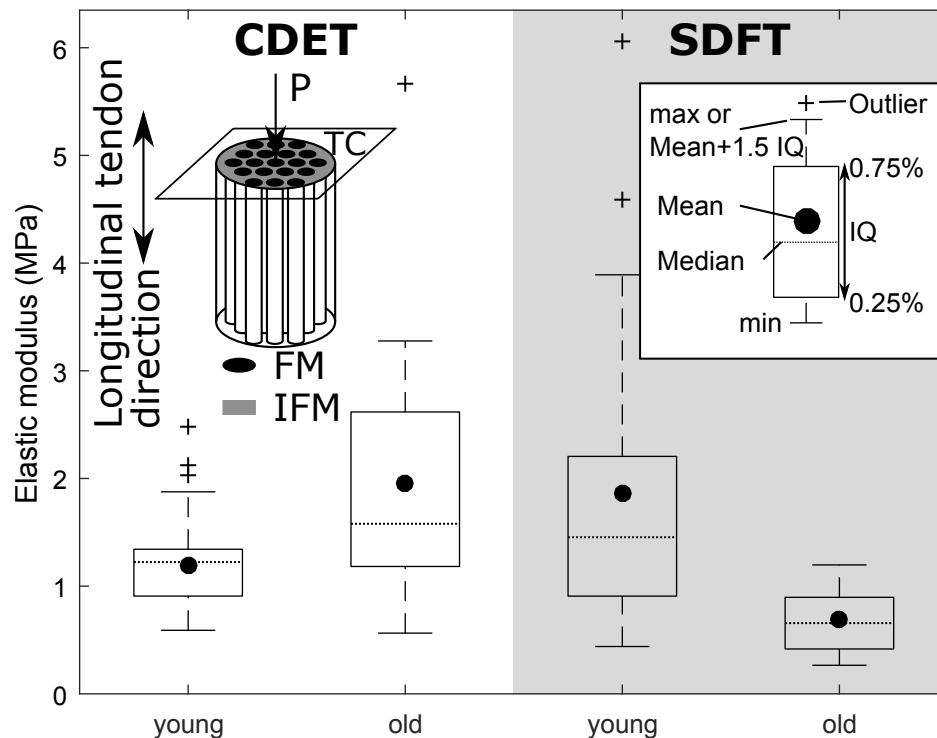


FIGURE 5.9: Shows the results from the microindention type AFM experiments on transversal tissue sections from common digital extensor- (CDET) and superficial digital flexor tendons (SDFT) from a young (3 years) and one old (18 years) horse. Due to the fact that the fascicular- and the interfascicular matrix could not be differently identified in these samples they could not be distinguished separately. The results shown in this diagram combined with an increase of extrafibrillar crosslinks (fig. 5.8), a decrease of elastic modulus of individual collagen fibrils (fig. 5.13) and a constant individual collagen fibril diameter (fig. 5.16) leads to the assumption of crosslinks mainly being in charge for shifting the CDET values to higher values assuming buckling to be a dominating principle when loading in fibril direction.

sample zone	CDET young		CDET old		SDFT young		SDFT old	
	FM	IFM	FM	IFM	FM	IFM	FM	IFM
mean E-modul (SD) in kPa	3.93 (1.4)	2.18 (1)	14.75 (7.37)	4.6 (1.45)	6.81 (2.3)	2.26 (0.64)	22.14 (7.26)	3.73 (0.84)
mean IV (SD) in μm^3	3.84 (0.98)	3.18 (1.03)	3.1 (0.82)	3.69 (1.51)	2.34 (0.52)	2.85 (0.64)	1.54 (0.51)	1.66 (0.67)
min DZ-slope	0.26	0.38	0.15	0.24	0.44	0.31	0.17	0.09
max DZ-slope	0.52	0.71	0.27	0.35	0.74	0.52	0.34	0.13
n	1	1	1	1	1	1	1	1

TABLE 5.3: Shows the results from microindention experiments on longitudinal tendon cut samples. The indention volume (IV) was chosen to be in the range of $1 < IV < 3 \mu\text{m}^3$ to make the mechanical results more comparable. The number of samples been tested is given by n.

sample	CDET young	CDET old	SDFT young	SDFT old
mean E-modul (SD) in MPa	1.17 (0.37)	1.89 (1.15)	1.80 (1.26)	0.67 (0.29)
mean IV (SD) in μm^2	2.2 (0.59)	1.87 (0.57)	1.87 (0.57)	1.79 (0.63)
min DZ-slope	0.33	0.31	0.26	0.17
max DZ-slope	0.68	0.78	0.76	0.46
n	1	1	1	1

TABLE 5.4: Shows the results from microindentation experiments on transversal tissue sections. The indentation volume (IV) was chosen to be in the range of $1 < IV < 3 \mu\text{m}^3$ for making the mechanical results more comparable. The number of samples having been tested is given by n

Combination	Levene's test p- values				p_{ANOVA}
	P_{abs}	P_{sqr}	P_{log}	P_{rez}	
IFM_y CDET vs. IFM_o CDET	0.3189	0.9669	0.3303	0.0332	0.0017
IFM_y SDFT vs. IFM_o SDFT	0.7402	0.7258	0.3570	0.1018	0.0019
IFM_y CDET vs. IFM_y SDFT	0.1676	0.1333	0.1072	0.0920	0.8075
IFM_y CDET vs. IFM_o SDFT	0.5572	0.2579	0.1040	0.0351	0.8075
IFM_o CDET vs. IFM_y SDFT	0.0244	0.1796	0.8319	0.1424	0.0003
FM_y CDET vs. IFM_o CDET	0.8921	0.8218	0.7555	0.6407	0.3782
FM_y CDET vs. FM_y SDFT	0.0389	0.2362	0.8717	0.1731	0.0018
FM_o CDET vs. FM_o SDFT	0.9320	0.2648	0.0375	3.7E-4	0.0018
FM_o CDET vs. FM_y SDFT	0.0014	0.0066	0.0846	0.2841	0.0020

TABLE 5.5: Shows ANOVA implemented in Matlab applied on microindentation longitudinal cut results. The equality of variance was tested on original (abs) and transformed- (square-root (sqr), logarithmic (log), reziproke (rez)) data. ANOVA was done on data with most similar variance (highest p_{xxx} value). Different interesting combinations according zone (IFM, FM), tendon type (CDET, SDFT) and age (young (y), old (o)) were investigated. The similarity of the specific tested combination of the mean values is represented by p_{ANOVA}

Combination	Levene's test p- values				P_{ANOVA}
	P_{abs}	P_{sqr}	P_{log}	P_{rez}	
CDET_o vs. SDFT_y	0.0013	0.0086	0.3656	0.0023	2.8E-6
CDET_o vs. SDFT_y	0.8168	0.6118	0.4176	0.1513	0.7863
CDET_y vs. CDET_o	2.1E-7	3.8E-6	3.5E-4	0.1718	0.0092
CDET_y vs. SDFT_o	0.4343	0.6789	0.0339	3.4E-8	5.6E-7
CDET_o vs. SDFT_o	0.0013	0.0086	0.3656	0.0023	2.8E-6
SDFT_y vs. SDFT_o	0.0018	0.0038	0.1081	0.0149	2.2E-5

TABLE 5.6: Shows ANOVA from microindention transverse cut results. The equality of variance was tested on original (abs) and transformed- (square-root (sqr), logarithmic (log), reziproke (rez)) data. ANOVA was done on data with most similar variance (highest p_{xxx} value). Different combinations of interest according tendon type (CDET, SDFT) and age (young (y), old (o)) were investigated.

the old CDET reaches slightly but significantly higher values than the FM of the young CDET, whereas the IFM from the old SDFT is smaller than the FM of the young CDET. The IFM of the young SDFT and the young CDET show no significant differences whereas the IFM of the old CDET shows higher values than the one originating from the IFM of the SDFT. The FM of the young CDET shows significantly lower values than for the young SDFT whereas this trend is kept the same for the old samples.

The transverse cut samples show different results. FM and IFM could not be distinguished via light microscope in these samples which makes it impossible to compare the zones separately. However the elastic modulus shows an increase of 62% for the CDET and a decrease of 63% for the SDFT related to the results of the young tendons (see tab. 5.4 and tab. 5.6). The elastic modulus of the old SDFT even falls beneath the value of the young CDET.

The most striking difference between the results of the longitudinal- and the transverse cut sample is the magnitude of the elastic modulus. Whereas longitudinal cut samples show an elastic modulus in the 1-40 kPa range, results from the transverse cuts are 2-3 orders of magnitude higher, in the MPa range. The most likely explanation therefore is illustrated in figure 5.10. Fascicles are stacks of single collagen fibrils. When they are loaded in transversal direction (longitudinal cut samples, fig. 5.11 (a)) The reaction forces arise from the transverse stiffness of individual collagen fibrils and from the interfibrillar crosslinks, which prevent fibrils from being pushed apart when other fibrils

from the upper are pressed between them (illustrated in figure 5.11 (a)). Therefore, microindentation tests in fascicles transverse direction might mainly gain information about the amount and the strength of these interfibrillar crosslinks and the transverse stiffness of individual fibrils. Here individual fibrils had an elastic modulus of 1.25 MPa and 3.53 MPa for the CDET and 5.65 MPa and 2.24 MPa for the SDFT for young and old horses, respectively (c.f. section 5.4). The microindentation results on the other hand had an elastic modulus of 3.93 kPa and 14.75 kPa for the CDET and 6.81 kPa and 22.14 kPa for the SDFT for the young and old horses respectively. The fact that there is a three magnitude difference between the elastic modulus values of the transverse cuts and individual collagen fibrils suggests, that the dominant mechanism specifying the elastic modulus of the longitudinal cuts is in fact the crosslinking. Further, an increase in interfibrillar crosslinking would also explain why all of tendon zones (FM and IFM) for the two tendon types become stiffer during ageing as cross-linking is an age-dependent mechanism [55][50].

The fact that the FM is stiffer than the IFM can be explained by the fibril organisation of the individual collagen fibrils in these specific zones. It is well known, that the FM is a highly orientated zone, where fibrils are aligned densely packed in a more or less wavy pattern. The IFM on the other side is less orientated, consisting of fibrils aligned more isotropically [27]. This structure was also observed in a contact mode scan over a FM- IFM- FM zone with a sharp cantilever, as used for nanoindentation experiments (see fig. 5.12). Fibrils from the IFM tend to go from one FM to the neighbouring one and connect these two zones. The more isotropically arrangement might also be the reason for the flexibility of this zone [59] assuming fibrils being able to align when two neighboured FMs are moving relatively to each other. Interfibrillar crosslinks appear on any positions between two fibrils [18]. If fibrils are less orientated, as it is the case in the IFM, two fibrils might mostly not be that close over a long distance to develop crosslinks, as they are frequently crossed by other fibrils. This could be an explanation for the elastic modulus of the IFM tending to be lower than the FM but still increasing during ageing. Fibrils in the FM on the other hand are aligned very close to each other over long distances and therefore give the opportunity to develop more crosslinks between two fibrils. An increase of interfibrillar crosslinks during ageing also explain why the elastic modulus of the FM and the IFM tends to be very similar for the young horses. To strengthen this explanation it would be interesting to investigate tissue from even younger horses where fibrils tend to be crosslinked even less.

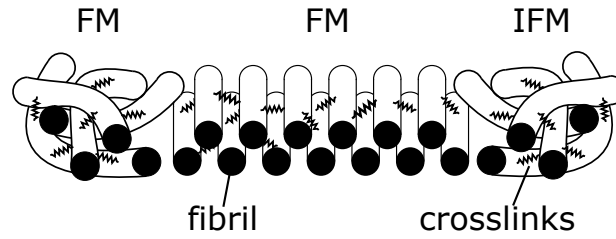


FIGURE 5.10: Illustrates the differences in the fascicular (FM) and the interfascicular (IFM) according the fibril orientation.

When loading fascicles in longitudinal direction (transverse cut samples) the counterforce might mainly be due to the single fibrils compression and buckling tendency. Simplifying the fibrils to be very slim homogeneous beams without any constraint from fibril surrounding crosslinks, makes it possible to investigate the critical buckling force by using the Euler-Bernoulli beam theory. Thereby this force is defined as

$$P_{crit} = \frac{EI_{min}\pi^2}{s^2} \quad (5.2)$$

with E as the fibrils elastic modulus (N/m^2), $I(d_{fibril})$ (m^4) the minimum geometrical moment of inertia and s (m) the free buckling length. The free buckling length depends on how the buckling fibril is considered to be constrained i.e. being L if the ends are completely free or $0.5L$ in fixed conditions, with L as the fibril length. Assuming the tissue in transversal direction becoming stiffer for higher values of P_{crit} and the fact that $P_{crit} \propto EI$ defines the fibrils elastic modulus and its diameter as the main influencing parameters. Therefore larger and stiffer fibrils in the tissue would lead to a higher elastic modulus, whereas fibrils with a smaller diameter and a elastic modulus would lead to lower values. To confirm this hypothesis geometrical and mechanical results from single fibrils on the nano level are necessary, which are presented in the the following section. Anticipating the mean values of these results and combining them with the results of the microindentation experiments from transversal cuts makes it possible to assess the critical buckling force by using 5.2 and comparing it with the force a single fibril was compressed with (mean values presented in table 5.7) when using the following assumptions:

- Each fibril being compressed extends from the very bottom to the top of the transverse cut sample.
- The forces compressing each fibril are ideally vertically aligned with the longitudinal axis of the fibril.

	CDET_young	CDET_old	SDFT_young	SDFT_old
sample height h (μm)	10	10	10	10
mean fibril elastic modulus (MPa)	1.28	3.53	5.65	2.24
mean fibril diameter in PBS (nm)	187	140	154	143
fibril cross sectional area (μm^2)	0.027	0.015	0.019	0.016
mean F_{max} (nN)	117	222	195	340
mean contact area (μm^2)	13.5	12.4	12.4	12.1
amount of fibrils	490	805	668	754
P_{crit} (pN) with $s=h$	7.57	6.58	15.2	4.54
P_{crit} (pN) with $s=0.5h$	30.3	26.3	60.9	18.1
fibril-compressing force (pN)	238	275	292	451

TABLE 5.7: Shows the mean values from micro- and nanoindentation experiments to use them for calculating critical buckling forces P_{crit} for two different types how fibrils are constrained on their ends (no constraint ($s=h$), fixed on both ends ($s=0.5h$)).

- Crosssections of the fibrils are constant over the length and have got a circular shape, making it possible to calculate it from the diameter in PBS as measured by AFM.
- All fibrils in the penetrated area have got the same diameter (calculated from the mean value of the fibrils in PBS).
- The amount of fibrils is calculated by dividing the contact area by the mean cross section area of a single fibril.
- All of the fibrils are loaded with the same force so that the compression force for one fibril results from the the maximum force, the region is investigated with, divided by the number of fibrils.

Under these assumptions and when using the results from the nanoexperiments, P_{crit} reaches values which are lower than than any single force applied on a single fibril. Even when fibrils are assumed to be fixed on both ends, ($s=0.5h$) still individual fibrils buckle theoretically under the used experimental conditions.

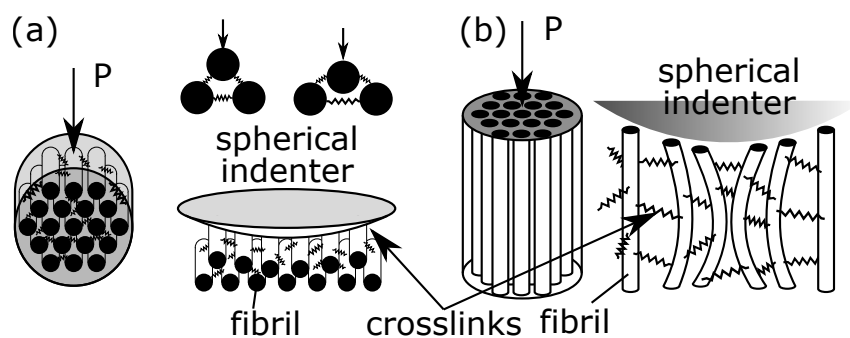


FIGURE 5.11: Illustrates how fibrils in the tendon tissue might react due to external force applied in longitudinal (a) and transversal (b) direction. While the stiffness of the transverse cut samples is mostly dominated by the fibrils stiffness (E-modul), interfibrillar crosslinks might provide the predominant counterforce to keep the fibrils from sliding apart when loading in transversal direction.

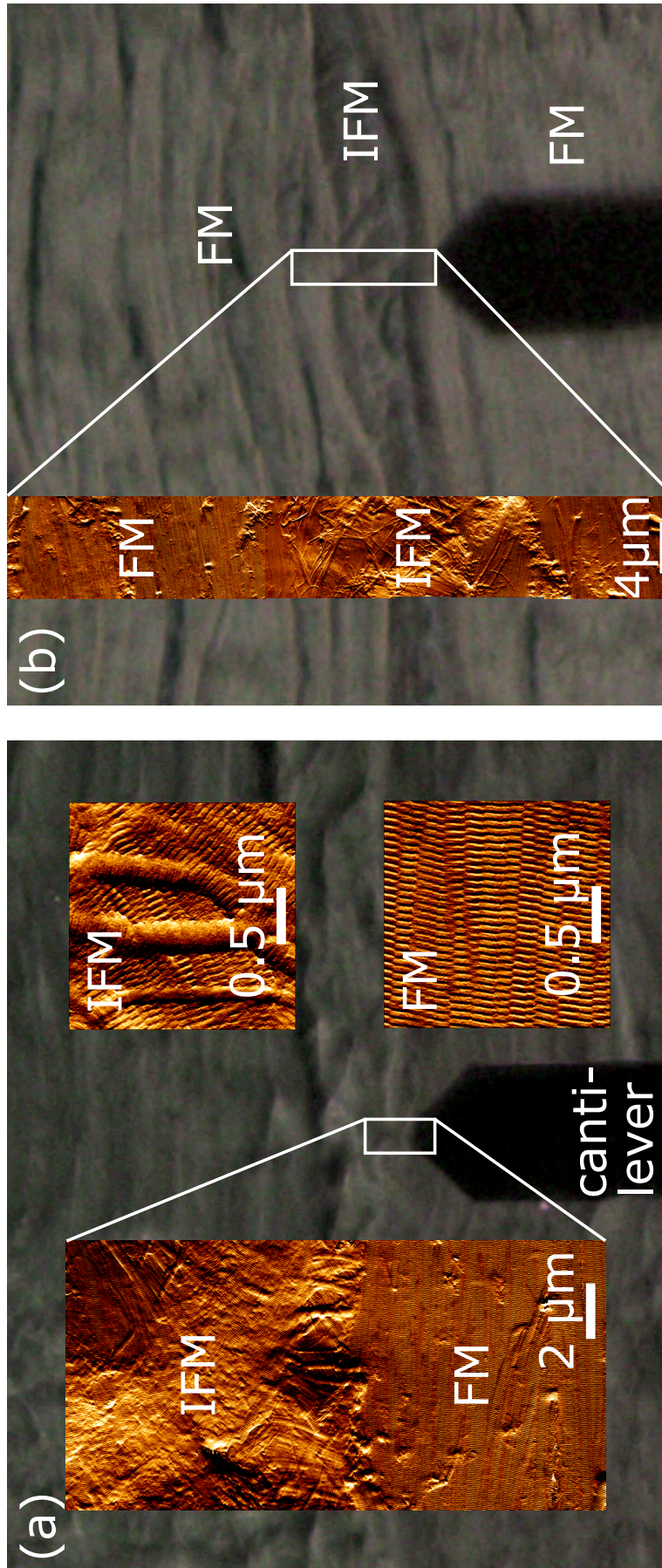


FIGURE 5.12: Shows images of fascicular- (FM) and interfascicular matrix (IFM). Whereas fibrils in the FM are highly orientated, the fibrils in the IFM have no distinct orientation, initiating a lower packing density which might be the explanation for lower values in elastic modulus.

5.4 Nanoindentation on individual collagen fibrils

Results from nanoindentation experiments on individual collagen fibrils show an increase of elastic modulus from young to old in the CDET. The elastic modulus of the SDFT fibrils on the other hand decreases during ageing. Thereby the percentage changes from young to old tissue of the elastic modulus are 176% and -60% for the CDET and the SDFT respectively (see tab. 5.9). Fibrils from the young and the old SDFT are both stiffer than fibrils from the young CDET. These findings strengthen the hypothesis of the previous section, that the elastic modulus of transverse cut sections is mainly influenced by the elastic modulus of the single collagen fibrils. Both results, from the microindentation transverse cut samples and the nanoindentation experiments, show the same trend according to ageing for each tendon type. Furthermore, quantitative comparison shows that the microindentation elastic moduli for both tendons are smaller than for the nanoindentation. The nanoindentation results show a higher elastic modulus for the young SDFT compared to the old CDET fibrils, whereas the microindentation results from the transverse cuts do not show this difference. Based on the hypothesis that the fibrils are buckling, a parameter, which could explain this would be fibril diameter differences, which were investigated in the swelling experiments, presented in the next section. However no difference in average diameter was detected (c.f. 5.8). Therefore, the fact that the microindentation results from the transverse cuts of the old CDET and young SDFT are not following the fibril results could be explained in the following way: The microindentation results on the transverse are cuts predominantly influenced by the interfibrillar crosslinks. Hence, once can argue that the higher elastic modulus of the old CDET compared to young SDFT for both FM and IFM (c.f.

Combination	p-value
CDET_young vs. SDFT_young	0.1897
CDET_young vs. SDFT_old	0.3939
SDFT_young vs. CDET_old	1
CDET_young vs. CDET_old	0.1897
SDFT_young vs. SDFT_old	1
CDET_old vs. SDFT_old	0.8182

TABLE 5.8: The null-hypothesis, whether the diameter data, originating from individual collagen fibrils in PBS, comes from continuous distributions with equal medians was tested by using a non-parametric Wilcoxon rank sum test, with the hypothesis being accepted for $p > 0.05$. The table shows the different combinations and their p-values respectively.

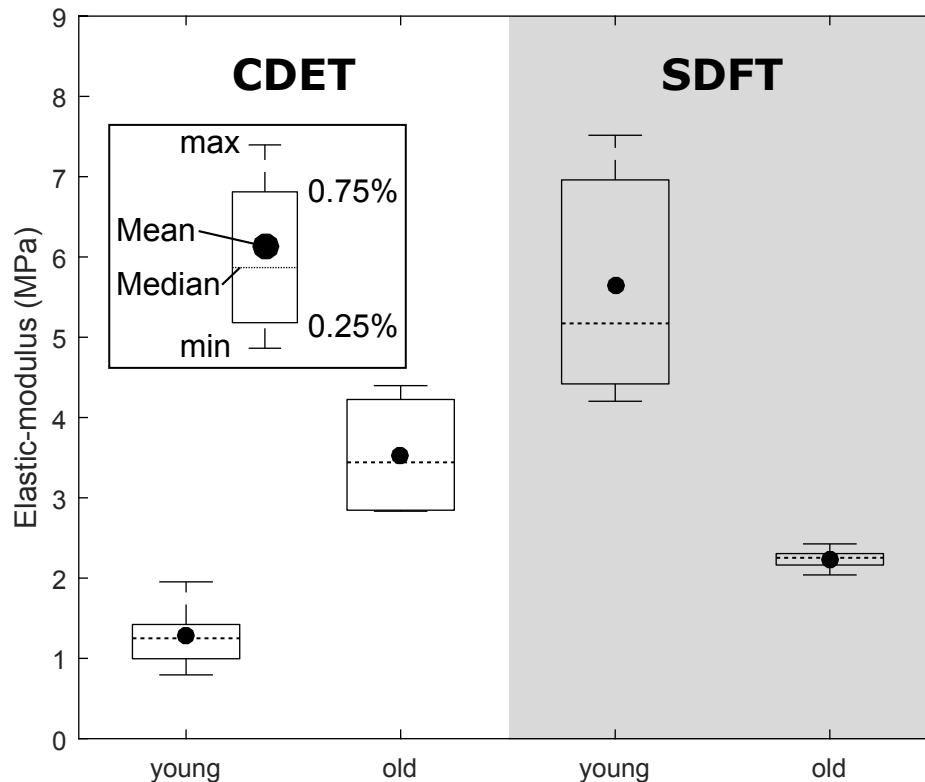


FIGURE 5.13: Shows results from the nanoindentation experiments on individual collagen fibrils. During ageing fibrils from the common digital extensor tendon become stiffer, whereas from the superficial flexor tendon become softer. The same trend can be seen in the microindentation transversal tissue samples.

5.8 and table 5.5) is linked to this effect. Therefore, old CDET has overall higher crosslinking between fibrils which could also be contributed to buckling behaviour. In fact this would increase P_{crit} in the old CDET, such that the difference detected in the nanoindentation data of the individual collagen fibrils (old CDET vs young SDFT) this appears, when conducting microindentation tests on the transverse cuts.

Limitations of this interpretations are of course, that we have no analytical chemistry data for these samples detailing potential differences in crosslinking, and, that we have measured only the transverse modulus of the individual collagen fibrils. However, for the latter a correlation between the transverse and the longitudinal elastic modulus does exist (private conversation with Andriotis O. PhD).

sample	CDET young	CDET old	SDFT young	SDFT old
mean E-modul (SD) (MPa)	1.28 (0.40)	3.53 (0.70)	5.65 (1.35)	2.24 (0.13)
Contact Depth (SD) (nm)	18.9 (5.6)	12.5 (1.1)	14.8 (5.8)	13.2 (0.6)
min DZ-slope	0.19	0.25	0.25	0.27
max DZ-slope	0.41	0.47	0.51	0.58
n	6	6	7	6

TABLE 5.9: Shows the results from nanoindentation experiments of individual collagen fibrils. As just one type of cantilever was used with one specific tip geometry the contact depth (nm) was used instead of indentation volume (IV)

Combination	Levene's test p- values				P_{ANOVA}
	P_{abs}	P_{sqr}	P_{log}	P_{rez}	
CDET_o vs. SDFT_o	0.0004	0.0005	0.001	0.009	1.2E-4
CDET_o vs. SDFT_y	0.0444	0.1607	0.5520	0.1946	0.0031
CDET_y vs. CDET_o	0.0434	0.5351	0.4321	0.0398	2.8E-5
CDET_y vs. SDFT_o	0.0849	0.0442	0.0264	0.0172	2.4E-4
CDET_y vs. SDFT_y	0.0048	0.1007	0.6756	0.0171	8.4E-7
SDFT_y vs. SDFT_o	7.3E-4	0.0014	0.0038	0.1339	5.8E-8

TABLE 5.10: Show ANOVA applied on nanoindentation results. The equality of variance was tested on original (abs) and transformed- (square-root (sqr), logarithmic (log), reziproke (rez)) data. ANOVA was done on data with most similar variance (highest p_{xxx} value). Different combinations of interest according tendon type (CDET, SDFT) and age (young (y), old (o)) were investigated.

	CDET_young	CDET_old	SDFT_young	SDFT_old
mean D_{PBS}/D_{AIR} (SD) in %	213.2 (26.1)	150.7 (2.71)	164.5 (3.27)	168.8 (11.5)
n	7	6	7	6

TABLE 5.11: Shows the results of the swelling ratios (D_{PBS}/D_{AIR}) of individual collagen fibrils for different samples. The number of individual collagen fibrils having been tested is given by n.

5.4.1 Swelling behaviour

Swelling is a common phenomenon in biological tissues and necessary to adapt their properties. Collagen fibrils have the ability to change their size and therefore adapting their mechanical characteristics. Geometrical investigations were done on dry fibrils in air just for swelling measurements by imaging in contact mode and afterwards the same fibrils were investigated in PBS (pH= 7,4) using force mapping mode to simultaneously get the elastic modulus and the geometry from each fibril. All of these fibrils showed swelling ratios (D_{PBS}/D_{AIR}) of at least 150% up to 270%. The results furthermore show that swelling changes during ageing for specific tendons (see fig. 5.15). Whereas the SDFT shows no differences in swelling between young and old horses, the CDET fibrils swell more if the tendon becomes older, perhaps indicating increased turnover within the tissue. For the absolute diameter values for fibrils in PBS no significant differences among the different groups were determined. Hydration generally softens tissues. Figure 5.17 shows the relation between swelling ratio and the elastic modulus of individual collagen fibrils from nanoindentation experiments. The CDET fibrils tend to swell less in older tendons, leading to higher values for the elastic modulus as suggested. For the SDFT on the other hand the swelling behaviour seems to be similar in old and young tendons whereas the elastic modulus seems to be higher for the young tendon. The change seen with age in both tendon types might in fact have mechanobiological causes. In this sense the positional CDET tendon becomes stiffer in age, which is reflected by a decrease in collagen fibril swelling. For the SDFT no difference in swelling could be observed, however the SDFT seems to have a decreased stiffness with age.

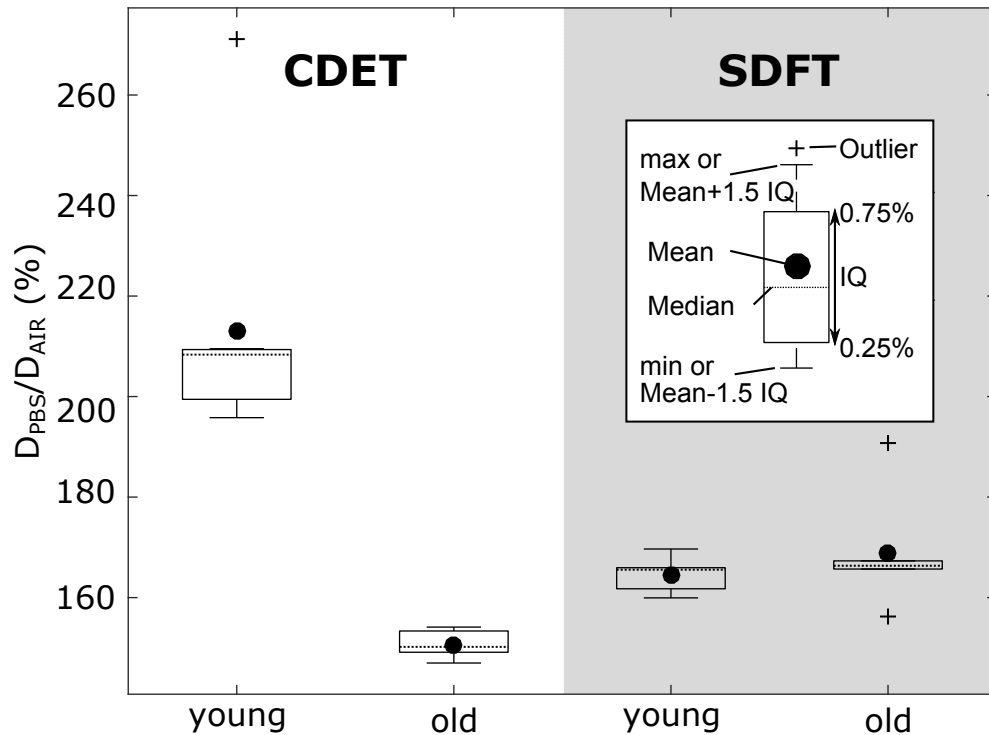


FIGURE 5.14: Shows the swelling behaviour of individual collagen fibrils. Whereas fibrils from the CDET tendon decrease due to ageing the swelling ratio of fibrils from the SDFT tend to keep the same.

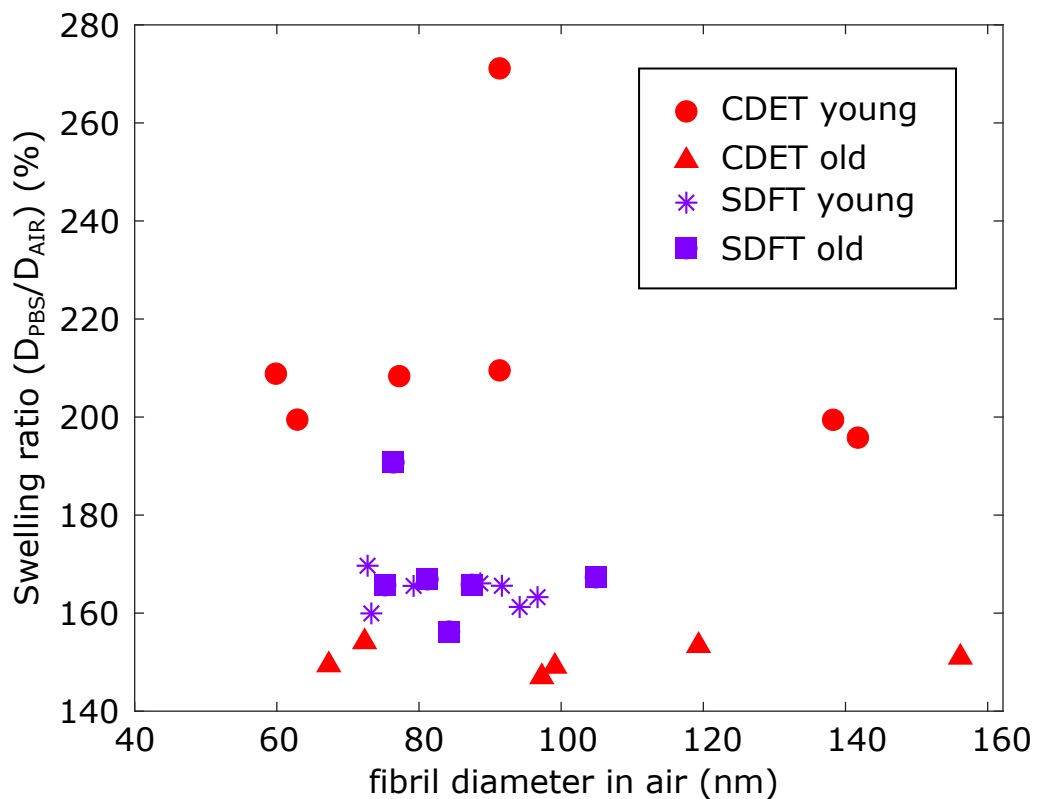


FIGURE 5.15: Shows the swelling ratio for individual collagen fibrils which were hydrated completely in PBS (pH 7.4) from a previously dry state.

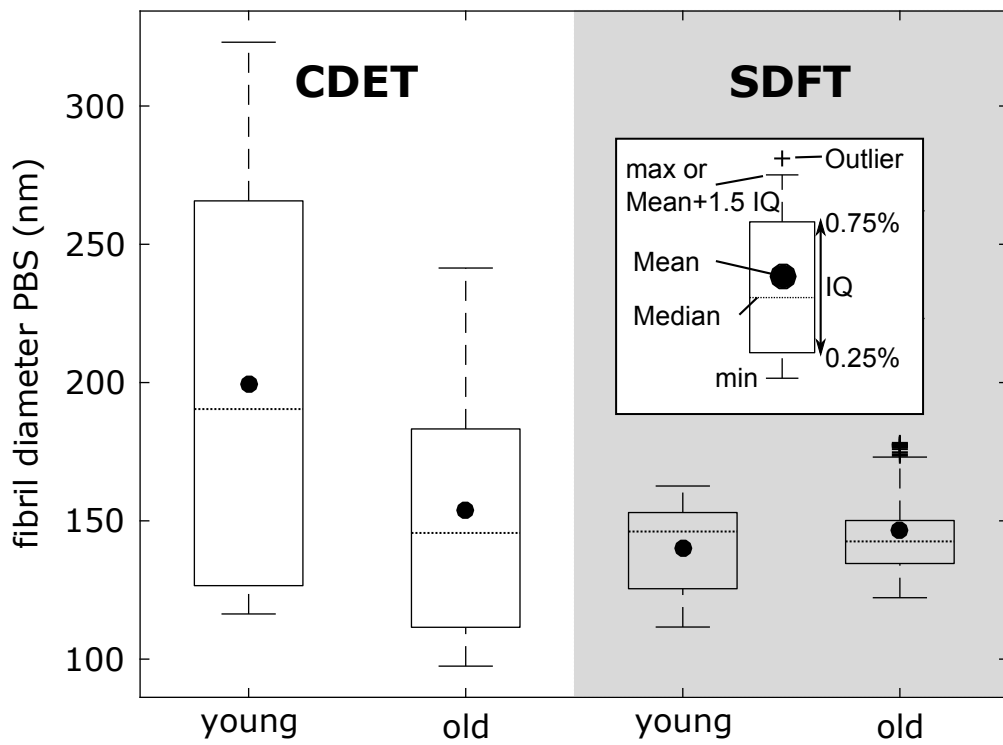


FIGURE 5.16: Shows the fibril diameters of SDFT and CDET tendons placed in PBS.

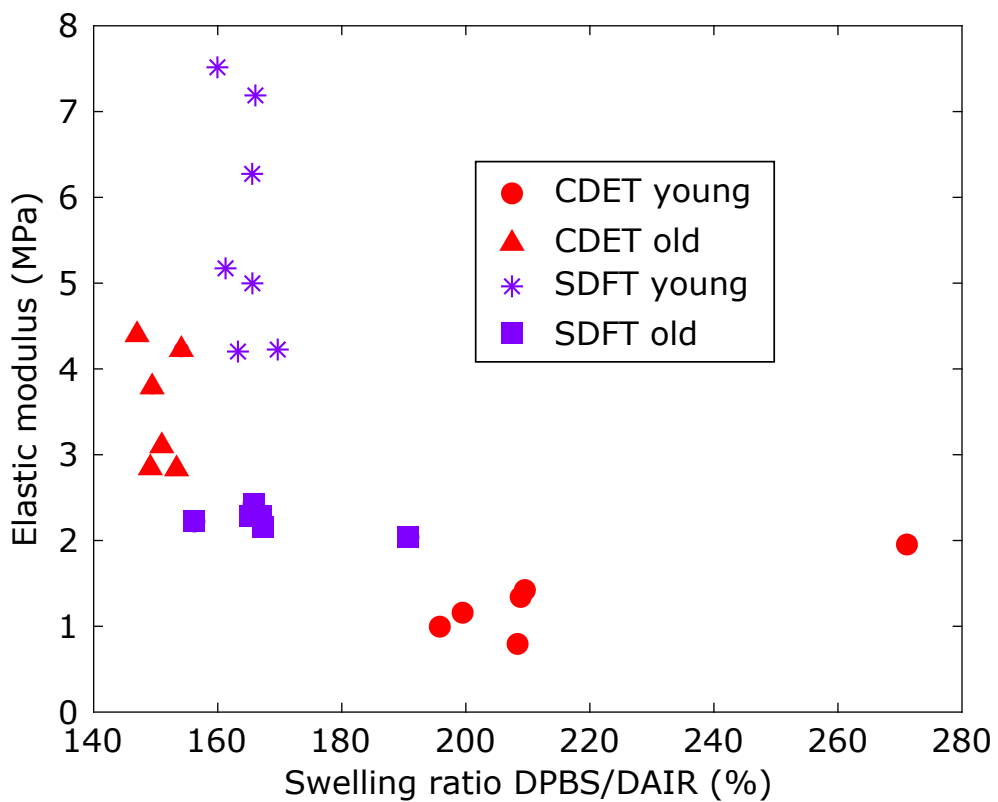


FIGURE 5.17: Shows the relation between swelling ratio and the elastic modulus of individual collagen fibrils.

5.5 Comparison to literature

The microindentation results from fascicles in longitudinal direction (transverse cut samples) should be best comparable to tensile experiments on isolated fascicles. As our samples originated from one horse of each group having been investigated in the study [59] these results were taken as reference for comparison. In this paper fascicles were tested via tensile tests in physiological longitudinal direction. Therefore trends from these results should be comparable to compression tests in the same direction, i.e. microindentation tests of the transverse cut samples. However, there are striking differences between the results from these experiments. The first difference is the range of the data. Both, the reference data and the data from this thesis reports elastic modulus values in the MPa region, but the values in [59] are two orders of magnitude higher. An explanation for this might be the way how samples were hydrated. Changes in elastic modulus according to hydration and different pH values of the liquid were already explained in [19] and could explain the difference here. Both, the investigations in this thesis and also the one in the reference paper used PBS with pH=7.4 to keep samples in wet condition. But, in this thesis a bath was used and therefore the samples were hydrated through submersion the whole time. The samples in the reference paper on the other hand were stored in tissue damped with PBS before and after the experiments. While this was done to ensure hydration of the samples, samples might have in fact been partly dehydrated during the mechanical tests. Further, preconditioning of the samples by loading and unloading the samples repetitively, most likely means that crimp is no longer present in the samples. Additionally one can assume that each loading cycle forces PBS out of the sample leading to further dehydration. As this is done several times. Consequently one can assume the sample to be already very dry during the actual experiments. Another reason could be the crimp. In our experiments crimp could of course have a significant effect on the measured elastic modulus in longitudinal direction. Due to the fact that such wavy structures compressed in longitudinal direction for sure do not withstand that much force, as if the structures were completely straight and pulled (as it is the case in the tensile tests). Further, comparison between data from the fascicles from the young CDET and the young SDFT samples show the same trend in the thesis as also in the reference data. On the other hand, comparing the old samples the results are inverted. Due to the above mentioned different loading case and tissue hydration it might be at all a problem to compare these results. However, earlier tensile investigations on CDET and SDFT tendons on the macroscale [58]

show the CDET being stiffer than the SDFT which completely agrees with the elastic modulus results of the old fascicles in the transverse cut samples from this thesis.

Chapter 6

Summary, conclusion and outlook

The main goal of the thesis was to investigate individual collagen fibrils and cryosections harvested from equine tendons. These samples originated from the superficial digital flexor tendon and common digital extensor tendon. These types of tendons are known to be functionally different on the macroscale level. The main question was whether also differences on the fascicular and fibrillar, so the microscale and nanoscale level could be observed. The samples originated from 3 year and 18 year old horses. So additionally potential characteristics, which could indicate the phenomena of ageing had to be investigated. As a further step the answer had to be given whether these results could be linked to potential changes in structure and chemistry. The atomic force microscope was an ideal candidate to analyse individual collagen fibrils, according to their swelling behaviour by imaging them in wet and dry condition and simultaneously also getting information about their elastic modulus by performing nanoindentation experiments. For these experiments an already proven experimental protocol was used, which was time consuming but could be performed after a short time of training without any major problems. Micronindentation type AFM experiments posed a bigger challenge. Trying to keep different parameters like the indentation volume and the DZ-slope constant for samples with elastic modulus differing by 2-3 orders of magnitude was a real challenge. Here pretests were done on a position close to the one, which was intended to be investigated on the sample. On this location the force curves were prepared by changing the indentation force, to reach a certain indentation volume, by still having the DZ-slope close to its ideal value of 0.5. Although ideal settings could be found on the pretesting position, it often turned out that the real position of interest, behaved completely different, using the previous settings. This fact indicates a high heterogeneity in mechanical properties on the tendons microscale level. Nevertheless development of the protocol for microindentation type AFM experiments on such tissue was successful. Importantly, at the end

interesting findings could be gained from the longitudinal, as well as from the transversal tendon sections and could mostly also be explained. Thereby one most interesting finding was that investigations on the different fascicle directions (transverse and longitudinal cuts) give the possibility to see the observe and maybe even quantifying the strength of interfibrillar crosslinks. Further, age dependent properties on tendon structures on the micro and on the nanoscale could be observed and explained. Additionally, the most important finding might be, that the main difference on the macro-scale, the CDET being stiffer than the SDFT, could also be observed on the elastic modulus in longitudinal direction from fascicles of old horses. One thing which was missing to completely characterise the mechanical properties of the fascicles were nanotensile properties of individual collagen fibrils. These experiments could not be done due to the fact that such experiments are very time consuming but it would be very important to gain these data in a future project. Further, to strengthen the hypothesis of crosslinks strongly influencing the age dependent material properties, analytical chemistry data would have been necessary. Therefore it would be important for the future to gain this knowledge from appropriate experiments. However the thesis also gave to chance for further future work. According the validation of the diameter determination of the spherical tips using the AFM TGT1- and trench gratings with the SEM as a reference technique, it would be really interesting, to check whether coating in the SEM imaging influences the mechanical properties of the cantilevers, as doing the SEM before the microindentation experiments would for sure improve the amount of data, as the risk of losing the tip due to unforeseeable events would be averted. Furthermore it would be a real advantage if test gratings similar to the TGT1 gratings with spikes of about 1 μm and a larger space in between the spikes were available. Then it would be possible, to produce a real contact area vs. indentation depth function for a large range of contact depth which would be valid for this cantilever, as long as it's not contaminated. The validation experiments on agarose samples showed that AFM type microindentation can properly be used to identify differences on samples with elastic moduli reaching from the kPa to the MPa region. One thing which could be improved in further experiments would be the way of producing the agarose samples. Thereby it might be helpful to use temperature controlled moulds to cool the samples slowly in a predefined way and therefore improving the reproducibility of the preparation procedure. For higher concentrations e.g. 5% it would also be good to keep the Erlenmeyer flask which was used to dissolve the agarose in the specific amount

of water at a temperature where the viscosity is still low as it turned out that the high concentration gels are likely to produce bubbles in the material which makes the samples useless for testing. Keeping them at a specific temperature after dissolving to let air diffusing out of the Agarose-water solution. One interesting investigation which could be done on that in the future is trying to combine the transverse and the longitudinal elastic modulus of fascicles by using theory from fibre reinforced material theories. Assuming fascicles to be such a material with fibrils as fibres, very well aligned in longitudinal direction, would make it possible to use formulas from this theory. Such materials are mechanically characterised by the transverse and longitudinal elastic modulus, which are determined by using the elastic modulus from the fibres (represent the elastic modulus of the individual collagen fibrils) and the fibre volume ratio (ratio of the fibre volume to the total materials volume). Another parameter been used is the elastic modulus of the matrix, which could be assumed to represent the elastic modulus of the proteoglycan-water matrix, crosslinking single fibrils, in our samples. If additionally to the microindentation experiments also morphological investigations on the samples were done, to analyse the fibre volume ratio, it might be possible to calculate the elastic modulus of the matrix thus the quantity of crosslinks.

microindentation Appendix A

Appendix A

Microindentation on gelmod and Polyethyleneglycol

microindentation Main appendix title

microindentation For referencing this appendix elsewhere, use A

The aim of these experiments was to investigate the elastic modulus according to contact depth (h_c) and holding time of different hydrogels for using these knowledge to design the validation experiments on agarose gels. Both parameters were suggested to be important to overcome surface- and viscoelastic effects. Hydrogels are visco- and poroelastic materials which are able to swell and retain high amounts of water in their three dimensional structure without dissolving. If such materials are mechanically loaded, parts of this water re-orientates in the gel or is pushed out. As these processes are not happening spontaneously different loading speeds can lead to different response of the material. As gelmod was not exposed as a whole with UV light, but far more in a way creating stripe-like rectangular structures exposed with gradually different UV-intensities (100 mW, 80 mW, 60 mW, 40 mW). This structure also makes it possible to investigate whether AFM type microindentation is able to identify small differences in mechanical properties.

A.1 Gelmod

Results from gelmod experiments show the necessity of using holding time and also defining an interaction specifying parameter like contact depth h_c or indentation volume, depending on whether one, or different sphere diameters are used in the experiments. Gelmod 1- 3 were UV exposed, so consisting of additional crosslinks compared to Gelmod 4 which was an untreated reference region (see fig. A.1). The elastic moduli from gelmod 1, 2 and 4 show

a holding time dependency, as data from experiments the cantilever was withdrawn right after reaching the predefined indentation force (0s holding time), is shifted to higher values compared to the data, holding time was used. Furthermore the elastic modulus shows a curved behaviour, leading to the suggestion that elastic moduli reaches a plateau for high holding times and large contact depths. Interestingly gelmod 3 does not follow this trend although similar contact depths were reached and the elastic modulus being also in the same range. Experiments from other gel-types for a different project (data not presented here), showed similar curved behaviours and the data also seemed to reach a plateau at higher contact depths and holding times. Similar investigations on photo-crosslinkable hydrogels are shown in [32]. In this work also differently UV penetrated hydrogel stripes were investigated using indentation type AFM. Thereby diving board cantilevers ($k_c=0.5$ N/m- 9.5 N/m) commercially furnished with 3.5 μm spheres were used. In this work visco- and poroelastic characteristics of the gels were investigated, by gradually changing the indentation speed (0.006 $\mu\text{m/s}$ to 200 $\mu\text{m/s}$). The results show that from velocities of about 0.2 $\mu\text{m/s}$ upwards, the elastic modulus is shifted to higher values. In my thesis the piezo extension velocity was constantly set to 0.5 $\mu\text{m/s}$ and just the holding time was changed. Nevertheless investigations on hydrogels characterised by changing the velocity should be comparable to experiments done with specific different holding times as the main idea is to give the material time to adjust. Therefore the curved shape of the elastic modulus vs. contact depth might origin from high extension velocities, which is equivalent to short holding times. The effect might further be enhanced when large micro spheres are used, as a larger area is penetrated, which takes the material more time to adjust. These suggestions should be investigated by doing further indentation type experiments on hydrogels using a even much larger holding times (i.e. 0 s to some minutes).

The mean differences were tested using ANOVA ($\alpha= 0.05$). The equality of variance was tested on the absolute and transformed (square-root, reziproke, logarithmus) data, using the Levene's test implemented in the matlab function `vartestn()`. The ANOVA was done using the data with the biggest P-value from the Levene's (as described above). Data from gelmod 3 was completely excluded in the statistical analysis due to the fact that a bubble located right in the region of interest has certainly influenced the measurements.

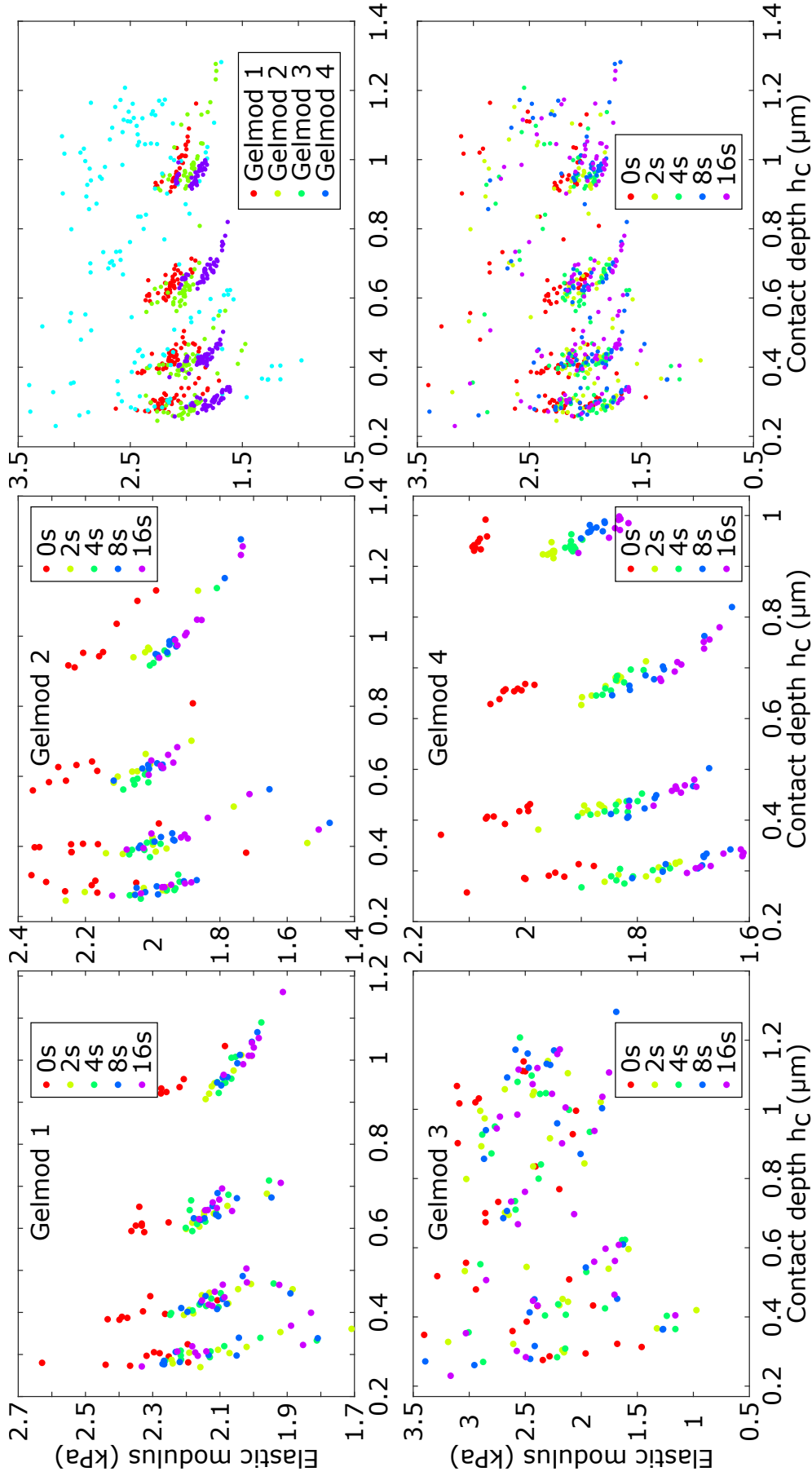


FIGURE A.1: The differently laser-crafted gelmod results strengthen the necessity of using holding time but also defining a specific target value for the contact depth (h_c) or a similar parameter as the indentation volume IV as used in this thesis.

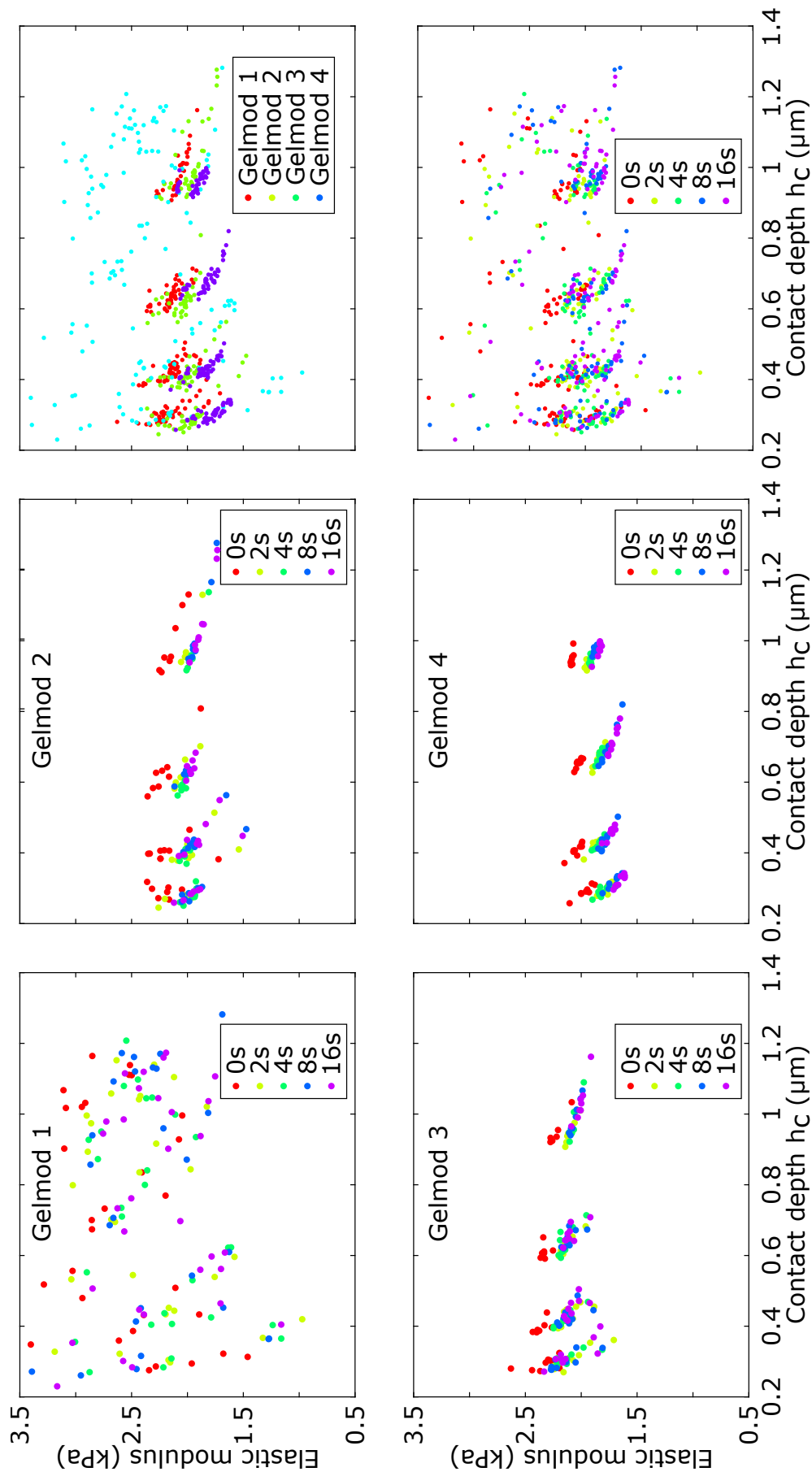


FIGURE A.2: Shows the same figures as presented in A.1 but in scale to make it easier to see differences according to the different gels.

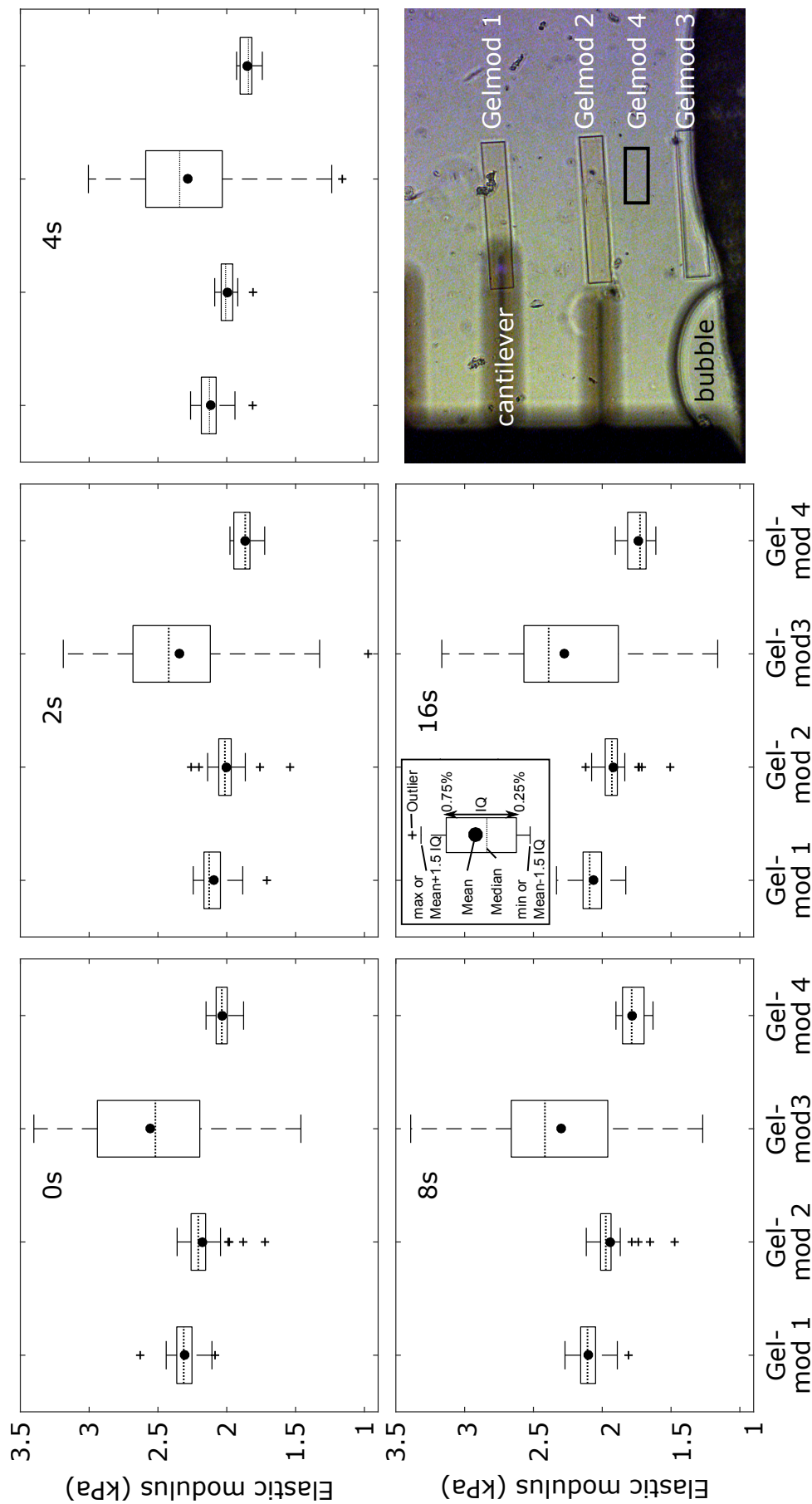


FIGURE A.3: The boxplots shows, differences in elastic moduli for gelmods having been cured with different UV intensity (gelmod 1-3). Gelmod 4 was not exposed and is therefore the reference. The results indicate a dependency on holding time and show additionally to the Agarose gels that AFM type microindentation is able to indicate small differences in mechanical properties.

E-modul (kPa) mean (SD)	Gelmod 1	Gelmod 2	Gelmod 3	Gelmod 4
0 s holding	2.31 (0.1)	2.18 (0.14)	2.55 (0.49)	2.03 (0.06)
2 s holding	2.1 (0.11)	2 (0.13)	2.34 (0.52)	1.86 (0.08)
4 s holding	2.12 (0.1)	2 (0.06)	2.28 (0.48)	1.85 (0.05)
8 s holding	2.1 (0.1)	1.94 (0.13)	2.3 (0.52)	1.78 (0.08)
1 s holding	2.07 (0.11)	1.92 (0.12)	2.27 (0.45)	1.73 (0.08)

TABLE A.1: Shows the results from microindentation experiments on gelmod. Gelmods 1 to 3 were gradually exposed with UV intensity whereas gelmod 1 was penetrated with the highest power. Gelmod 4, the reference, was not exposed with UV. Furthermore the E-modul indicates to be dependent on holding time.

A.2 Polyethyleneglycol (PEG)

The Polyethyleneglycol (PEG) sample was investigated with the same holding-times- and indentation-forces as it was used for the gelmod. The results does not show the dependency in holding time and contact depth h_c as it could be seen in the gelmod samples. However h_c values show that PEG was just one third to one fourth indented. It might be possible, that the elastic modulus also decreases for higher h_c s but a clear dependency on holding time cannot be observed. Even the data, where the cantilever was withdrawn right after contact (0 s) is similarly distributed to the ones holding time was used. This might be explained due to PEG keeping water stronger than gelmod which could be investigated in further experiments.

microindentation	holding time	0s	2 s	4 s	8 s	16 s
E-modul (kPa)mean (SD)		23.49 (4.94)	24.26 (5.25)	25.58 (4.28)	27.02 (4.41)	23.81 (3.76)

TABLE A.2: Shows the results from UV crafted PEG. The same forces and holding times were used as in the gelmod experiments. Against the gelmod the elastic modul of PEG seems to be as much holding time dependent

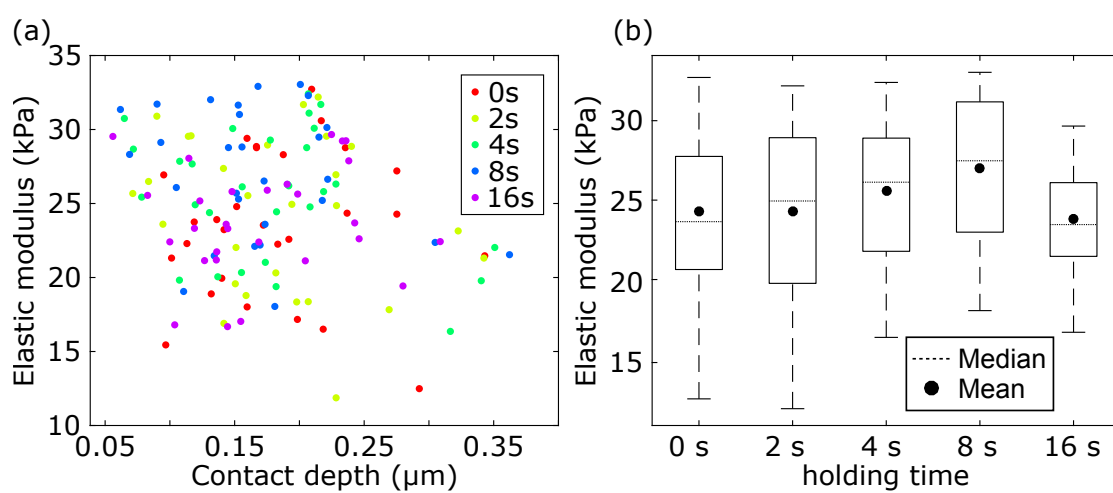


FIGURE A.4: Shows results from microindentation experiments on polyethylene glycol (PEG). The data is evenly distributed and therefore the elastic modulus does not seem to depend on holding time as it was seen in the gelmod results.

Bibliography

- [1] Orestis G Andriotis et al. "Nanomechanical assessment of human and murine collagen fibrils via atomic force microscopy cantilever-based nanoindentation". In: *Journal of the mechanical behavior of biomedical materials* 39 (2014), pp. 9–26.
- [2] Ikai Atsushi. *The world of nano-biomechanics*. 1st ed. Elsevier, 2008. ISBN: 978-0-444-52777-6.
- [3] Andrew A Biewener. "Muscle-tendon stresses and elastic energy storage during locomotion in the horse". In: *Comparative Biochemistry and Physiology Part B: Biochemistry and Molecular Biology* 120.1 (1998), pp. 73–87.
- [4] G. Binnig, C. F. Quate, and Ch. Gerber. "Atomic Force Microscope". In: *Phys. Rev. Lett.* 56 (9 1986), pp. 930–933.
- [5] G. Binnig and H. Rohrer. "Scanning tunneling microscopy". In: *Surface science* 126.1-3 (1983), pp. 236–244.
- [6] Helen L Birch. "Tendon matrix composition and turnover in relation to functional requirements". In: *International journal of experimental pathology* 88.4 (2007), pp. 241–248.
- [7] N Blanc et al. "Scanning force microscopy in the dynamic mode using microfabricated capacitive sensors". In: *Journal of Vacuum Science & Technology B* 14.2 (1996), pp. 901–905.
- [8] The University of Melbourne in Liz Kalaugher Image: Dr. Simon Crawford from School of Botany. *V-shaped AFM cantilevers could have design flaw*. URL: <http://nanotechweb.org/cws/article/tech/17122> (visited on 10/12/2016).
- [9] W.Richard Bowen and Nidal Hilal. *Atomic Force microscopy in process engineering*. Vol. 1. Butterworth-Heinemann, 2009. ISBN: 978-1-85617-517-3.
- [10] SI Bulychev et al. "Determining Young's modulus from the indenter penetration diagram". In: *Zavod. Lab* 41.9 (1975), pp. 1137–1140.
- [11] NA Burnham et al. "Comparison of calibration methods for atomic-force microscopy cantilevers". In: *Nanotechnology* 14.1 (2002), p. 1.

- [12] Hans-Jürgen Butt, Brunero Cappella, and Michael Kappl. "Force measurements with the atomic force microscope: Technique, interpretation and applications". In: *Surface science reports* 59.1 (2005), pp. 1–152.
- [13] Hernandes Faustino De Carvalho. "Understanding the biomechanics of tendon fibrocartilages". In: *Journal of theoretical biology* 172.3 (1995), pp. 293–297.
- [14] Gloria A Di Lullo et al. "Mapping the ligand-binding sites and disease-associated mutations on the most abundant protein in the human, type I collagen". In: *Journal of Biological Chemistry* 277.6 (2002), pp. 4223–4231.
- [15] Georg E Fantner et al. "Components for high speed atomic force microscopy". In: *Ultramicroscopy* 106.8 (2006), pp. 881–887.
- [16] Gion Fessel, Christian Gerber, and Jess G Snedeker. "Potential of collagen cross-linking therapies to mediate tendon mechanical properties". In: *Journal of shoulder and elbow surgery* 21.2 (2012), pp. 209–217.
- [17] Anthony C. Fischer-Cripps. *Nanoindentation*. 3rd ed. Springer-Verlag New York, 2011. ISBN: 978-1-4419-9871-2.
- [18] Patrick Garner. "The contribution of collagen crosslinks to bone strength". In: *BoneKEy reports* 1 (2012), p. 182.
- [19] Colin A Grant et al. "Tuning the elastic modulus of hydrated collagen fibrils". In: *Biophysical journal* 97.11 (2009), pp. 2985–2992.
- [20] Heinrich Hertz. "Ueber die Berührung fester elastischer Körper." ger. In: *Journal für die reine und angewandte Mathematik* 92 (1882), pp. 156–171. URL: <http://eudml.org/doc/148490>.
- [21] Peter Hinterdorfer et al. "Detection and localization of individual antibody-antigen recognition events by atomic force microscopy". In: *Proceedings of the National Academy of Sciences* 93.8 (1996), pp. 3477–3481.
- [22] Matthew A Hopcroft, William D Nix, and Thomas W Kenny. "What is the Young's Modulus of Silicon?" In: *Journal of microelectromechanical systems* 19.2 (2010), pp. 229–238.
- [23] Jeffrey L Hutter and John Bechhoefer. "Calibration of atomic-force microscope tips". In: *Review of Scientific Instruments* 64.7 (1993), pp. 1868–1873.
- [24] P-F Indermühle et al. "Fabrication and characterization of cantilevers with integrated sharp tips and piezoelectric elements for actuation and detection for parallel AFM applications". In: *Sensors and Actuators A: Physical* 60.1 (1997), pp. 186–190.

- [25] Alan Jennings et al. "Empirically based modeling of tape spring hinge deployment for space structures". In: *AIAA SPACE 2011 Conference & Exposition*. 2011, p. 7249.
- [26] Karl E Kadler et al. "Collagen fibril formation". In: *Biochemical Journal* 316.1 (1996), pp. 1–11.
- [27] P Kannus. "Structure of the tendon connective tissue". In: *Scandinavian journal of medicine & science in sports* 10.6 (2000), pp. 312–320.
- [28] Yoshinori Kasashima et al. "Can exercise modulate the maturation of functionally different immature tendons in the horse?" In: *Journal of Applied Physiology* 104.2 (2008), pp. 416–422.
- [29] David J Keller and Fransiska S Franke. "Envelope reconstruction of probe microscope images". In: *Surface Science* 294.3 (1993), pp. 409–419.
- [30] Xiaodong Li and Bharat Bhushan. "A review of nanoindentation continuous stiffness measurement technique and its applications". In: *Materials characterization* 48.1 (2002), pp. 11–36.
- [31] Yang Liu, HS Ramanath, and Dong-An Wang. "Tendon tissue engineering using scaffold enhancing strategies". In: *Trends in biotechnology* 26.4 (2008), pp. 201–209.
- [32] McKenna. "Mechanical Characterization of Photo-crosslinkable Hydrogels with AFM". Thesis. Mount Holyoke College, 2012.
- [33] V.J. Morris, A.R. Kirby, and A.P. Gunning. *Atomic Force Microscopy for Biologists*. 2009. ISBN: 9781908978219. URL: <https://books.google.at/books?id=ale7CgAAQBAJ>.
- [34] nanoworld. *AR5-NCLR*. URL: <http://www.nanoworld.com/pointprobe-high-aspect-ratio-afm-tip-ar5-nclr> (visited on 10/12/2016).
- [35] nanoworld. *NCH*. URL: <http://www.nanoworld.com/pointprobe-tapping-mode-afm-tip-nch> (visited on 10/12/2016).
- [36] nanoworld. *PNP-DB*. URL: <http://www.nanoworld.com/pyrex-nitride-rectangular-silicon-nitride-cantilever-afm-tip-ppn-db> (visited on 10/12/2016).
- [37] nanoworld. *SSS-NCL*. URL: <http://www.nanoworld.com/pointprobe-super-sharp-silicon-tapping-mode-afm-tip-sss-ncl> (visited on 10/12/2016).

- [38] Valéry Normand et al. "New insight into agarose gel mechanical properties". In: *Biomacromolecules* 1.4 (2000), pp. 730–738.
- [39] Warren C Oliver and Georges M Pharr. "Measurement of hardness and elastic modulus by instrumented indentation: Advances in understanding and refinements to methodology". In: *Journal of materials research* 19.01 (2004), pp. 3–20.
- [40] Warren Carl Oliver and George Mathews Pharr. "An improved technique for determining hardness and elastic modulus using load and displacement sensing indentation experiments". In: *Journal of materials research* 7.06 (1992), pp. 1564–1583.
- [41] Janet C Patterson-Kane and Elwyn C Firth. "The pathobiology of exercise-induced superficial digital flexor tendon injury in Thoroughbred racehorses". In: *The Veterinary Journal* 181.2 (2009), pp. 79–89.
- [42] Janet C Patterson-Kane and Tina Rich. "Achilles tendon injuries in elite athletes: lessons in pathophysiology from their equine counterparts". In: *ILAR Journal* 55.1 (2014), pp. 86–99.
- [43] John A Petruska and Alan J Hodge. "A subunit model for the tropocollagen macromolecule". In: *Proceedings of the National Academy of Sciences* 51.5 (1964), pp. 871–876.
- [44] Roberto Raiteri et al. "Micromechanical cantilever-based biosensors". In: *Sensors and Actuators B: Chemical* 79.2 (2001), pp. 115–126.
- [45] John E Sader, James WM Chon, and Paul Mulvaney. "Calibration of rectangular atomic force microscope cantilevers". In: *Review of Scientific Instruments* 70.10 (1999), pp. 3967–3969.
- [46] John Elie Sader. "Susceptibility of atomic force microscope cantilevers to lateral forces". In: *Review of scientific instruments* 74.4 (2003), pp. 2438–2443.
- [47] Kirsten Ingolf Schiffmann. "Area function calibration in nanoindentation using the hardness instead of Young's modulus of fused silica as a reference value". In: *International journal of materials research* 98.5 (2007), pp. 424–429.
- [48] Sara Sibilla et al. "An overview of the beneficial effects of hydrolysed collagen as a nutraceutical on skin properties: Scientific background and clinical studies". In: *The Open Nutraceuticals Journal* 8.1 (2015).

- [49] Ellen R Singer et al. "Injuries in the event horse: training versus competition". In: *The Veterinary Journal* 175.1 (2008), pp. 76–81.
- [50] RKW Smith et al. "The influence of ageing and exercise on tendon growth and degeneration—hypotheses for the initiation and prevention of strain-induced tendinopathies". In: *Comparative Biochemistry and Physiology Part A: Molecular & Integrative Physiology* 133.4 (2002), pp. 1039–1050.
- [51] Roger K.W. Smith and Allen E. Goodship. "Chapter 2.3 - Tendon and ligament physiology: responses to exercise and training". In: *Equine Exercise Physiology*. Ed. by Kenneth W. Hinchcliff, Raymond J. Geor, and Andris J. Kaneps. Edinburgh: W.B. Saunders, 2008, pp. 106–131. ISBN: 978-0-7020-2857-1. DOI: <http://dx.doi.org/10.1016/B978-070202857-1.50007-X>. URL: <http://www.sciencedirect.com/science/article/pii/B978070202857150007X>.
- [52] Paul R Stephens, David M Nunamaker, and Diane M Butterweck. "Application of a Hall-effect transducer for measurement of tendon strains in horses." In: *American journal of veterinary research* 50.7 (1989), pp. 1089–1095.
- [53] Martin Stolz et al. "Dynamic elastic modulus of porcine articular cartilage determined at two different levels of tissue organization by indentation-type atomic force microscopy". In: *Biophysical journal* 86.5 (2004), pp. 3269–3283.
- [54] Juming Tang et al. "Stress-strain relationships for gellan gels in tension, compression and torsion". In: *Journal of Food Engineering* 31.4 (1997), pp. 511–529.
- [55] Chavaunne T Thorpe et al. "Aspartic acid racemization and collagen degradation markers reveal an accumulation of damage in tendon collagen that is enhanced with aging". In: *Journal of Biological Chemistry* 285.21 (2010), pp. 15674–15681.
- [56] Chavaunne T Thorpe et al. "Capacity for sliding between tendon fascicles decreases with ageing in injury prone equine tendons: a possible mechanism for age-related tendinopathy". In: *Eur. Cells Mater* 25 (2013), pp. 48–60.
- [57] Chavaunne T Thorpe et al. "Distribution of proteins within different compartments of tendon varies according to tendon type". In: *Journal of anatomy* 229.3 (2016), pp. 450–458.

- [58] Chavaunne T Thorpe et al. "Specialization of tendon mechanical properties results from interfascicular differences". In: *Journal of The Royal Society Interface* (2012), rsif20120362.
- [59] Chavaunne T Thorpe et al. "The interfascicular matrix enables fascicle sliding and recovery in tendon, and behaves more elastically in energy storing tendons". In: *Journal of the mechanical behavior of biomedical materials* 52 (2015), pp. 85–94.
- [60] Sandeep Kumar Vashist. "A review of microcantilevers for sensing applications". In: *J. of Nanotechnology* 3 (2007), pp. 1–18.
- [61] KG Vogel. "What happens when tendons bend and twist? Proteoglycans". In: *Journal of Musculoskeletal and Neuronal Interactions* 4.2 (2004), p. 202.
- [62] KG Vogel and D Heinegård. "Characterization of proteoglycans from adult bovine tendon." In: *Journal of Biological Chemistry* 260.16 (1985), pp. 9298–9306.
- [63] Takafumi WATANABE et al. "Characteristics of collagen fibrils in the entire equine superficial digital flexor tendon". In: *Okajimas folia anatomica Japonica* 84.3 (2007), pp. 111–114.
- [64] Marco PE Wenger et al. "Mechanical properties of collagen fibrils". In: *Biophysical journal* 93.4 (2007), pp. 1255–1263.